DRUG DELIVERY TO THE POSTERIOR EYE USING ETCHED MICRONEEDLES

DRUG DELIVERY TO THE POSTERIOR EYE USING ETCHED MICRONEEDLES

By

GEETHA MAHADEVAN, B.S.M.E., M.S.

A

Thesis

Submitted to the School of Graduate Studies

In Partial Fulfillment of the Requirements

For the Degree

Doctor of Philosophy

DOCTOR OF PHILOSOPHY (2011) McMaster University
(Chemical Engineering) Hamilton, Ontario

TITLE: Drug Delivery to the Posterior Eye Using Etched Microneedles

AUTHOR: Geetha Mahadevan, B.S. Mechanical Engineering (University of Texas at Austin); M.S. Biochemistry (Worcester Polytechnic Institute, Worcester, Massachusetts, USA)

SUPERVISORS: Heather Sheardown and Kim Jones

NO. OF PAGES: 201

ABSTRACT

Sight-threatening degenerative diseases, such as age-related macular degeneration (AMD), affect the tissues of the posterior segment of the eye. Though modern classes of biomolecular based drugs are therapeutically useful, targeting them for prolonged bioavailability to pathological sites within the eye is challenging. Current clinical approaches such as monthly injections are risky and inefficient while delivery devices lack control over drug release rates and tissue-specific localization. In this thesis, a device using microneedles embedded in a flexible platform was developed that could potentially overcome these challenges.

Methods were developed to (1) construct a prototypical device to integrate hollow and rigid microneedles into a flexible polydimethylsiloxane (PDMS) substrate to demonstrate molecular-weight independent release (2) fabricate hollow glass microneedles and integrate them into flexible elastomeric substrates (3) demonstrate ex-vivo delivery of rhodamine to the various layers in the posterior eye at controllable nanoscale flow rates.

The prototype device demonstrated a new hybrid approach of coupling a hollow and rigid microneedle that was strong enough to penetrate the tough, fibrous sclera with a soft and pliable PDMS substrate that could conform to the irregular shape of underlying biological tissues. Glass microneedles several millimeters tall with 5 μm tips were embedded into a 300 μm microchannel in PDMS. The device released a total of 45 ng of 6-aminoquinolone (144 FU) and 16 μg Rose Bengal (1044 FU) over a 20 minute infusion

at a delivery rate of 50 μL/min, a rate which was alterable by changing such factors as concentration and pressure.

New methods for microneedle fabrication were also developed by co-opting simple chemical etching methods commonly used for optical probe fabrication as an alternative to current complex and expensive photolithographic technologies to produce out-of-plane, high aspect ratio microneedles which are often constrained materially to silicon and metal. Microneedles with repeatable tip and taper sizes were obtained by simply using hydrofluoric acid, an organic phase and fused-silica capillary tubing. Microneedles in the range of 126 μm – 323 μm OD and 10 μm ID were made using single and batch mode methods where up to fifteen 126 μm OD microneedles could be fabricated in 60 minutes. Single 323 μm OD microneedles could be fabricated in 120 minutes. Microneedles were integrated into PDMS for positional placement via a self-guiding alignment scheme using low cost micromolding approaches with the same degree of precision and accuracy provided by conventional photolithography. The same micromolding approach was extended to develop a tool to define microneedle lengths at 50 μm spacings to target the different layers of the posterior eye. The physics of scaling laws proved beneficial as dimensions decreased to the microscale using another approach based on electrokinetic-actuated flows for a one-step "etch and deliver" solution.

Single microneedle-based devices successfully delivered rhodamine intrasclerally, intravitreally, suprachoroidally and to the retina at a set flow rate. This is the first demonstration of active delivery of compounds to a range of specific spatial regions

within the posterior eye at controllable rates using a non-implantable, biocompatible device – with minimal fabrication facilities, equipment and cost.

ACKNOWLEDGEMENTS

This thesis would not have been possible without the support and guidance of my advisor Dr. Heather Sheardown who always kept an encouraging outlook on results that were not always up to my expectation. I am grateful for her superior wisdom in moving me forward through the challenges of undertaking a new idea from scratch.

I would also like to thank my co-supervisors Dr. Ravi Selvaganapathy for his technical guidance in non-traditional microfabrication approaches and Dr. Kim Jones for her valuable advice in the committee meetings.

CEDT staff Doris, Zhilin and Graham, were very helpful while I was learning how to use the Clean Room and Tandem Accelerator facilities. I would also like to thank Mary Jo in Core Histology, Marnie in the Confocal Microscope Facility and Chris with the JEOL SEM in the Brockhouse Institute for their advice and also Dr. Greg Wohl in Mechanical Engineering for use of his ADMET for mechanical testing. The Mech. Eng. Shop Staff and Joe were critical to the design of the experimental setups. My lab mates in JHE A110, Pouya Z, Pouya R, Salman, Bala, Wen and Arash, were invaluable for idea exchange. I thank Lina Liu for her helpful insight into all things polymer-related, Fran for her enthusiastic assistance in procuring eyes and performing the durability study, Lakshman for his helpful ophthalmological advice and the two undergraduate students Cameron and Jessica.

The project was possible due to the generous contribution of eyes from Willie's Custom Meats in Troy, ON and funding from OCE and NSERC.

I finally pay great gratitude to my family, the Johnson family and Dr. Sheardown for their belief in me.

TABLE OF CONTENTS

CHAPTER 1 MOTIVATION AND THESIS OVERVIEW 18

1.1. Motivation 18
1.2. Thesis Objectives 19
1.3. Thesis Organization 20

CHAPTER 2 BACKGROUND AND LITERATURE REVIEW 22

2.1. Introduction to Drug Delivery 22
2.2. Drug Delivery to the Posterior Eye 23
2.2.1. Structure of the Posterior Eye 23
2.2.2. Drug Delivery to the Posterior Segment 24
2.2.3. Engineered Systems for Posterior Eye Drug Delivery 27
2.2.4. Introduction to Microfluidics 31
2.2.5. Microsystems for Drug Delivery 31
2.3. Limitations in Previous Research 33

CHAPTER 3 COMPLIANT PDMS BACKED MICRONEEDLES FOR DRUG DELIVERY 35

3.1. Conceptual Idea 35
3.2. Design Approach 37
3.2.1. Microneedles for Drug Delivery 37
3.2.1.1. Silicon Microneedles 41
3.2.1.2. Metal Microneedles 42
3.2.1.3. Polymer Microneedles 43
3.2.1.4. Glass Microneedles 44
3.2.2. Fabrication of Glass Probes for SNOM 45
3.2.3. Basic Principles of Microscale Flow 52
3.2.3.1. Pressure Driven Flow 52
3.2.3.2. Electroosmotic Flow 53
3.3. Device Design 54
3.3.1. Design Criteria and Material Selection 54
3.3.1.1. Microneedle Material 54
3.3.1.2. Microneedle Dimensions 54
3.3.1.3. Microneedle/Device Configuration 55
3.3.1.4. Device Substrate Material 55
3.3.1.5. Control over Delivery Rates 57
3.3.1.6. Device Dimensions 57

CHAPTER 4 DEVICE FABRICATION AND IN-VITRO DRUG DELIVERY 58

4.1. Fabrication Materials 58
4.1.1. Wafer Prep 58
4.1.2. SU-8 Photoresist 58
4.1.3. PDMS 59
4.2. Fused Silica Tubing 60
4.3. Methods for Fabrication and Assembly 60
4.3.1. UV Photolithography for Mold Fabrication 60
4.3.1.1. Single Mask UV Photolithography 60
4.3.1.2. Master Mold Fabrication Using Dual Layer Photolithography 63
4.3.2. PDMS Casting 65
4.3.3. Microneedle Fabrication 66
4.3.3.1. Pipette Puller 66

4.3.3.2. Microneedle Fabrication using Surface Tension Forces 70
4.3.4. Device Assembly *76*
4.3.4.1. Assembly: Pipette Pulled Microneedles 76
4.3.4.2. Assembly: Microneedles Fabricated using Surface Tensions Forces 78
4.3.4.3. Assembly: Microneedles Fabricated using Surface Tension and Electrokinetic Pumping 82
4.3.5. Optical and SEM Microscopy *85*
4.3.6. Mechanical Testing *85*
4.3.6.1. Pipette Pulled Microneedles 85
4.3.6.2. Surface Tension Fabricated Microneedles 85
4.4. MATERIALS/METHODS FOR DRUG DELIVERY EXPERIMENTAL APPARATUS 88
4.4.1. Model Compounds *88*
4.4.2. Trypan Blue Staining *89*
4.4.3. In-vitro Release from Microneedles *89*
4.4.4. Animal model: Porcine Eye *90*
4.4.5. Ex-vivo Drug Delivery Setup in Porcine Eyes *92*
4.4.6. Histology and Tissue Fixation *95*
4.4.7. Image Analysis *98*
4.5. IN-VITRO DIFFUSION EXPERIMENTS 99
4.5.1. Tracer Molecule *99*
4.5.2. In-vitro Model: Bovine Eye *99*
4.5.3. Diffusion Chamber *100*
4.5.4. Scleral Permeability *101*

CHAPTER 5 IN-VITRO DELIVERY USING EMBEDDED MICRONEEDLES 103

5.1. PROTOTYPE DEVICE AND PIPETTE PULLED MICRONEEDLE MEASUREMENT 103
5.2. PENETRATION OF COLLAGEN/BOVINE SCLERA AND RELEASE IN PBS 106

CHAPTER 6 FABRICATION OF SINGLE MICRONEEDLES USING SURFACE TENSION 110

CHAPTER 7 SITE-SPECIFIC EX-VIVO DELIVERY VIA SINGLE EMBEDDED MICRONEEDLE 117

7.1. EMBEDDING SINGLE MICRONEEDLES IN MICROPATTERNED PDMS SUBSTRATES 117
7.2. MICRONEEDLE PENETRATION OF BOVINE SCLERA 119
7.3. INCREASE OF TRANSSCLERAL PERMEABILITY USING MICRONEEDLE INDUCED DEFECTS 122
7.4. TRYPAN DELIVERY USING A SINGLE EMBEDDED MICRONEEDLE 127
7.5. INTRAVITREAL DELIVERY OF RHODAMINE 131
7.6. TRANSSCLERAL, SUPRACHOROIDAL AND RETINAL DELIVERY OF RHODAMINE 140
7.7. INTRASCLERAL DELIVERY OF RHODAMINE 144
7.8. INTRASCLERAL DELIVERY OF BSA 155

CHAPTER 8 INTERFACIAL BOND STRENGTH CHARACTERIZATION 157

CHAPTER 9 DURABILITY STUDY 160

CHAPTER 10 MICRONEEDLE ARRAYS: FABRICATION, INTEGRATION AND APPLICATION 164

10.1. ETCHING OF MICRONEEDLE ARRAYS 164
10.2. INTEGRATION OF ARRAY-ETCHED MICRONEEDLES 166
10.3. VARIATION USING ELECTROOSMOTIC PUMPING 170

CHAPTER 11 CONCLUSIONS/FUTURE WORK 176

CHAPTER 12 REFERENCES 187

CHAPTER 13 APPENDIX 195

13.1. POLYMICRO FUSED SILICA PRODUCT GUIDE.....195
13.2. PX273- PRESSURE TRANSDUCER 197
13.3. STANDARD CURVES FOR QUANTIFICATION OF MODEL COMPOUNDS 199

LIST OF FIGURES

Figure 1. Tissue layers of the posterior eye (Adapted from [19]) 24
Figure 2. Drug penetration avenues for targeted delivery to the posterior eye segment [Image reproduced from [18]. 26
Figure 3. Image shows a conceptualized prototype of a microneedle based drug delivery device. Rigid, hollow, glass microneedles with sub-micron sized tips are arranged in a precisely spaced two-dimensional array and embedded in a flexible elastomeric platform that can conform to underlying tissues in biological applications. 36
Figure 4. 20 x 20 array of silicon microneedles fabricated using photolithographic and reactive ion etching (RIE) methods Image reproduced from [61]. 39
Figure 5. Fabrication of tapered tips using air-etchant surface tension effects to make hollow electrospray nanoemitters. Water is pumped through the inner bore, indicated by the arrows, to prevent HF influx and enlargement of the native inner bore [99]. 46
Figure 6. Process flow for single layer mask design Single mask UV photolithography showing a pristine 3" silicon wafer activated using oxygen plasma (I) for enhanced adhesion of epoxy-based SU8 photoresist spun coated (II) onto the oxidized wafer forming of a 100 μm layer of SU8 followed by (III) UV photolithography through a defined photomask allowing selective passage of ultraviolet light to micropattern the underlying resist. The target relief structures remain behind after solvation of unexposed photoresist in developing solution (IV). The mold is ready to be used to cast microstructures in PDMS. ...63
Figure 7. Process flow for dual layer mask design: a single mask UV photolithography round was first performed on a 3" silicon wafer activated using oxygen plasma (I) for enhanced adhesion of epoxy-based SU8 photoresist spun coated (II) onto the oxidized wafer forming of a 100 μm layer of SU8 followed by (III) UV photolithography through a defined photomask allowing selective passage of ultraviolet light to micropattern the underlying resist. The target relief structures remained behind after solvation of unexposed photoresist in developing solution (IV). A second layer of SU-8 was then spun onto the first patterned layer using the same processing conditions used for the first round of photolithography (V) followed by a timed UV exposure (VI) and then subsequently developed to reveal the second layer aligned on top of the first layer (VII). The mold was then used to cast multiple PDMS molds with microchannels possessing microneedle positioning markers for accurate microfluidic coupling. 65
Figure 8. P-97 instrument settings for generating micropipettes with sub-micron tip diameters (The P-97 Pipette Cookbook: 2006, revision C, Sutter Instruments, Novato, CA) 68
Figure 9. Schematic showing micropipette fabrication: a single borosilicate capillary tube is pulled biaxially while heating the midpoint to 585°C to form two micropipettes with taper lengths of 9 mm and tip diameters in the range of several microns. 69
Figure 10. SEM image of tip of pulled micropipettes. (The smaller tube visible in the image is supplied by manufacturer to facilitate ease of aspiration for suction applications.) 69
Figure 11. Experimental setup for etching capillary tubing in 49% HF 71
Figure 12. Pressurized flow of water through a 126 μm OD/10 μm ID capillary tubing array before immersion into HF etchant for the etch process to fabricate microneedle arrays 75
Figure 13. Post-etch image showing arrays of 15 X 126 μm OD/ 10 μm ID microneedles using the native polyimide coating for the unmodified ends to prevent breakage and fracture of the tubing during assembly, handling, etching and microneedle retrieval 76
Figure 14. Process flow diagram for assembly of PDMS substrate to embed pipette pulled microneedles for the delivery device 78
Figure 15. Image of a single 323 μm OD/ 10 μm ID microneedle in an alignment groove in PDMS 80
Figure 16. Mask used for setting microneedle length based on tissue target for solute delivery. 81
Figure 17. Capillary tubings were preloaded with methylene blue dye for visualization of filling, tested for conductivity and then embedded into the microchannels (A) for subsequent taper definition using HF etchant. A single droplet of water was then placed on the top-side of the tubing array (B) to provide a reservoir from which to pump water through the capillary once the assembly was placed in an electric field. 82

Figure 18. Experimental apparatus for parallel fabrication of microneedle arrays using a micromolded PDMS capillary tubing alignment positioner, a single droplet water reservoir and an electric field* 84
Figure 19. Tensile samples showing 10 cm long capillary tubing samples being pulled in tension from the PDMS substrates to which they are bonded to in order to determine the failure force of the interfacial bond 87
Figure 20. Schematic of specimen holder to measure bond failure force under shear loading 88
Figure 21. Sections from porcine eyes used to characterize average scleral thickness 92
Figure 22. Microneedle device positioning into whole porcine globes followed by clamping of tubing for support for ex-vivo release studies 94
Figure 23. Porcine whole globe frozen in liquid N_2 and sectioned using a band saw. Spatial arrangement of the posterior section is intact and ready for chemical fixation. (The lens and vitreous are visible due to their high water content). 97
Figure 24. Tissue layers of the posterior porcine eye - as visualized from histological analysis of frozen, sectioned and H&E stained samples 98
Figure 25. Two-chamber permeability experiment to determine diffusion of 40 kDa FITC-Dextran through a section of bovine scleral membrane. 101
Figure 26. Stereoscopic images showing delivery of dye in pulled microneedles integrated into the assembled micropatterned PDMS device. Microchannels were 300 μm wide and 5.0 cm long flanked by terminating 1.0 x 2.0 cm^2 rectangular reservoirs on either end. Aerial view (A) of the device showing pulled microneedle tips aligned with the underlying 300 μm microchannel; side angle view (B) filled microneedles without any leakage; solution emerging (C) from the 2-um tips. 103
Figure 27. Characteristic taper and tip appearance on micropipettes pulled from capillaries. Although pulled micropipette tips appeared extremely sharp, images analyzed under increased magnification showed that the actual tip did not terminate into a defined sharpened tip. 104
Figure 28. Mean tip ID, tip OD, cone angle and taper length for pulled micropipette tips. Tips were pulled from 1.00 mm OD/0.50 mm ID standard wall borosilicate capillaries using the P-97 Puller at #33 program conditions. 105
Figure 29. Microneedle penetration of UV-crosslinked collagen (A) and excised bovine sclera (B). Insertion and penetration was achieved without microneedle fracture. 106
Figure 30. Continuous delivery of Rose Bengal solution at a rate of 50 μL/min. Red arrows indicate the fixed location of the microneedles in the reservoir from which visible streaklines appear. 107
Figure 31. Delivery of model compounds through the assembled device using active pumping at a rate of 50 μL/min of Rose Bengal solution (12.5 μg/mL (N=2)) and 6-aminoquinolone (0.05 μg/mL (N=3)) 108
Figure 32. Delivery in ex-vivo bovine eye: intravitreal delivery (A) of dye and (B) dye penetration in the posterior segment after release from the microneedle array 109
Figure 33. A 323 μm OD/10 μm ID hollow glass microneedle fabricated using surface-tension mediated tip sharpening (A) at 40X magnification. Similar shapes and tip diameters were obtained for 126 μm OD/10 μm ID microneedles (B). A near-field image of a 126 μm OD/10 μm ID microneedle at 200 X magnification (C) shows the uniform and symmetrical structure obtained. 110
Figure 34. Images show 323 μm OD/10 μm ID tipped microneedles obtained independently illustrating a repeatable resultant shape, taper length and cone angle using the etch processes. 111
Figure 35. Mean tip ID, tip base OD, taper length and cone angle for microneedles fabricated from 323 μm OD/10 μm ID capillary tubing using surface tension mediated chemical etching. 112
Figure 36. Images show 126 μm OD/10 μm ID tipped microneedles obtained independently illustrating a repeatable resultant shape, taper length and cone angle using the etch processes. Slight visible taper asymmetry was attributed to slight misalignment from a true vertical position of the tubing with the chemical etchant during the chemical process. 112
Figure 37. Mean tip ID, tip base OD, taper length and cone angle for microneedles fabricated from 126 μm OD/10 μm ID capillary tubing using surface tension mediated chemical etching. 113
Figure 38. Evolution of taper on an optical fiber via meniscus based chemical etching. Figure adapted from [130]. 114

Figure 39. Process flow showing embedding of microneedles into PDMS: the master SU-8 microfabricated mold containing the positive relief microstructured pattern (I) is used to cast microchannels in PDMS (II) possessing the negative impression of the master mold features (III). The microneedles are then subsequently embedded into the microchannels (IV) for precise alignment and interneedle spacing.....117
Figure 40. Before final bonding of the tubing (A) and after fixation (B) of a 323 μm OD/20 μm ID microneedle with a corresponding 20 μm tip 118
Figure 41. The front edge of the straight-cut PDMS is placed flush against the PDMS stop patterned in SU8. The microneedle is then manually positioned to the desired length using a microscope. Microneedles are shown at different lengths of (A) 300 μm (B) 800 μm and (C) 1.1 mm. 119
Figure 42. Microneedle insertion point in bovine sclera after penetration using a single embedded 126 μm OD microneedle on the episcleral side using trypan blue staining of porcine sclera after treatment with a single 126 μm OD microneedle with a 10 μm tip. 120
Figure 43. Insertion of a single 450 μm tall 126 μm OD/10 μm ID microneedle into excised bovine sclera; penetration was sufficient to raise the sample due to frictional adhesion between the microneedle tip and tissue. The tissue remained adherent to the tissue and did not fall under its own weight.....121
Figure 44. A single microneedle inserted into a whole bovine globe was able to insert and remain adherent with the scleral matrix. The adhesion (i.e. frictional forces) between the microneedle and the tissue was adequate to balance the weight of both the PDMS substrate and the embedded microneedle. 122
Figure 45. Strong adhesion forces between a single microneedle embedded in a PDMS substrate prevent decoupling of the device under gravity forces (A) and visible insertion point (B) remaining in the sclera after manual removal of the device. 122
Figure 46. Average Cumulative Mass vs Time for 40 kDa-Dextran Transfer across Intact Bovine Sclera at 25°C (N=3).....124
Figure 47. Cumulative Mass vs Time for 40 kDa FITC-Dextran in Bovine Sclera penetrated 5 times with a 1 mm long 323 μm OD/10 μm ID microneedle 125
Figure 48. Perforations in bovine sclera after penetration using a 1 mm tall 323 μm OD/10 μm ID microneedle. Defect sizes are approximately 150 μm dia estimated using a section of 150 μm capillary tubing.....126
Figure 49. Insertion and retention of a 1-mm tall 323 μm OD/10 μm ID microneedle into porcine whole globes 127
Figure 50. Average scleral thickness with respect to distance from the corneoscleral limbus for the four quadrants defined 128
Figure 51. A 126 μm OD/10 μm ID microneedle set to a height of 750 μm using the dimensions defined in the SU-8 master wafer.....129
Figure 52. A 126 μm microneedle showing a droplet of trypan blue from a 126 μm OD/10 μm ID; the insertion point (white arrow) is visible after the device was removed 130
Figure 53. Arrows indicating sections of intrascleral trypan blue delivery using a 750 μm tall 126 μm OD/10 μm ID microneedle.....130
Figure 54. Droplet of rhodamine emerging from the tip of a 1.1 mm tall 323 μm OD/10 μm ID microneedle 131
Figure 55. Light microscope image of section showing evidence of microneedle insertion (white arrows) at a distance away from the central point that actually penetrated the sclera. 50 μm sections were cut across the plane containing the insertion point to reveal the cross section. Sclera from this particular sample was measured to be ~300 μm thick. The fluorescence image shows enhanced fluorescence signal indicating (circle) rhodamine infusion near the microneedle insertion site.....133
Figure 56. Light microscopy image of a section cut several sections away from the previous section in the direction towards the microneedle insertion site showing increased depth of penetration (indicated by arrow) 133
Figure 57. Rhodamine B was injected at a flow rate of 200 nL/min for 65 minutes. Post-dissection inspection revealed accumulation of the delivered 13.2 uL (A). Control vitreous body (B) is shown for comparison. 134
Figure 58. Intrascleral release of rhodamine associated with penetration of microneedle 135

Figure 59. Depot of Rhodamine B delivered intravitreally over 25 minutes.....137
Figure 60. Episcleral side insertion point (A) and uveal side defect (B). There was no evidence of transscleral, suprachoroidal or retinal delivery – only the singular intravitreal depot.....137
Figure 61. Intrascleral/transscleral release of rhodamine after infusion; note microneedle insertion point 138
Figure 62. Microneedle insertion point showing attenuation of fluorescence signal proximal to the region adjacent to the microneedle-induced defect. 138
Figure 63. Visible insertion point (shown by arrow) on globe after mock delivery experiment 139
Figure 64. Microneedle insertion point (shown by arrow) is visible on the uveal side indicating microneedle penetration through the sclera. However, there was no observable evidence of any dye released to the vitreous humour through passive diffusion alone.....140
Figure 65. The device, this time embedded with a 1 mm long 323 μm OD microneedle with a 10 μm tip was inserted into an identical position on the porcine globe. Rhodamine B was injected at a flow rate of 500 nL/min. A small portion of the total 26.5 μL delivered volume had localized to the suprachoroidal space just anterior to the choroid (A) while further revealed staining of the scleral floor with a microneedle impression (B). Most of the volume delivered had flowed to the retina as shown in (C). 141
Figure 66. Post-delivery images of porcine sclera taken using confocal microscopy showed transscleral penetration of the 1 mm microneedle delivering Rhodamine B at the insertion point (a) 100 μm from the insertion point (b) 200 μm from the insertion point (c) 250 μm from the insertion point (d) 300 μm from the insertion point (e) 450 μm from the insertion point and (f) 500 μm from the insertion point.....143
Figure 67. Accumulation of a portion of the 26.5 uL rhodamine dispensed was visually observed in detached retina and further confirmed using fluorescence microscopy (A). No autofluorescence of equivalent intensity could be detected in control retina samples (B). 144
Figure 68. A 323 μm OD/10 μm ID microneedle embedded to approximately 400 μm.....145
Figure 69. Post-delivery inspection of ocular tissues showed that rhodamine was only delivered to the scleral floor for the infusion case employing a 400 μm microneedle. The thickness of the sclera at the insertion point was also measured to be about 400 μm. 145
Figure 70. Corrected Total Region Fluorescence (CTRF) levels in porcine sclera with increasing distance from the scleral floor. (0 microns represents the uveal side of the sclera; 750 microns is the episcleral end). 147
Figure 71. Porcine sclera infused with 12.7 μL rhodamine using a 400 μm long 323 μm OD/10 μm ID microneedle. Images are shown in order starting from the scleral floor at 0 microns. 151
Figure 72. Cross sectional section through insertion point showing a 250 μm diameter orifice through the sclera with BSA visible at the circumference of the orifice. 156
Figure 73. Images taken from the same scleral section showing delivery of FITC-BSA.....156
Figure 74. Average failure stress under tensile loading for the interfacial bond between 363 μm OD polyimide coated tubing and 10:1 PDMS for four different bonding adhesives: PDMS at ratios of 10:1, 3:1 and 30:1 base:curing agent and 10:1 PDMS with 0.085 wt% fumed silica.....158
Figure 75. Microneedle A: before and after images after 10 attempts of insertion and removal into a whole porcine globe.....162
Figure 76. Microneedle B: before and after images after 6 attempts of insertion and removal into a whole porcine globe.....162
Figure 77. Microneedle C: before and after images after 6 attempts of insertion and removal into a whole porcine globe.....162
Figure 78. Microneedle D: before and after images after 6 attempts of insertion and removal into a whole porcine globe.....163
Figure 79. Resultant 126 μm OD/10 μm ID microneedles fabricated using the described process 164
Figure 80. Mean tip ID, tip Base OD, taper length and cone angle for microneedles fabricated from 126 μm OD/10 μm ID capillary tubing using array based fabrication. 165
Figure 81. Construction of one-dimensional linear arrays of two 323 μm OD microneedles (A) three 323 μm microneedles (B) and five 126 μm OD microneedles (C) using the methods described. 166
Figure 82. Series of images showing how microneedles are aligned using a flat stainless steel panel and a microscope. Once tubing sections containing the sharpened tips are rolled into their grooves (I) the lengths

are adjusted for equivalency by pushing the needles back to set the target length (II). In these images, 5 X 126 μm OD microneedles are shown at a length of approximately 450 μm. 167
Figure 83. Five-microneedle linear array after embedding shown next to mm-scale markers.....167
Figure 84. SEM images of a 5 X 126 μm OD/ 10 μm ID microneedle array.....168
Figure 85. Size comparison of 2 X 126 μm OD/10 μm ID microneedles embedded into micropatterned PDMS substrates. Microneedles are shown next to a 30 Gauge stainless steel needle (305 μm OD X 140 μm ID) currently used for intravitreal injections.....169
Figure 86. Insertion and retention of an array of 5 X 126 μm OD 500 μm tall microneedles.....170
Figure 87. Schematic of the principle behind microneedle fabrication using pressure driven (A) and single droplet electroosmotic actuated flow (B) of water efflux through the inner bore of the capillary tubing to prevent internal etchant rise 171
Figure 88. Post-etch optical image (A) showing the resultant array of etched microneedles within the PDMS substrate. Capillary tubings are not fixed during the etching process and can hence be easily positioned (B) for precise planar alignment after etching. 172
Figure 89. Post-alignment optical image (A) of microneedles at an interneedle pitch of 150 μm. Top view (B) of linear array showing precision spacing of the microneedles embedded in the PDMS matrix – device is ready to be used within a drug delivery setup.....173
Figure 90. Mean tip ID, tip base OD, taper length and cone angle for microneedles fabricated from 126 μm OD/10 μm ID capillary tubing using an electrokinetic method of array based fabrication. 174
Figure 91. Pressure transducer DC output and fitted with a 24 VDC power supply 198
Figure 92. Pressure sensor calibration curve for the PX273 – 300 DI. 198

LIST OF TABLES

Table 1. Major classes of Si microneedles categorized by configuration.....42
Table 2. Major classes of metallic microneedles categorized by configuration 43
Table 3. Examples of polymeric microneedles categorized by configuration 44
Table 4. Glass microneedle fabrication using the drawn glass method 44
Table 5. Density and surface tension of various organic overlaying reagents [Table adapted from Ref. [112]] 51
Table 6. Recommended spin speed for Microchem SU8-100 Negative Photoresist 59
Table 7. Exposure, post-bake and development time for Microchem SU8-100 Negative Photoresist.....61
Table 8. Failure Shear Stress for Tubing/PDMS Interface.....159
Table 9. Outcomes of single embedded 323 μm microneedle durability tests in whole porcine globes 161

LIST OF ABBREVIATIONS

AMD	Age-Related Macular Degeneration
FU	Formula Unit
OD	Outer Diameter
PDMS	Polydimethylsiloxane
ID	Inner Diameter
SEM	Scanning Electron Microscope
H&E	Hematoxylin and Eosin
VDC	Volts Direct Current
CMV	Cytomegalovirus
GAG	Glycosaminoglycans
VEGF	Vascular Endothelial Growth Factor
PGA	Polyglycolic Acid
PLA	Polylactic Acid
PLGA	Polylactic-co-glycolic acid
PKC412	Protein Kinase C 412
MEMS	Microelectromechanical Systems
IC	Integrated Circuits
RIE	Reactive Ion Etching
PVP	Polyvinylpyrrolidone
DRIE	Dry Reactive Ion Etching
LPCVD	Low Pressure Chemical Vapor Deposition
UV	Ultraviolet
UV-LIGA	Ultraviolet Lithographie, Galvanoformung, Abformung
SNOM	Scanning Near Field Optical Microscopy
ESI-MS	Electrospray Ionization Mass Spectroscopy
FITC	Fluorescein Isothiocyanate
BSA	Bovine Serum Albumin
OCT	Optimal Cutting Temperature
ROI	Region of Interest
PBS	Phosphate Buffered Saline
CTRF	Corrected Total Region Fluorescence
RPE	Retinal Pigment Epithelium
CNV	Choroidal Neovascularization
VISION	VEGF Inhibition Study in Ocular Neovascularization

Chapter 1 Motivation and Thesis Overview

1.1.Motivation

The most prevalent sight-threatening diseases affecting the posterior eye include age-related macular degeneration (AMD), macular oedema secondary to retinal vein occlusion, uveitis, diabetic retinopathy, cytomegalovirus (CMV) retinitis and retinitis pigmentosa [1].

Development of AMD and diabetic retinopathy in particular increases with age as reported by an epidemiological study following populations that experienced visual impairment caused by these diseases in the United States, Europe and Australia [2]. AMD has also been identified as the leading cause of irreversible blindness among elderly patients in the Western world, affecting an estimated 1.75 million people in the U.S. with a projected 50% increase by the year 2020 due to extended life spans as well as a steady increase in the number of people over the age of 75 within the general population [3]. Diabetic retinopathy remains the leading cause of blindness in non-elderly groups of working age individuals and affects 10% of all diabetics [4].

While effective pharmacological therapies exist commercially, an effective delivery method for these drugs to preferentially target the posterior eye segment remains elusive. Currently, intravitreal injections of the new classes of anti-angiogenic drugs are the most prevalent clinical intervention for AMD treatment. However, chronic disease states require frequent injection, which can be painful and difficult for elderly patients. Directing drugs to the posterior tissues such as the

choroid and retina is challenging and risky as intravitreal injections raise the likelihood of associated post-surgical adverse events such as retinal detachment, vitreous hemorrhage, and cataract [5]. Moreover, frequent administrations of large boluses may be needed in order to reach therapeutically relevant dosing for long-term treatment depending on a particular drug's rate of clearance from the vitreous [5]. Further limitations include lack of control over dosing and the lack of ocular tissue specificity and control.

As such, the development of less invasive, less painful and more convenient methods for posterior eye drug targeting is an active area of research.

1.2.Thesis Objectives

The main objective of this thesis was to design and develop a microfluidic device to deliver model drugs to the posterior eye using a controlled and targeted method. Specific objectives included:

a. Miniaturization of device dimensions that interact with ocular tissues in order to mitigate risks, tissue trauma and pain associated with current clinically invasive methods
b. Active control over drug infusion rates for on-demand dosing- a desirable improvement over drug-loaded polymer-based methods where drug release rate is governed by the physicochemical properties of the drug, the matrix material and the surrounding tissues.

c. Tissue-specific targeting of the posterior eye layers as current intraocular delivery approaches cannot be spatially controlled to deliver to a range of tissue targets
d. Design and development a device with optimum characteristics to overcome these limitations followed by fabrication and testing using in-vitro and ex-vivo ocular tissue models

1.3.Thesis Organization

The thesis is organized into the following chapters:

Chapter 2 discusses the general anatomy of the posterior segment of the eye, the various drug delivery routes to reach these tissues and the different classes of drug delivery systems that have been developed for posterior ocular applications along with their limitations.

Chapter 3 lists the specific objectives of the thesis and the advantages that a microneedle based device provides for an improved method of ocular drug delivery. Associated engineering concepts related to the design are considered and used to establish the criteria for device design and material selection. Tasks based on the thesis objectives are defined.

Chapter 4 details the materials selected for the device and the processes developed for microneedle fabrication and substrate integration. Methods and materials developed for the in-vitro and ex-vivo drug delivery experiments and device characterization are summarized.

Chapter 5 discusses in-vitro experimental results obtained for an early device fabricated to demonstrate that microneedles embedded in flexible PDMS substrates were capable of controlled release of model solutes.

Chapter 6 summarizes processes developed in this thesis for generating individual microneedles using a novel, simple and inexpensive method of fabrication.

Chapter 7 shows results obtained for delivery of rhodamine and bovine serum albumin to various layers of model porcine eyes using a single microneedle based device. Mechanical characterization of the device along with results from tissue permeability experiments are also presented and discussed.

Chapter 8 and Chapter 9 cover the mechanical characterization of the developed microneedle device.

Chapter 10 shows the results for processes developed to extend the single microneedle fabrication method to generate high throughput microneedle arrays. A variation on array fabrication using electroosmotic principles for microneedle array fabrication was also developed which could potentially further simplify the microneedle fabrication processes developed in this thesis.

Chapter 11 presents the closing discussion with recommendations for future work. Chapter 12 lists the references. The appendix containing supplemental data is in Chapter 13.

Chapter 2 Background and Literature Review

2.1.Introduction to Drug Delivery

Engineered drug delivery systems target specific regions or tissues in the body in order to minimize side effects, reduce dosing requirements and provide a method of localized delivery to tissues that are conventionally difficult to access – e.g. the eye, brain or arterial tissues [6]. Within the past few decades, research efforts towards drug delivery systems have been driven by parallel growth in other areas of the pharmaceutical field as a wide range of pharmaceuticals are now increasingly complex and based on genes, proteins and nucleic acids in addition to increasing awareness that drug release profiles affect therapeutic responses in vivo [7]. In-vivo drug concentrations must typically stay within narrowly defined range of levels in order to effect reasonable bioavailability between a minimum threshold concentration for therapeutic efficacy and a maximum critical concentration above which damage to functional organs/tissue or non-specific cell surface receptor binding could occur [8]. Chemical stability of drugs is also crucial in the design of drug delivery systems as many modern protein and nucleic acid based drugs can be susceptible to enzymatic degradation [8]. For these reasons, advancements are continuously being developed to formulate new drug release systems with high specificity that enhance the bioavailability of functional drugs at the target site with the appropriate rate of release [8]. This approach to controlled release allows drug dosing at constant levels over prolonged periods of time. As such, drug levels remain within a therapeutically relevant range for long durations [9].

Drug delivery to the eye is particularly difficult due to low tissue permeability to most drugs and multiple convection routes for transport of drugs away from target ocular tissues [10]. The posterior segment of the eye in particular is extremely protected from the external environment due to both anatomic and physiologic barriers which pose a significant challenge for deployment of therapeutic drugs to intraocular tissues affected by disease [11].

2.2. Drug Delivery to the Posterior Eye

2.2.1. Structure of the Posterior Eye

The eye is a 98-99% water-filled flattened spherical shell approximately 23-24 mm in diameter [12]. The anterior portion of the eye consists of the cornea, a highly ordered and crystalline arrangement of collagen fibrils (30 nm - 300 nm OD) comprising 7% of the total surface area of the eye and the sclera which is comprised of an amorphous arrangement of collagen that varies in total thickness between 0.1 and 1.0 mm around the globe [12]. The sclera is the tough, white fibrous outer layer of the posterior eye and is permeable to nucleic acids and other higher molecular weight biomolecules < 70kDa [13-15]. The sclera has a large and accessible surface area, a high degree of hydration and is mostly acellular. The sclera is 75% collagen by dry weight, non-collagenous proteins 10% and 1% glycosaminoglycans (GAGs) and isolated fibroblasts [16].

Covering the sclera is the conjunctiva - a transparent cell layer proximal to the cornea while the Tenon's capsule contains the sclera and is mostly acellular and fibrous; the sclera itself is comprised of three layers: the episclera, the

stroma and the lamina fusca [16]. The outermost episclera is made up of loosely arranged bundles of collagen interspersed with random fibroblast cells, proteoglycans and a few melanocytes leading into the inner layer of the episclera consisting of thicker bundles of collagen that begin forming ordered lamellae [17]. The stromal layer has more elasticity than the episclera with the occasional fibroblast and even larger bundles of collagen. The lamina fusca contains loosely coherent collagen bundles mixed with melanocytes and mesodermal cells leading into the choroid [17]. Figure 1 shows a simplified schematic of the posterior layers of the eye.

The average human scleral thickness varies from 0.39 – 1.0 mm from the limbus to the optic nerve[17],[18].

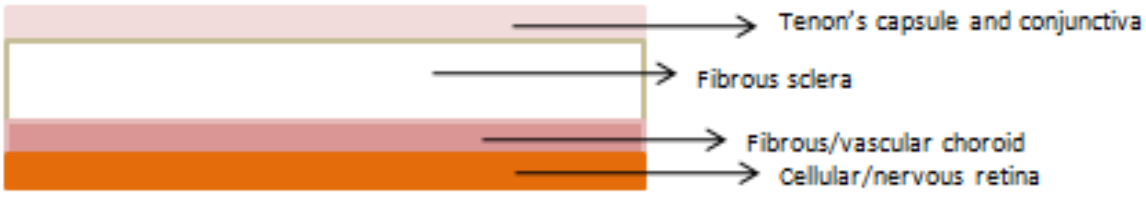

Figure 1. Tissue layers of the posterior eye (Adapted from [19])

2.2.2. Drug Delivery to the Posterior Segment

Drugs can be directed to the intraocular tissues using four main drug penetration routes: systemically, topically, transsclerally and intravitreally by penetration through the outer sclera. Figure 2 illustrates these four delivery modalities [18].

Systemic administration of drugs is the traditional route in delivery therapeutic compounds to the posterior region. However, in order to achieve a suitable dose to the posterior segment, systemic administration of drugs often needs to be delivered at artificially high doses. The high dosage accounts for losses as a result of normal drug metabolic activities by the liver to allow for a sufficient dose to cross the blood-ocular and blood-retinal barriers for ultimate penetration to the intraocular issues [19]. This can result in systemic overdosing with associated physiological toxicity effects.

The second and most commonly used traditional method of ocular dosing is topical instillation of eye drops as shown via path (a) in Figure 2. Similar to systemic dosing, topical administration involves the use of unnecessarily high concentrations of drug in order to reach a fraction of therapeutically relevant drug concentration at the target pathological site. Topical corneal application of drugs have significant drawbacks as typically less than 5% of the drug actually reaches the intraocular space due to the combined effects of the corneal epithelium acting as an excellent diffusion barrier to solute permeability immediately following instillation, high tear fluid turnover, systemic and local drainage pathways and a long diffusional pathway to the neural retina while significant losses due to precorneal drug loss via tear drainage, tear fluid turnover, counterdirectional intraocular convection and corneal impermeability also dominate [7, 17, 18]. Considerable systemic drainage also occurs through

the nasolacrimal duct and through absorption by the nasal and nasopharyngeal mucosa [18].

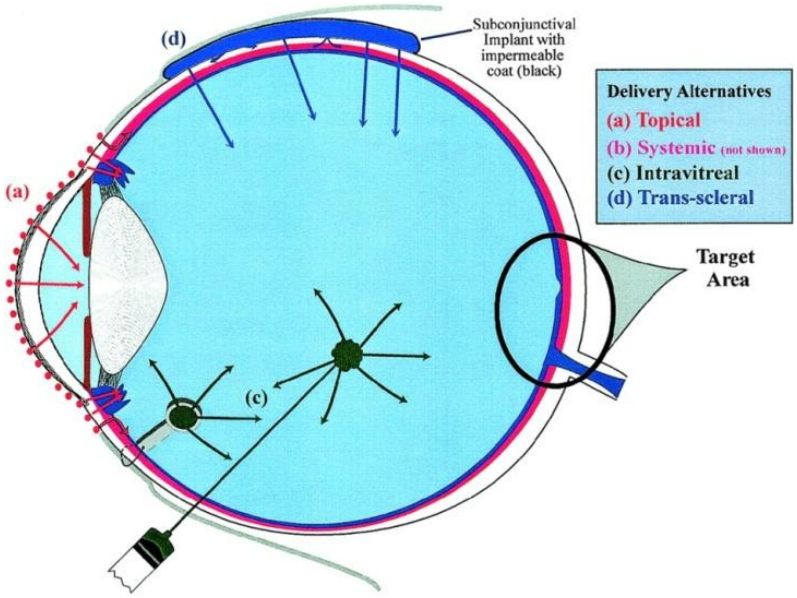

Figure 2. Drug penetration avenues for targeted delivery to the posterior eye segment [Image reproduced from [18].

Intravitreal injection, direct penetration of the intraocular tissues using a needle and syringe as shown in route (c) in Figure 2, is currently the most popular administration route for the family of anti-VEGF (vascular endothelial growth factor) compounds that are currently showing clinical efficacy against AMD. Intravitreal injections must be performed every 4-6 weeks and are painful and have associated risks and side effects as previously mentioned.

Transscleral delivery, as shown in route (d) in Figure 2, has been identified as the most promising delivery option. The vascularised choroid is considered the rate-limiting barrier for transscleral delivery for most drugs [20]. In general,

hydrophilic, anionic drugs have better transport across the sclera into the inner layers while lipophilic and positively charged solutes may slow down and form a plug, a slow release drug charge, at the Bruch's membrane layer - the innermost layer of the choroid preceding the internal neural retina [20]. If the retina is the target, the retinal pigment epithelial cells may further attenuate transport as it has been widely demonstrated that these cells represent a significant barrier to macromolecular transport [21, 22]. Thickening of the Bruch's membrane with age, in addition to lifelong accumulation of matrix components, further contributes to decrease in solute permeability across the internal membranes [23]. Age-related vitreous degeneration, marked by significant liquefaction of the vitreous humour, may also lead to enhanced convective flows causing more rapid clearance of drug solutes in elderly patients with pockets of liquefied vitreous [24, 25]. However, the actual rate of molecular transport of a particular drug across the sclera will be dependent on compound's solubility, molecular weight/molecular radius, charge and polarity [26]. It has been observed that transscleral permeability does not noticeably change with age [26].

2.2.3. Engineered Systems for Posterior Eye Drug Delivery

One objective of ocular drug delivery research is the enhancement of ocular permeability to drug solutes in order to extend duration of pharmaceutical action while reducing risks for complications and the need for frequent injections - which can be an artifact of both the mode of drug administration and

patient non-compliance [27]. As such, drug loaded polymers have been developed as an "off-the-shelf" solution to obtain stable and predictable drug release rates based on both the pharmacological properties of the drug and the physicochemical properties of the polymer matrix [28]. However, drug-loaded polymer implants still require some level of invasive surgery. These are most often inserted in the pars plana – the area posterior to the lens but anterior to the retina – in order to circumvent the blood-ocular barrier to obtain constant release rates at the target tissues with a concomitant reduction of total drug volume requirements [29-31].

Both degradable and non-degradable polymers have been used for ocular drug release. Non-degradable implants for posterior disease treatment, such as Bausch & Lomb's Retisert®, a polyvinyl alcohol and silicone copolymer for release of fluocinolone acetonide for uveitis, and Bausch & Lomb's Vitrasert®, an ethylene co-vinyl acetate and polyvinyl alcohol matrix for ganciclovir release to treat retinitis, have risks typically associated with intravitreal injection such as endophthalmitis and retinal detachment and require surgical removal [29, 30]. They are reservoir type devices whereby a drug charge is slowly released across a semi-permeable polymer membrane offering near zero-order release after steady-state concentration profiles are established across the membrane [28]. In contrast, degradable polymers are typically made up of synthetic aliphatic polyesters of the poly-α-hydroxy acid groups including polyglycolic acid (PGA), polylactic acid (PLA) PGA/PLA copolymers and polylactic-*co*-glycolic acid

(PLGA) [28]. Degradable implants can also often have an undesirable "burst" effect in release kinetics at the end of the implant life. Drug release rates from degradable implants is a function of the available surface area of the device, the mass of drug loaded and the loaded drug's water solubility and kinetics of polymer degradation [32]. Release typically follows pseudo first-order or square root time kinetics and follows a three-phase release pattern over device life: burst release due to initial release from the surface adsorbed drug layer, followed by a slow release governed by combined passive diffusion and chain scission (due to hydrolytic cleavage which increases polymer porosity and surface area), followed by a final burst release due to total degradation and mass loss of the polymer matrix although it is often desirable for the drug payload to be completely spent prior to this final phase [28].

A number of drug encapsulation methods using degradable PLA and PLGA microspheres/nanospheres for targeting to the posterior eye have also been reported [33-39]. Intravitreal injection is the delivery mode of choice for intraocular particle delivery, however vitreal clouding leading to blurred vision can be problematic as the particles sink [40]. Intravitreal injections of polylactide nanoparticles encapsulating fluorochromes rhodamine and Nile red were phagocytosed to subsequently stain the retinal pigment epithelial cells (RPEs) over a period of 4 months [38]. Particles may also be delivered transsclerally as both delivery of protein-kinase C based PKC412 pegaptanib, for treatment of choroidal neovascularisation, were therapeutically effective

after prolonged release over several weeks [41, 42]. Liposomes, lipid vesicles 25-10,000 nm in diameter fabricated from natural lipids, offer another biocompatible and degradable method of drug encapsulation of either hydrophilic or lipophilic drugs for intraocular delivery [43]. Additionally, polymer and lipid based drug systems are amenable to chemical surface modifications to preferentially bind the particles to actively angiogenic vessels allowing for the targeting and inhibition of leaky blood vessels. As an example, the ocular liposome-based drug Visudyne®, or Verteporfin, selectively binds to neovascularized tissues following IV infusion [44]. Red light activation in the eye directed towards the retina using a laser destroys and seals leaky blood vessels. However, this treatment is controversial as it may stimulate further angiogenesis and require more frequent intervention for disease control [44]. Again, disadvantages such as ocular clouding and macroscale injection of particles may result in complications.

Other drug delivery methods using drug-loaded episcleral implants, fibrin sealants, and in-situ gelation polymers, while effective, only actively target the proximal tissue site with the engineered rate of drug release offering a mostly non-controllable and passive mechanism for solute flux [45-48]. Moreover, these devices require painful and inconvenient macroscale injection for deployment of the drug, surgical intervention for administration/removal of the device and associated clinical risks these devices. A method of active delivery,

with control over dispensed flow rates with capabilities for tissue targeting to the posterior segment has not been developed to date.

2.2.4. Introduction to Microfluidics

In microfluidics and MEMS (microelectromechanical systems) devices, small volumes of fluids, solvents and reagents are transported and manipulated using integrated microchannels and microcomponents such as valves, pumps, and mixers, embedded on a chip [49]. Early motivation to purse microfluidic devices arose from the notion that fluid handling on the cellular, protein and nucleic acid length scale could be made more efficient with devices that required on-scale small sample volumes [50]. Microfluidic devices offer a number of advantages: minimized consumption of expensive purified biological reagents, parallel applications, reduced chemical reaction time as a result of the large surface-to-volume ratio in microchannels and on-scale handling of cells [51]. As the system size decreases, diffusion, surface tension and viscosity dominate as forces that are significant at a macroscale dimension, such as gravity and inertia, become more insignificant [50].

2.2.5. Microsystems for Drug Delivery

BioMEMS is a modern term used to describe a class of microdevices specifically designed for use with biological based analytical, diagnostic and therapeutic applications using methods obtained for the microelectronics and

integrated circuit (IC) industry. BioMEMS based drug delivery encompasses a range of technologies using these fabrication techniques to deliver and maintain drugs in a therapeutic window at the site of intended biological function [52]. MEMS based technologies, previously used to produce small scale devices on the micron scale with integrated sensors, switches, filters and gears, have yielded a wide array of devices for drug release ranging from silicon immunoisolating capsulation of insulin-secreting pancreatic cells for selective release of glucose, nutrients, oxygen and carbon dioxide, microfabricated microneedle arrays for transdermal permeability enhancement, implantable micropumps for long term in-vivo controlled release to micromolded silicon based reservoir release systems that deploy drugs upon application of an anodic potential[53-59]. One particular design involved a resorbable polymeric minidisc (480 - 600 μm in thickness) fabricated from PLA poly(lactic acid). The disc contained reservoirs each having a volume of 130 nl. A 6 x 6 array of reservoirs was patterned onto the 7 X 7 mm^2 surface of the PLA disk with each reservoir possessing a membrane fabricated from copolymers of PLA and PLGA poly(glycolic acid). Based on the ratio of individual monomers within the membranes, release could be tuned to deliver pulsatile ejection of the contents of the reservoirs in vivo as the degradation time of the membranes varied with each ratio thereby implementing a timed release of drug [52].

2.3.Limitations in Previous Research

Sections 2.2.2 and 2.2.3 discussed some of the limitations with current ocular delivery systems. Additionally, intravitreal injections possess first order kinetics resulting in initially excessive concentrations of drug followed by rapid clearance to diminished concentrations below therapeutic efficacy levels; as these injections results in very short half-lives of the drug, repeated bolus delivery is required [27]. As previously mentioned, side effects are common with intravitreal injections and with most of the implantable devices as retinal detachment, and intravitreal hemorrhaging may also occur [27].

With respect to microsystems-based drug delivery approaches, conventionally microfabricated drug delivery methods use substrate materials that require plasma based ion etching, e-beam metallization, x-ray lithography, injection molding, polysilicon micromolding, laser cutting, electroplating, casting, hot embossing, investment molding and x-ray/electron beam lithography - methods that are both time, training, equipment and capital intensive [60]. This constrains many microfabricated devices to silicon or metal substrates. Casting micromolded PDMS from photolithographically defined silicon masters offers a more convenient and biocompatible approach and is a widely utilized tool for rapidly creating microfluidic devices for therapeutic, analytical and diagnostic applications [61]. Unlike traditional materials such as silicon and glass commonly used for microfabricated devices, PDMS is a low cost material and PDMS processing techniques are simple and rapid when compared with conventional wet and dry

plasma etching, UV photolithography, bonding and chemical vapor deposition approaches in microfabrication [62].

Chapter 3 Compliant PDMS Backed Microneedles for Drug Delivery

3.1.Conceptual Idea

The objective of this thesis was to address the shortcomings of current methods of therapeutic delivery to intraocular tissues through the design and development of a device to deliver model drugs to the posterior eye. Specific device design requirements, along with proposed approaches to achieve these, were developed by identifying limitations of existing methods of delivery as discussed in previous sections. The goal was to find an optimized solution to capture those objectives.

After review of the related literature, it was hypothesized that hollow glass microneedles coupled to a flow rate source and embedded in a supportive precision-micromolded flexible PDMS substrate would satisfy each of these objectives. Microneedles, miniaturized needle-like structures on the order of 100 µm – 1 mm were selected because their smaller dimensions offer a less invasive and pain-free mode of drug injection into biological tissues while the volume dispensing capabilities are more on-scale with long term controlled dosing to the back of the eye – an improvement over macroscale stainless steel needles currently used that deliver a single payload of drug every 6 weeks.

Specifically, glass (fused silica) was selected as a suitable material both for its inertness in biological fluids and for its ease of compatible low cost manufacturing processes. It was hypothesized that coupling of rigid, glass microneedle into a soft and flexible housing would provide a method to couple the

strength and rigidity of conventionally microfabricated microneedles required for tissue penetration with a soft, flexible substrate that can conform to underlying biological tissues. A prototype of the conceptual idea shown in Figure 3 was constructed. The approach would provide the required technological shift away from rigid microfabricated devices that do not conform to biological tissues to a more flexible and implantable platform.

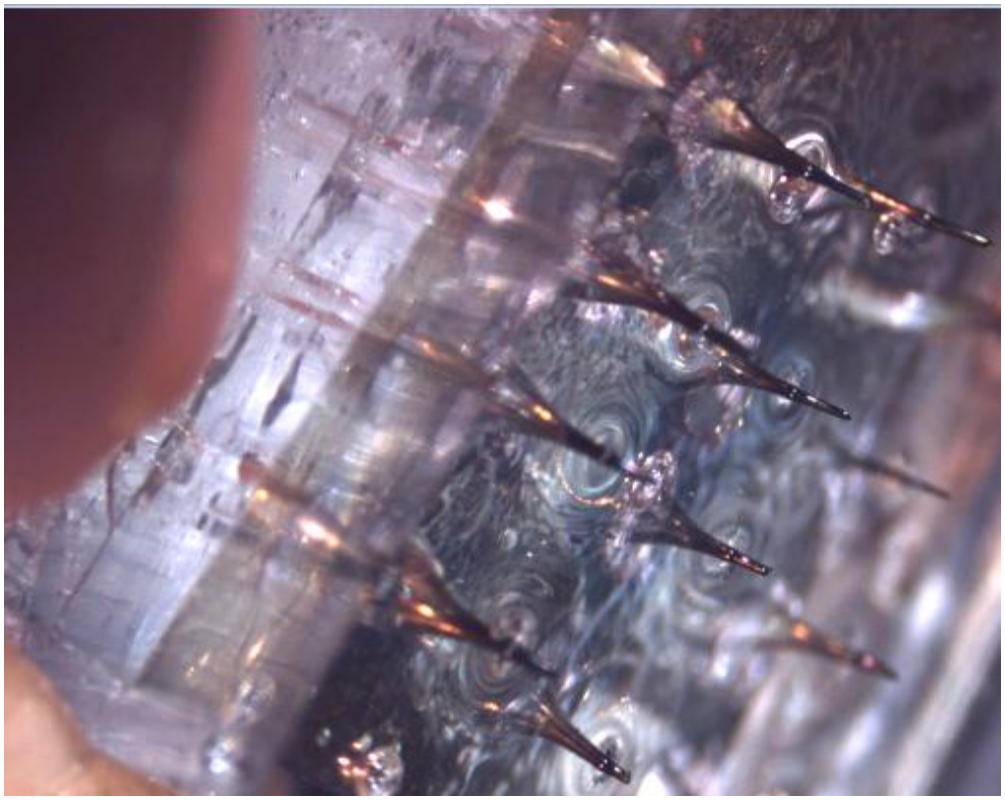

Figure 3. Image shows a conceptualized prototype of a microneedle based drug delivery device. Rigid, hollow, glass microneedles with sub-micron sized tips are arranged in a precisely spaced two-dimensional array and embedded in a flexible elastomeric platform that can conform to underlying tissues in biological applications.

3.2.Design Approach

3.2.1. Microneedles for Drug Delivery

Historically, microneedle arrays have formed the basis for transdermal drug delivery systems for the delivery of exogenous substances that do not normally traverse the skin. Microneedles are akin to macroscale hypodermic stainless steel needles, however with dimensions on the microscale: 100 μm to 1 mm in length. These dimensions are sufficient to penetrate the subcutaneous layer of skin while sparing the nerve layer thereby alleviating pain associated with macroscale needles that are several centimeters in length and several hundred microns in diameter [63].

The major advantage of microneedle based transdermal drug delivery systems is that serum drug levels can be maintained within a therapeutic range for extended time periods, something not possible with conventional injections. Furthermore, drugs that would be rapidly eliminated from the body can be released in timed intervals so that clearance and metabolism of drugs with short half-lives can be averted [63]. Microneedles containing a hollow core can also provide a conduit for drug delivery driven by pressure gradients or by diffusion [64].

Hollow glass microneedles inserted underneath the skin of diabetic rats microinjecting insulin over a 30-min infusion period resulted in a 70% drop in pre-perfusion blood glucose levels over a 5 h period [65]. A single microneedle,

the cross-sectional width of a human hair, was used to painlessly sample 200 nanoliters of blood to measure blood glucose levels in humans [66].

Henry *et. al*., were the first to demonstrate a dramatic increase of calcein permeability in the skin, as much as 4 orders of magnitude, through sections of human epidermis that were pierced with arrays of 150 μm tall solid silicon microneedles, Figure 4 [61]. This remarkable increase in permeability to calcein, a molecule that typically crosses the skin very slowly, was attributed to the approximately 1 μm diameter pores left behind in the epidermis. The authors highlighted the fact that technologies that can increase tissue permeability even 1-2 orders are seldom seen in drug delivery research emphasizing the potential utility for microneedles as a non-invasive and effective delivery vector for macromolecules[61].

Microneedles were made using standard photolithographic patterning on chromium to form arrays of dots as a protective mask during the subsequent gas-phase etch process. Reactive ion etching was performed for several hours in a rate controllable chamber with an SF_6/O_2 plasma to remove underlying silicon, not protected by the chromium masks, to yield an array of high aspect ratio microneedles. These microneedles had ultra-sharp tips and easily pierced sheets of human skin.

The skin is comprised of three layers: the stratum corneum – formed of compacted dead cells which establishes the primary barrier to drug diffusion (typically 10 -15 μm thick), the living epidermis – which is avascular and

comprised of living cells and nerves (50 – 100 μm thick) and the dermis which forms the thickest highly vascularised and highly innervated layer of the skin [67]. As such, microneedles penetrated sufficiently deep to create microchannels across the stratum corneum followed by subsequent rapid diffusion into the underlying tissues without reaching nerves found in the deeper tissues [68, 69].

This was further confirmed by using the micromachined silicon microneedles on human test subjects to determine if any sensation could be detected. Test subjects reported sensations equivalent to a mild pressure during insertion followed by removal sensations akin to removal of tape from the surface of the skin. No swelling, infection or other reaction was observed in the days following treatment confirming the microneedle as a useful tool for pain-free drug delivery.

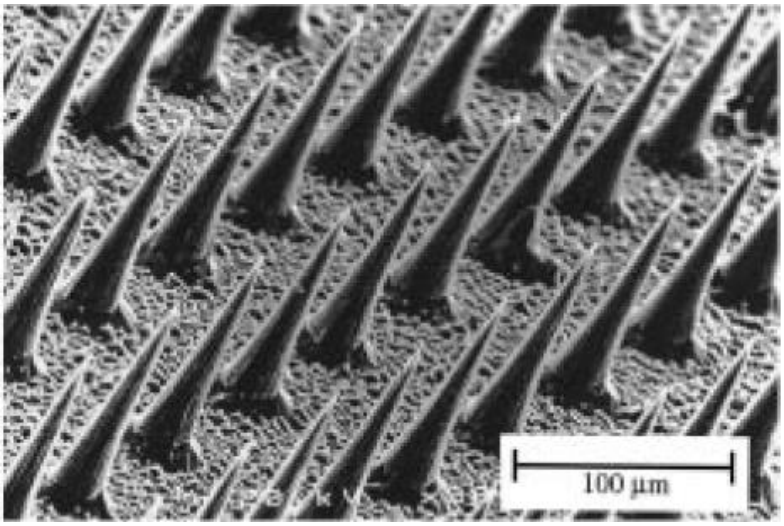

Figure 4. 20 x 20 array of silicon microneedles fabricated using photolithographic and reactive ion etching (RIE) methods Image reproduced from [61].

Prior to this first study in drug delivery, the earliest concept of using microneedle-like projections coupled to an on-chip drug reservoir for subcutaneous macromolecule penetration was reported in a 1976 patent application by inventors at Alza Corporation [70]. However, as high-volume IC fabrication technologies were not fully developed until later years, actual demonstration of such a device had not been pursued until Henry *et al.* in 1998 [61]. From these early studies, there was increasing collaborative interest among the microfabrication and drug delivery communities to develop microneedles and microneedle arrays for pharmaceutical solutions that extend beyond transdermal applications [71]. The technology launched widespread interest from various biological and microfabrication research groups to develop new methods and materials for microneedle fabrication for transdermal delivery of drugs that ordinarily do not cross the skin – particularly due to its relatively painless application.

As numerous approaches have been described for microneedle fabrication in a variety of shapes, sizes, materials and configurations – they are generally grouped based on their geometry (solid, hollow, flat, and sharp), material (metal, silicon, degradable/non-degradable polymers such as PLA, PGA, PLGA, and PVP and dissolving polymers such as maltose) and planar arrangement (in-plane and out-of-plane) [60].

The next several sections briefly review these approaches.

3.2.1.1. Silicon Microneedles

As mentioned, microneedles have been mostly fabricated using UV photolithographic based processes in clean-room facilities in association with wet chemical etching, dry reactive ion etching (DRIE)/ion-beam milling and thin film deposition processes using physical and chemical vapour deposition methods of SiO_2, SiN and other compounds followed by additional isotropic/anisotropic etching methods for geometric definition of multi-layered devices [60].

The first microneedles fabricated for drug delivery were in-plane, needle-like projections parallel to the plane of a substrate and made from single-crystal solid silicon using high precision instruments and methods from the microelectronics/integrated circuit (IC) industry [72, 73]. In contrast are out-of-plane microneedles that are oriented perpendicular to the substrate which are more amenable to fabricating batch processed microneedle arrays using photolithography, thin-film deposition and wet/dry chemical etching [74].

The earliest microfabricated microneedles were in-plane silicon structures that have been well characterized for pressure/flow profile and also for insertion forces, however, the needles were also extremely sharp, with very long taper lengths potentially causing pain during insertion [73]. Since the earliest in-plane formats, most technologies developed the out-of-plane configuration.

Table 1 lists the major categories of silicon based microneedle systems.

Table 1. Major classes of Si microneedles categorized by configuration

Configuration	Dimensions	Fabrication Processes	Ref
Single in-plane hollow single- and poly- silicon probes and microhypodermic needles	1-6 mm length; 30-140 µm width with 10-32 µm wide and 9-15 µm deep microchannels for fluid injection;	Multiple steps of patterning protective oxide/nitride layers for selective etching; boron diffusion, anisotropic etch; thermal oxidation and dielectric LPCVD and isotropic etch for structure release; RIE (polysilicon molding)	[72, 73, 75]
Solid out of plane silicon microneedle arrays	150 µm tall; 80 µm base with 1 µm tips; 20 X 20 arrays with 150 µm center to center spacing	LPCVD deposited oxide onto Si, CF4-CHF_3-He plasma etching of oxide layer, DRIE for hollow channel definition, LPCVD nitride deposition, SF_6 isotropic plasma etch, wet HFetch/ removal of SiN/SiO; DRIE for pillar definition	[61, 63]
Hollow out of plane silicon microneedle arrays	20 -100 µm internal channel diameter , 100-400 µm height and 150 - 750 µm spacings; 10 X 10 , 20 X 20 arrays	Isotropic/anisotropic etching, CF_4-CHF_3-He plasma, LPCVD SiN, DRIE, wet HF etch; DRIE and UV photolithography; ICP Etcher	[63, 74, 76-78]
In-plane hollow microneedle array	2 mm length, 100 µm thick and 200 µm width 20 µm internal bore diameter; cone angles 8.5 – 30°;	Anisotropic dry etch, sidewall passivation via thermal oxide or LPCVD nitride deposition, isotropic SF_6 dry etching, LPCVD polysilicon deposition.	[79]

3.2.1.2. Metal Microneedles

Though microneedles were initially processed in silicon using silicon-compatible clean room processing techniques, metal was shown to also be an effective material to form arrays that could penetrate skin - at much lower costs [60]. Metals such as stainless-steel, titanium, palladium and nickel have been used as structural materials for microneedle arrays as shown in Table 2.

Table 2. Major classes of metallic microneedles categorized by configuration

Category	Dimensions	Fabrication Processes	Ref
Single- and Multiple-metallic microhypodermic needle design	Single or multiple needle option:200 µm - 2 cm length; cross-section of 70 – 200 µm width and 75-120 height; Tip ~ 15 µm x 15 µm; Inner lumen area: 10 X 10 µm and 5 X 5 µm square	Palladium, palladium-cobalt alloys, and Ni electroplating onto Si, UV photolithography, sputtering and wet etch release	[80, 81]
Hollow metal microneedle arrays	120-400µm height, 80 µm base dia. with 1 -75 µm tips; 40 µm bore ID; 10 X 10 and 20 X 20 array with 150 µm center to center spacing; Tip ID 33.6-101 µm; cone angle ~ 5°	Casting of SU8 epoxy over solid silicon microneedle molds; sputter coating with Ti/Cu seed layers and metal electroplating; UV exposure, O_2/CHF_3 plasma RIE, SF6 plasma; UV-LIGA processes, double-layer Cr/Cu/Ni electroplating, O_2/CF_4 dry plasma etch; excimer laser and electrodeposition	[65, 76, 82-84]
Solid metal microneedle arrays (for piercing)	300, 550, 700 and 900 µm	30G stainless steel hypodermic needles in a 4 X 4 polyetherketone mold at 1.25 mm pitch; needles were inserted to height and cut and affixed to applicator	[85]
Single drug coated solid metal microneedles	500 – 750 µm; 200 X 50 µm width; cone angle 55°	Infrared-laser cut 75 µm stainless steel sections	[86, 87]

3.2.1.3. Polymer Microneedles

Microneedles have been fabricated from a range of polymers as they possess sufficient strength and toughness for penetration, have associated low-cost processing techniques (molding and casting) and can be made in both degradable (or dissolving)/non-degradable configurations as briefly summarized in Table 3 [60].

Table 3. Examples of polymeric microneedles categorized by configuration

Configuration	Dimensions	Fabrication Processes	Ref
Solid biodegradable PGA, PLA, Polylactic-co-glycolic acid arrays	400 µm- 1.5 µm tall; 120 – 225 microneedle array; 100 – 200 µm base diameter	Polymer melts cast in PDMS micromolds casted from solid silicon masters at 150 – 250°C under vacuum; micromolding with SU-8 or polyurethane masters to cast PDMS followed by the PGA, PLA and copolymeric microneedles.	[65, 88]
Solid drug-loaded dissolving PVP microneedle arrays; dissolving maltose arrays	150-750 µm length, 250 µm base and 5 µm tip radius	Micromolding with SU-8 to crease reverse PDMS molds; photopolymerization of liquid monomeric vinyl pyrrolidone to yield polyvinylpyrrolidone (PVP) microneedles; maltose arrays cast on metal molds	[89, 90]
Hollow SU-8 polymer microneedle arrays	6 X 6 array 1mm tall; side opened 150 µm lumens	UV photolithography and single-step micromolding techniques	[91]

3.2.1.4. Glass Microneedles

Recently, fabrication methods for ocular drug delivery have exclusively employed a commercial pipette puller to make stand alone microneedles to demonstrate delivery to the eye [92, 93]. Table 4 lists the primary, and essentially only, current method of microneedle fabrication using commercial pipette pullers.

Table 4. Glass microneedle fabrication using the drawn glass method

Category	Dimensions	Fabrication Processes	Ref
Hollow glass microneedles	Tip OD 10 – 22 µm, tip ID 7 – 40 µm (up to 100 µm if bevelled), taper lengths several mm; cone angles 20 - 30° (with beveller); Height in general difficult to quantify due to long tapers	Drawn glass using commercial micropipette puller	[92, 94-98]

3.2.2. Fabrication of Glass Probes for SNOM

A new and simple method of microneedle fabrication was identified by co-opting chemical etch methods used to make electrospray ionization-mass spectrometry (ESI-MS) emitters from hollow capillary tubing [99, 100]. It was hypothesized that the process could yield hollow microneedles that would yield sufficient tapers that would be strong enough to penetrate the sclera.

The chemical etching method generates tapered tips which are fabricated by vertically inserting one end of a hollow fused-silica capillary tubing, stripped of its native polyimide coating, into an aqueous solution of hydrofluoric acid (HF) [100]. In order to preserve the original inner diameter of the capillary tubing, water is pumped through the inner bore - a technique first performed by Emmett *et al*. to fabricate microelectrospray tips as shown in Figure 5 [101]. As a result of the chemical etch, the resulting structures have outer diameters of 360 μm terminating at a tip of 20 μm with a constant inner bore - dimensions equivalent to the starting dimension of the capillary tubing.

The probes had very high aspect ratios (ratio of the length of the taper to the unmodified base) as the probe tip is produced at an air/etchant interface where surface tension forces cause the etchant to rise along the outer diameter of the tubing [99]. This gradient in etch rate, where etch rates decrease with distance from the bulk solution, produces a characteristic taper at the air-HF interface [100]. The process is self-terminating as the glass in contact with the

etchant was fully consumed by the etchant enabling a highly reproducible process.

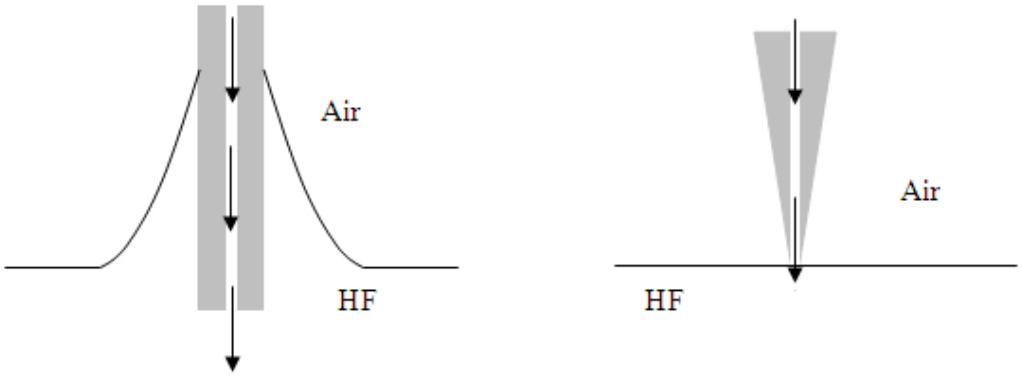

Figure 5. Fabrication of tapered tips using air-etchant surface tension effects to make hollow electrospray nanoemitters. Water is pumped through the inner bore, indicated by the arrows, to prevent HF influx and enlargement of the native inner bore [99].

As many of the desirable features for these emitters such as well-defined cone angles, a hollow bore for solute delivery, tapered tip geometries and smooth surface finishes, were deemed relevant for microneedle functionalities, the method was hypothesized to serve as an economical method of microneedle fabrication for ocular drug delivery.

The first documented use of an acid etchant for the formation of tapered glass structures was first described for the fabrication of glass micro-dissection needles used for the isolation of yeast ascospores [102]. After pulling 3-mm diameter glass rods, HF was used to gradually etch ultrafine fragments of the pulled glass until a sharp, well-defined point was reached. A 50% solution of

hydrofluoric acid was used for the stepwise etching process that resulted in the controlled formation of a gradual taper terminating in a single sharp point.

Chemical etching via surface-tension forces at the interface between glass fibers and hydrofluoric acid (HF) is also the most common method of rapid, convenient, inexpensive and repeatable fabrication of sharp, tapered conical shaped-aperture optical probes with ultra-fine points, using solid core optical fibers, with sub-wavelength tip diameters for high resolution imaging applications such as SNOM (scanning near-field microscopy) [103, 104].

Known as Turner's Method, the formation of the tapered geometry was due to the dynamic positional change of the interfacial meniscus between an organic overlayer and the acid etchant due to the reduction of the diameter of the glass fiber being etched. The procedure yields tapered points from a symmetrical cylindrical fiber by placement of the fiber into a biphasic solution of an acid etchant and an immiscible, lower density liquid overlayer that is inert to the quartz fiber and acid etchant. The selected overlayer is typically an organic solvent or oil and serves a number of purposes. The overlayer allows for a self-terminating process by protecting the tip from further etching reactions [105]. The overlayer also prevents evaporation of the etchant thus providing a constant etchant composition and volume as changes in etchant composition would affect etch rates of the glass while a volumetric decrease could lead to distortion and uneven geometry of the resultant cone [105]. Corrosive vapor etching of the bulk fiber is also averted with the overlayer.

As etching proceeds, the fiber diameter in contact with the etchant is subsequently decreased with an associated reduction of upward pulling forces [106]. As a result, the height of the meniscus gradually falls until the segment of the tip residing below the oil is completely removed. The process is self-terminating as the final formed tip is protected in the inert organic overlayer. No mechanical processing and a reliable inherent etch-stop mechanism makes this process reproducible between each tip fabrication run.

The previous discussion so far is based on etching of solid core fibers. In order to fabricate microneedles suitable for drug delivery, it was mandatory to have a hollow bore within the tapered structure to provide a conduit for fluid flow. A microsurgical tool for intracytoplasmic injection was fabricated using a modified Turner Method to fabricate a cell microinjector with a hollow bore with a 2 μm tip inner diameter [107]. The microinjectors were fabricated by immersing 5-cm segments of polyimide-stripped silica capillary tubing (Polymicro) into 49% HF solutions capped off by a layer of silicone oil. The oil-filled tubing is then placed vertically into the HF for the etch. As the glass is consumed, the outer diameter decreases reducing the surface tension forces. The height of the meniscus subsequently falls until the etching front coincides with the central axis of the capillary terminating in a single, sharpened point [107].

Methods described using Kelly *et al*. improved on Wong's approach by avoiding introduction of oil into the inner bore which can contaminate or compromise the interior surface for end-use applications – and instead pumped

water through the bore. The technique was extended to batch fabrication of tapered structures by constructing an aluminum holder to etch 19 aligned capillary tubings in a single etch operation using 49% HF [99]. Water pumped at a total combined rate of 1.9 μL/min allowed formation of arrays of tapered capillaries with uniform dimensions and tapers. The authors note that capillaries were positioned at fixed distances to ensure that each structure formed its own meniscus allowing each tubing section to be independently etched.

A different approach used a rotating bath of HF to reduce the time to etch optical fibers into tapered tips [108]. By placing the fiber in the center of the liquid surface where the height was reduced as a result of angular motion, the etch time was reduced from 120-140 minutes using a static etch to 20-30 min using the rotating bath. The resultant fiber possessed ultra smooth and symmetrical tips when compared with statically formed structures. The faster etch rate was attributed to the constant level of the reduced etchant surface position relative to the fiber position [108].

Wong *et. al* have proposed that tip formation is a result of the height of the meniscus being dictated by the force balance between the downward weight vector of the etchant and the upwards pulling force due surface tension [107]. As the etching process progresses, the height of the meniscus gradually falls in an attempt to continuously balance the upward pulling force created by the surface tension of the etchant with the weight of the etchant in contact with the tubing [109]. The meniscus drop occurs at the point where the weight of the solution

(the etchant plus products of reaction) exceeds surface tension forces. The meniscus then falls to the next equilibrium point where the surface tension force balances the liquid weight of the new meniscus.

Based on their model, tip geometry can be tuned by adjusting the physical variables that govern the force balance in the system – namely the surface tension, the difference in densities between the etchant and overlying reagent and the contact angle at the liquid/liquid interface. These can be altered by varying the organic overlayer, the concentration of the acid etchant and the temperature [110-112]. Specifically, the meniscus height is a function of the meniscus formed between the HF along the fiber at the interface of the HF/solvent/fiber. This height is dependent on the interfacial tension, fiber diameter and the density difference between the immiscible solvent and acid etchant [113].

Cone angles and taper lengths show an inverse relationship as well with increasing HF concentration - lower HF concentration results in tip geometries showing sharper cone angles (smaller angles) with longer tapers while etching at higher HF concentrations above 40% results in larger cone angles with shorter taper lengths[110]. Etch rates also increase quadratically with increases in HF concentration [110]. Lower concentration etches also result in poorer quality structures due to HF diffusion into the solvent and attacking the glass and affecting the quality of the etched structure [110]. Increasing temperature accelerates the etch process and further surface quality improvements result. The

final resultant geometry is a function of the solvent type, acid concentration, etching speed and etching temperature [110].

Hoffman *et al.* further argued that while different cone angles were obtained by etching optical fibers in HF with a variety of water-immiscible solvents, shown in Table 5, there was no immediate relationship between surface tension of the solvent or density with the observed cone angle [112]. The theoretical determination of the meniscus height, the interfacial tension values between each of the phases must be known. The cone angle-dependent meniscus not only depends on the original fiber diameter but on three additional interfacial surface tensions which complicate theoretical predictions of cone angle [112].

Table 5. Density and surface tension of various organic overlaying reagents [Table adapted from Ref. [112]]

Organic Solvent	**ρ (g/cm^3)**	**γ (dyn/cm)**	**Cone Angle (deg)**
1-octanethiol	0.843	28.02	41
Isooctane	0.691	18.8	40
p-xylene	0.861	28.3	37
m-xylene	0.864	28.6	34
Dodecanethiol	0.844	-	33.5
Sunflower oil	-	-	33
Octane	0.703	21.7	32.7
Bromodecane	1.069	29.54	29
Toluene	0.867	28.4	26
Squalane	0.809	28.15	23.1
1-chlorocotane	0.872	27.65	22
Di-butyl-sulfide	0.826	-	18
Di-butyl-ether	0.767	22.9	8.5
Nitrotoluene	-	-	8

3.2.3. Basic Principles of Microscale Flow

As hollow microneedles possess internal bores with microscale dimensions, the delivery of drug solutions can be achieved across these microchannels using either pressure actuated flow or electrokinetic flow, i.e. flow actuation using an electric field. Further, either method can be used to pump water through the internal bore during the fabrication of microneedles.

3.2.3.1. Pressure Driven Flow

The modified Bernoulli equation describing macroscale fluid flow in a pipe has been previously used to model hydraulic behavior in individual symmetrical microneedles,

$$p_1 - p_2 + \rho \frac{v_1^{\,2} - v_2^{\,2}}{2} + \rho g(z_1 - z_2) = \rho f \frac{L}{d} \frac{v^2}{2} + \sum \rho K \frac{v^2}{2}, \quad (1)$$

where the subscripts denote the inlet and outlet of the bore, p_1-p_2 is the pressure drop, ρ is the liquid density, v is the linear fluid velocity, g is the gravitational acceleration, z is the hydrostatic head, K is an empirically derived coefficient for minor losses, f is the friction factor and d is the diameter of the microchannel [114]. Assuming a constant diameter cylindrical bore and negligible gravitational effects on the microscale, the equation can be simplified to the following equation assuming f = 64/Re for laminar flow:

$$\Delta p = \mu \frac{128}{\pi} \frac{q L}{d^4} + \rho \frac{8}{\pi^2} \frac{q^2}{d^4} (K_1 + K_2) \quad (2)$$

K_1 and K_2 are loss coefficients for a square-edged inlet and outlet to account for minor losses in the microchannel boundaries [114] .

3.2.3.2. Electroosmotic Flow

Microfluidic devices commonly exploit electroosmotic flow for on-chip liquid transport. When a solid surface such as glass is in contact with a medium such as water, ionization equilibrium at the interface results in a mobilization of free ions in solution to reassemble near the interface to produce a narrow region of nonzero charges near that interface effectively creating a separation of charge [115]. The remaining counterions are in a diffuse layer whose density diminishes with distance from the charged solid surface - this entire region is commonly referred to as the electrical double layer (EDL) [116]. If this arrangement is placed into an electric field tangentially to the solid-liquid interface, an electrical force will be generated witin the EDL causing the ions to move - and pulling the liquid with them causing bulk flow in the microchannel follows due to viscous drag effects [115]. For steady state, one-dimensional fully developed flow , the Smoluchowski equation gives the average flow velocity as:

$$v_{av} = \frac{\varepsilon_r \varepsilon_0 \zeta}{\mu} E_z \quad (3)$$

where E_z is the strength of the applied electric field, ε_0 and ε_r are the relative dielectric constant and electrical permittivity of a vacuum, μ is the viscosity of the aqueous solution and ζ is the zeta-potential at the interface - a the electrostatic potential at the boundary between the compact layer of charges assembled at the solid surface and the diffuse layer of counterions [115].

3.3.Device Design

3.3.1. Design Criteria and Material Selection

3.3.1.1. Microneedle Material

The microneedle material should possess sufficient rigidity to penetrate the sclera without breakage and fracture. Further, the chosen material should be generally accepted as compatible for implantation within the ocular tissues without adverse effects such as inflammation and infection. The material should be inert and non-degradable in biological tissues.

3.3.1.2. Microneedle Dimensions

The dimensions of the microneedles should fall within a height range of between 300 μm (transscleral) to 1.1 mm (intravitreal) to reach the range of tissues found in the region of the posterior segment of the human eye [17]. The outer diameter of the microneedles should be minimized to mitigate

associated pain sensations upon insertion. There are approximately 8-20 short ciliary nerves residing in the sclera/uvea while the vitreous and retina do not contain pain fibers [12]. As such, minimal outer diameter dimensions would reduce the probability of nerve contact. The choroid and retina are also poorly supplied with sensory nerves [46].

3.3.1.3. Microneedle/Device Configuration

The device should be able to accommodate a range of configurations: from a single microneedle format (if sufficient therapeutic delivery volumes are met) to multiple microneedles, i.e. an array, if a single needle is inadequate for required dosing for therapeutic efficacy. As conventionally microfabricated microneedles are typically batch processed to manufacture arrays, the developed process should consider multiple microneedle formats.

3.3.1.4. Device Substrate Material

PDMS was selected as the material for the microneedle housing as complex microfluidic devices can be fabricated quickly, easily and inexpensively using soft lithographic techniques [117]. Soft lithography refers to a set of procedures such as microncontact printing, casting, injection molding and embossing used to manipulate elastomeric materials to creaste micros- and nano- scale structures [49]. PDMS also provides an excellent

substrate for high fidelity replication patterning, down to 280 nm sized features, is cheap, displays low toxicity, is widely available, optically transparent in the visual and near-UV regions, chemically inert, mechanically flexible and durable and can easily withstand sterilization temperatures of up to 120°C (a requirement for biological implants) [49, 118]. As the field of microfluidics continues its rapid development in the context of biological applications, it has been noted that polymeric systems will replace traditional silicon based microsystems due to low processing and material costs, minimum time to realize many devices using replica molding (the ability to produce hundreds of relief structure replicas in PDMS of the opposite pattern constructed on a silicon master wafer), the ability to modify and implement design changes rapidly and easily and the flexibility of altering the surface in response to a particular application [118, 119]. PDMS is also non-toxic to cells and proteins [118].

PDMS contains repeating monomer units of $–O\text{-}Si(CH_3)_2$ groups with a naturally hydrophobic surface due to orientation of vinyl groups in an air medium. Exposure to oxygen plasma changes the surface to hydrophilic by introducing surface silanol (SiOH) groups in place of the $SiCH_3$ groups [120, 121]. The surfaces remain hydrophilic indefinitely when placed in contact with water or organic polar solvents. These surface silanol groups also render the surface easily mutable with a wide range of silanes (Si-R) that have important functional terminal end groups that can be used to introduce other

reactive groups for surface functionalization of innumerable biological and synthetic compounds [122]. The Young's Modulus of PDMS is 700-900 kPa [62].

Further, the bond between the microneedles and PDMS should withstand typical forces of tissue penetration. It is expected that microneedles should withstand multiple insertion and withdrawal cycles from tissue without delamination from the PDMS substrate or tissues themselves.

3.3.1.5. Control over Delivery Rates

Rates should be controllable and be independent of both material selection and model compound. This will be achieved by active pumping through the inner microneedle bore to deliver solutes at fixed rates into the tissues. The actual tissue layers themselves will act as rate-limiting membranes to restrict delivery into the intraocular layers. Alternatively, direct intravitreal injection could also be achieved though at much smaller volumes than is ordinarily delivered via macroscale injection.

In this case, rates would not be restricted and would be equivalent to the dosing rate directly in the intravitreal region.

3.3.1.6. Device Dimensions

The device will be no larger than 0.5 x 0.5 cm square. Thickness will be minimized; however, thickness should be sufficient for ease of device handling.

Chapter 4 Device Fabrication and In-Vitro Drug Delivery

4.1.Fabrication Materials

4.1.1. Wafer Prep

Single 3" diameter crystal p-type <100> silicon wafers (University Wafer, South Boston, MA) were subjected to oxygen plasma using an RF Plasma Barrel Etcher PT7150 (Biorad, Hercules, CA). The plasma treatment provided a clean silicon surface in order to enhance adhesion of the photopolymer to the wafer. The plasma oxidation was performed at a reactive pressure of 0.35 mbar with a gas flow rate of 5 sccm/min at an RF power of 50 watts for 60 seconds.

4.1.2. SU-8 Photoresist

SU-8 100 (Microchem, Newton, MA), an epoxy based negative photopolymerizable resist, was spun-cast onto to the wafer using a spinner at rotational speeds outlined in Table 6 in order to achieve the desired thickness layer. To create feature sizes of 100 μm, the resist was dispensed onto the wafer by pouring and then placed on vacuum chuck on the spinner and ramped from 100 RPM to the final recommended 1500 RPM over 10 seconds. The spinner continued at 1500 RPM for an additional 30 seconds. The thickness of the layer was equivalent to the height of the micropatterned features onto the wafers. After spinning, the coated wafers were subsequently soft baked and hard baked as indicated below in Table 6.

For the 100 μm layer that was used for the devices, the resist-coated wafers were soft-baked and hard-baked according to Table 6. After the hard bake wafers were ready for UV exposure or alternatively could be stored in the clean room away from light for up to 1 month.

Table 6. Recommended spin speed for Microchem SU8-100 Negative Photoresist

Spin Table for Range of Desired Feature Thickness

Thickness (μm)	Speed (RPM)	Ramp Interval	Total Spin Time (s)
140-150	1200	From 100 RPM to Speed over 10 seconds	40 seconds
90 – 105	1500		40 seconds
80	1700		40 seconds

Pre-exposure Bake Time

Thickness (μm)	Soft Bake 65°C	Hard Bake 95°C
140-150	30 minutes	3 hours
90 – 105	15 minutes	1 hour 15 minutes
80	12 minutes	1 hour

4.1.3. PDMS

SYLGARD® 184 PDMS (Dow Corning, Midland, MI) at a 1:10 curing agent to prepolymer base ratio was poured over the master silicon molds in order to create replica structures in PDMS.

4.2.Fused Silica Tubing

Hollow flexible fused silica (borosilicate) capillary tubing (Polymicro Technologies, Phoenix, AZ) coated with polyimide was used for the starting material for all etching processes described. Supplied form the manufacturer in a range of tubing dimensions, two sizes were used: TSP010150 and TSP010375, with corresponding outer diameter (OD) values of 148 μm and 363 μm, inner diameter (ID) values of 10 μm, and polyimide coating thicknesses of 12 μm and 20 μm. Spools of tubing were supplied from the manufacturer in meter-length increments. Appendix 13.1 shows the product information for the tubing.

4.3.Methods for Fabrication and Assembly

4.3.1. UV Photolithography for Mold Fabrication

4.3.1.1. Single Mask UV Photolithography

Following the hard bake, the photoresist was patterned using UV photolithography with a Karl Suss MJB 3-400 mask aligner (SÜSS MicroTec AG, Garching, Germany). Dark-field masks to pattern the negative SU-8 photoresist were designed in AutoCad to the desired feature layout and dimensions and digitally sent to a laser photpolotting service (CAD/Art Services, Brandon, OR) for high resolution (20,000 dpi) transfer to film. The film was then cut to a standard 4” square size and affixed to a 4” square glass slide using double-sided adhesive tape and placed onto a 4” vacuum chuck print-side-down in the mask aligner to hold the photomask in place. The

spin-coated/oxidized wafer was then loaded onto the wafer chuck and aligned with the photomask using an xyz translational stage and microscope.

After planar alignment, the wafer was vertically raised until the mask and resist layer were in contact, using caution so as to not deform the resist layer. After alignment, the wafer chamber vacuum was turned on to hold the sample in place for UV exposure. Samples were exposed to UV at an intensity of 7.1 mW/cm^2 for the recommended times shown in Table 7 followed by a post exposure bake.

Table 7. Exposure, post-bake and development time for Microchem SU8-100 Negative Photoresist

Exposure Energy

Thickness (μm)	Time (seconds)	Intensity (mW/cm^2)
140-150	150	7.1
90 – 105	96	7.1
80	85	7.1

Post-exposure Bake Time

Thickness (μm)	Soft Bake 65°C	Initial Bake 45°C for 2 minutes then 65°C	Hard Bake 95°C
140-150	30 minutes	20 minutes	30 minutes
90 – 105	15 minutes	10 minutes	20 minutes
80	12 minutes	5 minutes	10 minutes

Developer

Thickness (μm)	Time
140-150	40 minutes
90 – 105	25 minutes
80	15 minutes

Sections of photoresist exposed to the UV light corresponding to the design on the photomask were permanently cross-linked and revealed by immersion in SU-8 100 developer solution after solvation of unexposed SU8 using the times outlined in Table 7 with the process shown in Figure 6. After developing, the wafers were rinsed in isopropanol. The appearance of white residue on the silicon surface indicated incomplete development. The wafer was then placed in fresh developing solution for an additional five minutes and rinsed in isopropanol until no evidence of remaining resist was visible on the surface. After rinsing the wafer in isopropanol, the wafer was then gently dried using compressed N_2 and kept covered in petri dishes to minimize surface dirt and contamination. Care was taken when drying wafers to avoid delamination of structures when holding the N_2 gun too close to the wafer. Molds were then transported from the clean room to the wet lab and used to cast all micromolded PDMS structures described.

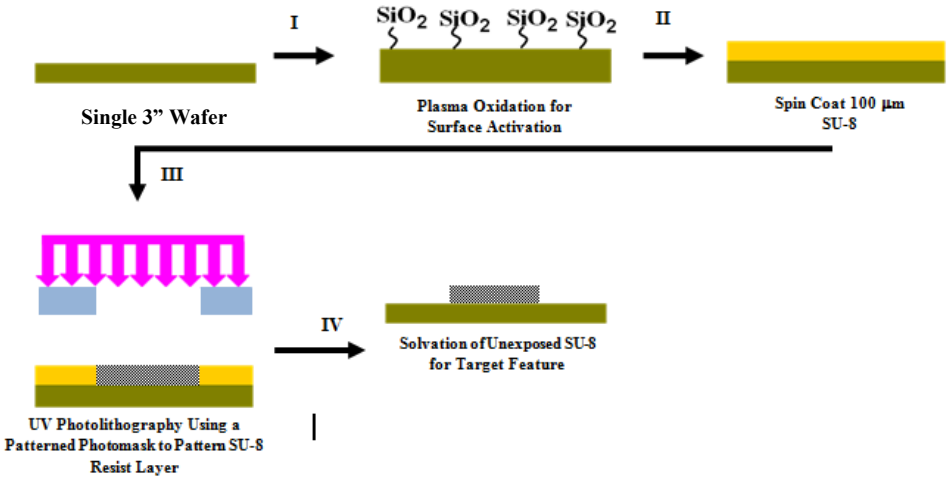

Figure 6. Process flow for single layer mask design Single mask UV photolithography showing a pristine 3" silicon wafer activated using oxygen plasma (I) for enhanced adhesion of epoxy-based SU8 photoresist spun coated (II) onto the oxidized wafer forming of a 100 µm layer of SU8 followed by (III) UV photolithography through a defined photomask allowing selective passage of ultraviolet light to micropattern the underlying resist. The target relief structures remain behind after solvation of unexposed photoresist in developing solution (IV). The mold is ready to be used to cast microstructures in PDMS.

4.3.1.2. Master Mold Fabrication Using Dual Layer Photolithography

Photolithographic processes can be done repeatedly on the same wafer to fabricate dual layered features. A two-layer mask was made for assembly using the pipette pulled microneedles. The first layer of photolithography was used to pattern a fluidic microchannel 300 µm wide and 5.0 cm long flanked by terminating 5.0 x 7.0 cm^2 rectangular reservoirs on either end. Following the first round of processing, a second round of spin-casting SU-8 100, UV photolithography and solvation was used to pattern the microchannel with a second layer of 1.0 mm diameter circular markers for precise positioning of the borosilicate microneedles with the 300 µm width microchannel as shown

in Figure 7. The second photolithographic layer was necessary for manual positioning accuracy of the microneedles as alignment of the 1.0 mm base of the glass microneedles within the microchannel would be otherwise challenging due to the smaller 300 μm dimensions of the channel and difficulty associated with visualizing micron sized features in the transparent elastomeric substrate. The circular markers were designed using the multi-layer design mode in AutoCAD in order to ensure accurate alignment of the microneedle base to guarantee fluidic coupling to the underlying microchannel without any chance of offset leading to compromised or blocked flow.

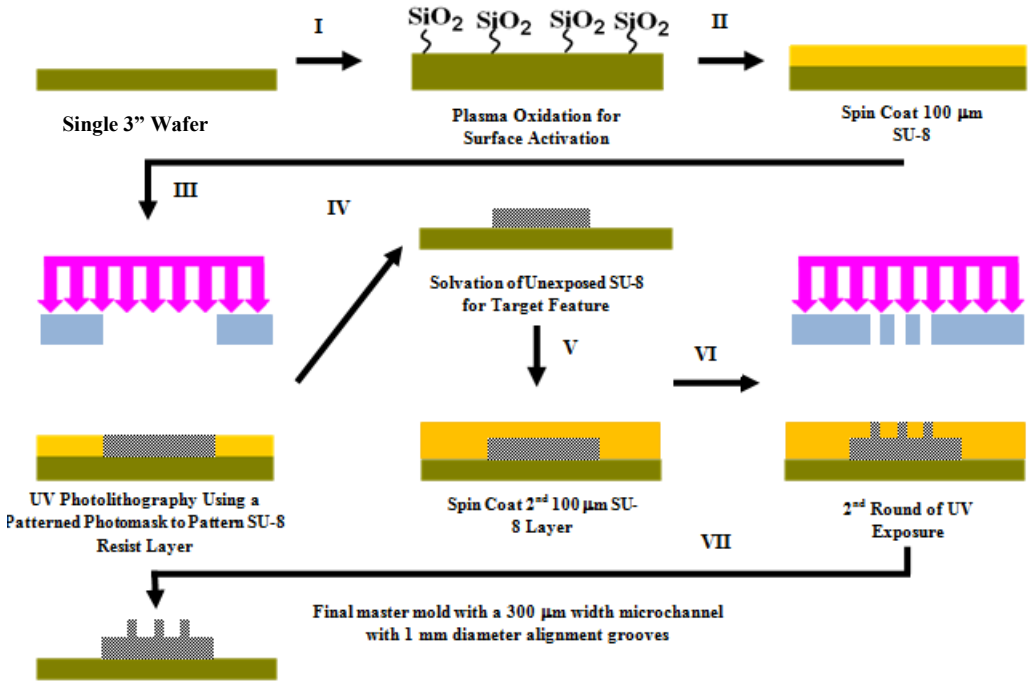

Figure 7. Process flow for dual layer mask design: a single mask UV photolithography round was first performed on a 3" silicon wafer activated using oxygen plasma (I) for enhanced adhesion of epoxy-based SU8 photoresist spun coated (II) onto the oxidized wafer forming of a 100 µm layer of SU8 followed by (III) UV photolithography through a defined photomask allowing selective passage of ultraviolet light to micropattern the underlying resist. The target relief structures remained behind after solvation of unexposed photoresist in developing solution (IV). A second layer of SU-8 was then spun onto the first patterned layer using the same processing conditions used for the first round of photolithography (V) followed by a timed UV exposure (VI) and then subsequently developed to reveal the second layer aligned on top of the first layer (VII). The mold was then used to cast multiple PDMS molds with microchannels possessing microneedle positioning markers for accurate microfluidic coupling.

4.3.2. PDMS Casting

PDMS polymer was cast by combining a 10:1 ratio of Sylgard 184 for a total of 11 mL volume (Dow Corning, Midland, MI) prepolymer base/curing agent solution and cast using a fabricated SU-8 100 master mold. The PDMS

was set to cure for 1 hour at 65°C. The negative impression of the pattern from the wafer was transferred into the bulk polymer. The patterned PDMS was then removed from the mold and prepared for assembly.

For dual layer photolithography, a second sample of PDMS at a 1:10 curing agent to prepolymer base ratio was poured into an empty petri dish to create an unpatterned circular slab of PDMS. After curing, both samples were delaminated in a clean room facility and assembled. To seal the microchannel, both PDMS sections were exposed to an oxygen plasma reactive pressure of 0.35 mbar with a gas flow rate of 5 sccm/min at an RF power of 50 watts for 30 seconds and permanently bonded.

4.3.3. Microneedle Fabrication

4.3.3.1. Pipette Puller

Microneedles were first fabricated using a pipette puller with a CO_2-laser based heat source to draw and pull hollow 1.00 mm OD/0.50 mm ID standard wall borosilicate capillaries (BF100-50-7.5; Sutter Instruments, Novato, CA) to sub-micron diameters. Microneedles were then retrieved from the pulled sections by cutting 0.5 cm lengths from the tip which were subsequently embedded and bonded onto the 300 μm width microchannels to provide a conduit for delivery into the ocular tissues.

For the prototype device, glass microneedles were made using a commonly used method of hollow glass micropipette fabrication that are

fabricated for a variety of laboratory tools such as extracellular recording probes, microelectrodes, patch pipettes, intracellular recording, microinjection needles for embryos and cells, pronuclear injection, aspiration for microhandling and ion selective electrodes (ISEs) and cell interfacing, such as injection and withdrawal (The P-97 Pipette Cookbook: 2006, revision C, Sutter Instruments, Novato, CA). The manual is freely available online.

The commercially available puller (P-97 Pipette Puller; Sutter Instrument Company, Novato, CA) was used to pull 1 mm OD / 0.5 mm ID tubing using instrument settings for Program #33, as shown in Figure 8, under the general lookup tables for a range of micropipettes using the P-97 Pipette Cookbook.

GENERAL LOOK UP TABLES: 2.5mm x 2.5mm Box Filament (FB255B)

1.0mm x 0.50mm Glass (B100-50-10)

TYPE	PROG #	Glass Item Number	LINE(S)	HEAT	PULL	VEL	TIME/DEL	PRESSURE
A	Prog. # 31	B100-50-10	Line 1, Loops(4)	Ramp	0	30	250 t	500
B	Prog. # 32	BF100-50-10	Line 1	Ramp+5	45	75	90 d	500
C	Prog. # 33	BF100-50-10	Line 1	Ramp	55	75	80 d	400
D	Prog. # 34	BF100-50-10	Line 1	Ramp+10	75	75	200t or 90d	400
E	Prog. # 35	B100-50-10	Line 1	Ramp+30	30	120	100 t	200

Standard or Thick Walled Glass
1.0mm x 0.50mm glass, 0.3µm-0.5µm Tip, 9mm taper **(400x mag.)**
▼ General Look Up Tables - Prog #33

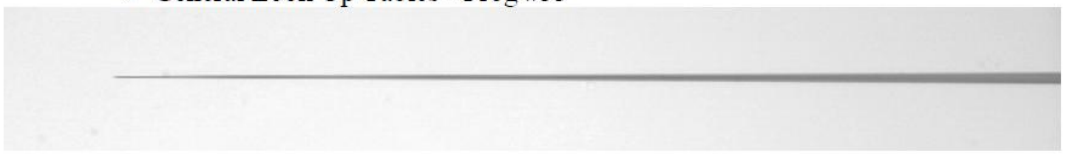

Figure 8. P-97 instrument settings for generating micropipettes with sub-micron tip diameters (The P-97 Pipette Cookbook: 2006, revision C, Sutter Instruments, Novato, CA)

The unmodified capillary tube was loaded into the holding receptacle of the P-97. The cover was then closed and instrument settings set based on the target geometry shown in Figure 8.

Schematically shown in Figure 9, the pipette puller uses an integrated continuous wave CO_2 laser to heat the mid-section of the capillary tubing while pulling bi-axially on either end of the tube to pull and draw the capillary into two micropipettes of varying taper lengths and tip dimensions [112]. The pulling force, time delay from irradiation to deformation and pull velocity can be varied to form structures of varying geometry and dimensions

[112]. The resultant tapers are very long with extremely small tip angles and as such possess limited mechanical rigidity [123].

Figure 9. Schematic showing micropipette fabrication: a single borosilicate capillary tube is pulled biaxially while heating the midpoint to 585°C to form two micropipettes with taper lengths of 9 mm and tip diameters in the range of several microns.

After pulling a set of needles, the tips were characterized using an SEM to measure the tip ID, OD and cone angle as shown in Figure 10. The taper lengths were measured using a ruler.

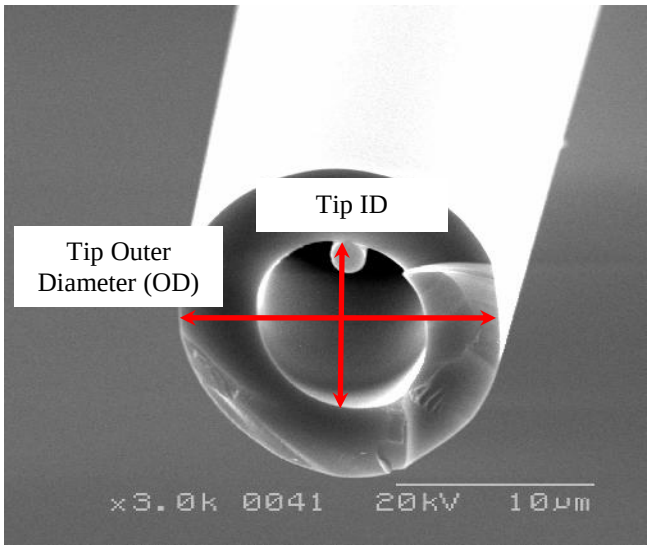

Figure 10. SEM image of tip of pulled micropipettes. (The smaller tube visible in the image is supplied by manufacturer to facilitate ease of aspiration for suction applications.)

4.3.3.2. Microneedle Fabrication using Surface Tension Forces

To improve on current fabrication approaches to fabricate tapered glass structures, a method using surface tension forces of hydrofluoric acid (a glass etchant) to chemically modify fused silica tubing was developed based on previously demonstrated research on optical fibers and capillary tubing.

A 6" section of 363 μm OD/10 μm ID capillary tubing was cut from the supplier's spool with a ceramic cleaving stone included with the capillary tubing. The section of tubing was then stripped of its polyimide coating by immersing it in concentrated H_2SO_4 heated to 130°C for 30 minutes. After stripping, the OD of the tubing was reduced to 323 μm.

The tubing was then rinsed under running water for 10 minutes and inserted into the tip of a stainless steel needle and bonded with epoxy glue to form a seal. The needle was then connected to a syringe and clamped so that the capillary tubing was positioned vertically. The plunger of the syringe was depressed until a droplet of water was visible at the tip of the free end of the capillary tubing. At that instant, a second burette clamp with vinyl coated jaws was used to hold the depressed plunger so that water could be dispensed until flow was initiated.

Deionized water was pumped through the inner bore of the capillary tubing for the duration of the etch. The pumping of water through the inner capillary bore prevented surface tension mediated influx of acid etchant.

The capillary tubing was then lowered into a solution of 90 mL 49% HF and 5 mL paraffin oil in a 200 mL polypropylene beaker until several millimeters of tubing were visible in the aqueous layer to ensure that the tubing was exposed to the etchants as shown in Figure 11. As long as the immersed end of the tubing was visible in the etchant, microstructures with sharp tips were generated. If the tubing was not visible in the etchant, an incomplete or unmodified tip would result.

The sample was retrieved after etching for 120 minutes. The microneedle was subsequently immersed in a saturated $Na_2(CO)_3$ solution for complete neutralization of the acid etchant to ensure safety during handling [102]. Complete removal of HF was sometimes performed by cleaning the sharpened tip with ethanol followed by immersion in deionized water for 24 hours [124]. The microneedle was then imaged and dimensioned using either an optical microscope or SEM.

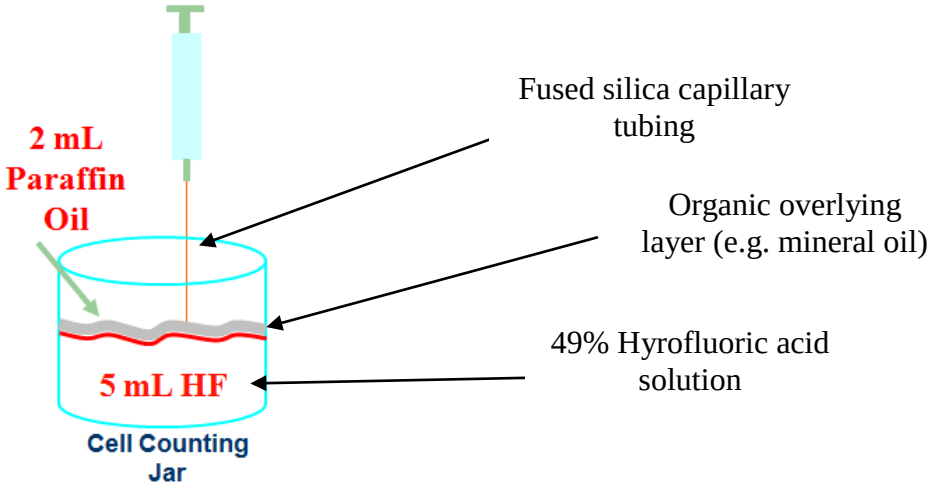

Figure 11. Experimental setup for etching capillary tubing in 49% HF

Smaller diameter tubing was also etched using the same process. 6" sections of 150 μm OD/10 μm ID tubing were stripped of the 12 μm polyimide coating using the hot, concentrated sulfuric acid process. The stripped 126 μm fused silica tubing was inserted into a needle and bonded using epoxy and etched similarly as the larger OD tubing. A shorter etch time of only 60 minutes was required due to the presence of less material to be consumed during the chemical reaction. Due to the smaller dimensions of the tubing, a weight had to be added to the tubing when suspending the tubing into the etchant. Typically a small piece of tape wrapped around the tubing was sufficient to prevent tubing drift in the etchant so that the capillary tubing was positioned vertically.

A low-cost method of fabricating arrays of microneedles was also developed to mimic the "batch processed" approaches typical of conventionally microfabricated microneedle arrays. However, only the smaller 150 μm capillary tubing could be batch processed due to its very low bending radius which enabled the flexibility required for array etching. This approach enabled large numbers of microneedles to be etched at a time for further processing and integration into the final device.

The process to make microneedle arrays started by designing a mask to make patterned arrays of microgrooves in PDMS. Two sets of microchannels were designed on a single 4" square dark field mask using AutoCAD. 150 μm

wide X 25 mm long microchannels at a pitch of 150 μm were sized to accommodate microneedles in the range of 126 – 150 μm OD, while 363 μm width X 25 mm long microchannels at a pitch of 363 μm were used for microneedles in the range of 323 μm – 363 μm. Both sets of sizes were included as the mold would also be later used to cast the substrates used for integrating the microneedles into the flexible elastomeric substrate.

Microchannels of both dimensions were grouped into sets of five. The sections were first used as a holder for array based etching for maintaining the capillary tunings in a vertical position at a fixed distance from each neighboring capillary during the array etch so that there was no interference in surface tension forces between each tubing. As such, the 363 μm width microgrooves were suitable to hold the 126 μm tubing sections at distances that kept each spatially isolated from the neighboring tubing so that a complete taper could be formed

To make the holder for array etching, the inverse micromolded elastomer was made by casting PDMS prepolymer onto the silicon/SU-8 molds. After curing, the patterned polymer was peeled from the SU-8 mold and cut to make 10 cm X 8 cm PDMS sections patterned with 3 sets of 5 X 363 μm microgrooves. A smaller unpatterned section of PDMS, which was poured and cured into an empty petri dish with no wafer, was placed on top of the microgrooved section sealing the channels.

The assembly was then ready for easy insertion and alignment of the tubing for the etch process. After all the tubing sections were threaded through the microchannels in the holder, the sections were fixed into place with 1:10 PDMS prepolymer rapid-cured on a 120°C hotplate.

The distal ends of the tubing sections were bundled and inserted into a 1/16" BARB Luer and coupled to a 5mL syringe and clamped upright as shown in Figure 12. After clamping the assembly upright, epoxy glue was applied to the junction of the tubings at the luer fitting orifice in order to fluidically couple and seal the tubings to the water reservoir in the syringe. To ensure a complete seal, the epoxy base and catalyst were combined and left to cure for exactly 4 minutes using a timer before application as the higher viscosity upon curing minimized flow of the viscous epoxy away from the gaps to ensure a leak-free seal every time. The assembly was left to fully cure for two hours before filling the syringe with water and proceeding with the etch process.

After the assembly was ready, the syringe was filled with water and clamped onto a ring stand. The plunger on the syringe was then depressed until droplets of water were visible at the array of capillary tips as shown in Figure 12. They syringe plunger was then clamped into position. The tubing was then lowered into the 49% HF, covered with a layer of paraffin oil, again until several millimeters of the tubings were visible in the aqueous layer to

ensure that an array of microneedles could be formed. Water was dispensed at constant pressure and the lengths of tubing were left to etch for 60 minutes.

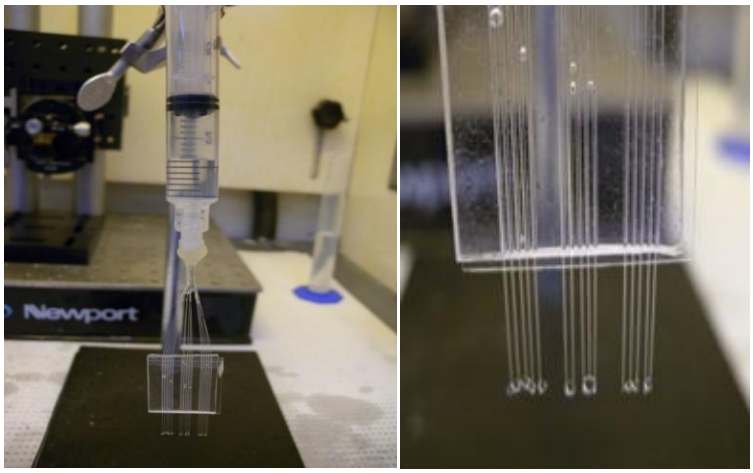

Figure 12. Pressurized flow of water through a 126 μm OD/10 μm ID capillary tubing array before immersion into HF etchant for the etch process to fabricate microneedle arrays

One further modification to the process was developed. As the array etch process often resulted in breakage of the capillary tubing and loss of product yield, a portion of the native polyimide coating was left on the capillary tubing. This increased the allowable bend radius of the tubing so that ordinary handling forces would not break the tubing. The polyimide was kept on the tubing to a point that extended beyond the length of the PDMS holder as shown in Figure 13 to ensure that the weak point at the coated/stripped interface was outside of the PDMS holder.

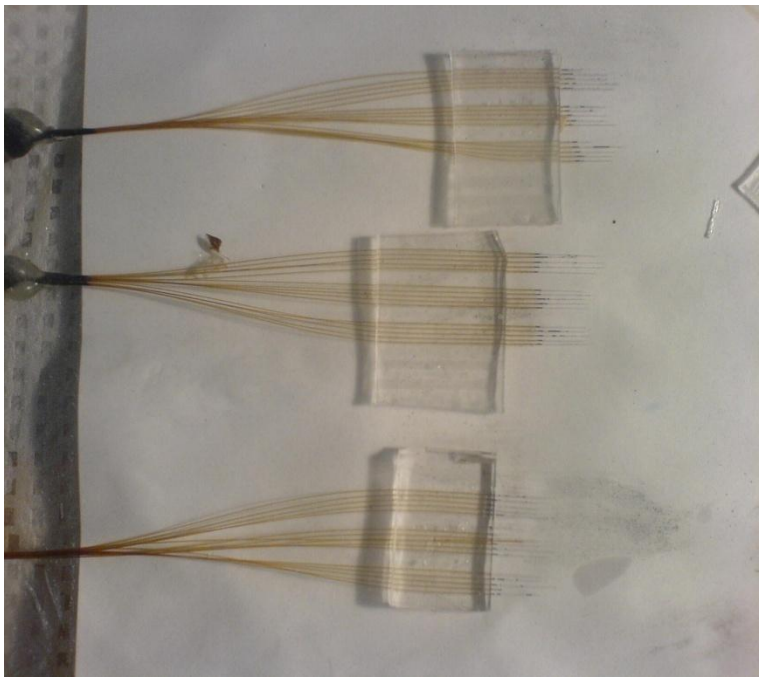

Figure 13. Post-etch image showing arrays of 15 X 126 μm OD/ 10 μm ID microneedles using the native polyimide coating for the unmodified ends to prevent breakage and fracture of the tubing during assembly, handling, etching and microneedle retrieval

4.3.4. Device Assembly

4.3.4.1. Assembly: Pipette Pulled Microneedles

Once each of the capillary tubes was pulled using the pipette puller into its two tapered counterparts, a diamond-tipped file was used to cleave the tips from the unmodified capillary tubing at approximately 0.5 cm from the tip. The isolated tip was then embedded into the PDMS microchannel using the circular positional markers. Figure 14 shows the process flow for embedding the microneedles into the micropatterned PDMS substrate. Sylgard 184 PDMS was prepared and cast over the master silicon mold which was placed in a standard petri dish. Step 2 shows the negative impression created in the

PDMS after curing over the positive relief structure patterned in SU8. A separate sample of PDMS was cured in a petri dish without any silicon master to form an unpatterned upper housing for the device and to seal the underlying microchannel as shown in Step 3. The unpatterned PDMS was temporarily placed on top of the micropatterned PDMS in order to denote position of the circular alignment markers on the 300 μm microchannel. After marking position, the unpatterned PDMS was removed and holes were made using 1.0 mm circular punches with a tissue biopsy tool as shown in Step 4. The unpatterned slab containing the new through holes and the patterned PDMS were both plasma oxidized and bonded taking care to align both halves to form an irreversible covalent bond between the sections shown in Step 6. A 100 g weight was placed on top of the assembly for 8 hours to ensure complete bonding. The 0.5 cm microneedle tips were then retrieved and inserted into the through holes of the upper section and into the circular alignment marks of the patterned PDMS. The entire assembly was then placed onto a hotplate at 120^{o}C and left for 20 minutes to ensure the PDMS was at temperature. The microneedles were then rolled in uncured PDMS and inserted into the through holes to rapid cure which ensured that the prepolymer would cure before flowing into the channel and forming blockages.

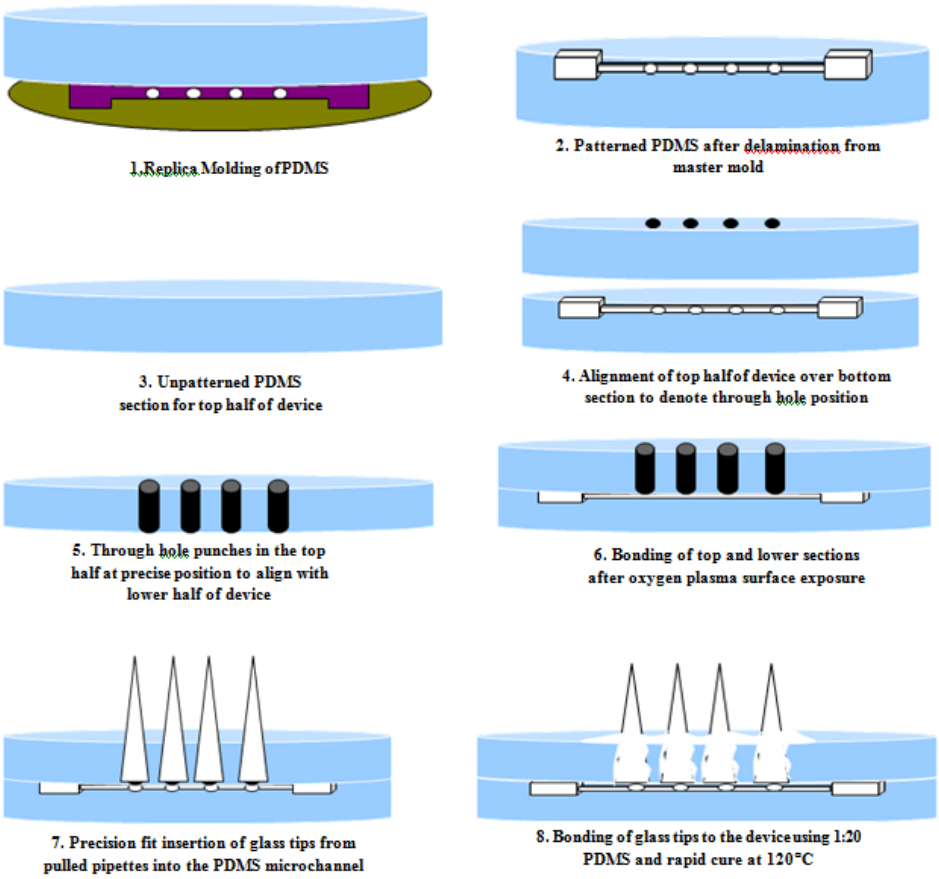

Figure 14. Process flow diagram for assembly of PDMS substrate to embed pipette pulled microneedles for the delivery device

4.3.4.2. Assembly: Microneedles Fabricated using Surface Tensions Forces

Once the HF-etched based fabrication methods had been developed and standardized to yield repeatable hollow microneedles, a method of embedding and integrating the microneedles into an underlying flexible substrate for a drug delivery application was developed. The objective was to pattern the flexible substrate in a manner that would align and position the microneedles with the precision and accuracy typically associated with conventional microneedle fabrication methods.

To achieve this, capillary tubing was manually rolled and positioned into the self guiding alignment scheme, discussed earlier for holding the tubings during array fabrication, provided by the patterned microgrooves obtained from photolithographically defined master wafers patterned in SU-8.

As the width of the underlying microchannel was of the same dimension as the outer diameter of the tubing, the unmodified end of the capillary tubing was positionally maintained via the self-guiding alignment scheme. This interference fit provided an ultra-precise alignment tool to ensure orthogonality between the microneedle and flexible PDMS substrate.

Once the unmodified section of the capillary tubing was securely fit into the microgroove, the chemically etched portion of the capillary tubing containing the sharpened tip was positioned to extend beyond the edge of its housing substrate as shown in Figure 15. The central microchannel within the set of five microchannels was typically chosen for placement of the single microneedle.

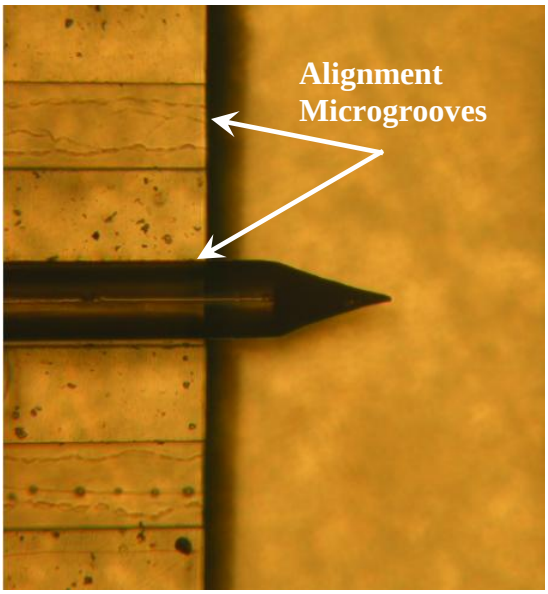

Figure 15. Image of a single 323 μm OD/ 10 μm ID microneedle in an alignment groove in PDMS

In order to set the length of the microneedle to a particular value based upon a particular tissue target within the eye, another mask was developed. This mask was used to only pattern positional markers in SU-8 on a silicon master (i.e. the mask was not used to cast PDMS - instead it was used as a positional tool to set microneedle lengths). After the microneedle was aligned into the central microchannel in PDMS, the microneedle/PDMS assembly was placed onto the silicon wafer with the SU-8 positional markers under the microscope. The leading straightedge of the PDMS section was positioned against the microledge shown in Figure 16 also included in the pattern.

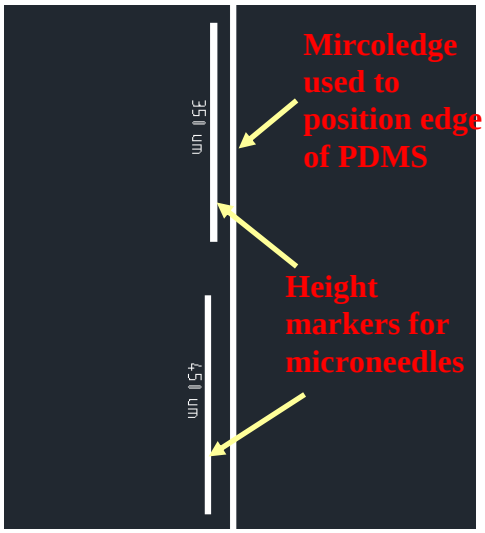

Figure 16. Mask used for setting microneedle length based on tissue target for solute delivery.

Prior to permanent fixture of the assembly, the microneedle length was set to a value within a range of 0.050 – 1.1 mm at 50 μm increments using a microscope based on the particular intraocular tissue to be targeted during the infusion experiment. Due to friction between the interference fit of the tubing and microchannel, the tubing was temporarily secured. The assembly was then transferred to preheated hot plate and permanently fixed into place using a rapid thermal cure of an optimized combination of PDMS prepolymer base and curing agent to maximize the strength of the tubing/PDMS interfacial bond.

4.3.4.3. Assembly: Microneedles Fabricated using Surface Tension and Electrokinetic Pumping

To integrate and combine the microneedle fabrication process with the assembly process, a method was developed to use electroosmotic forces to pump water during etching. For this procedure, 3 cm-length segments of 150 μm OD/10 μm ID fused silica capillary tubing were carefully cut using a cleaving stone. Polyimide coating was removed using hot concentrated H_2SO_4. The cleaned tubing sections were then placed into a beaker of methylene blue in order to fill the tubes via capillary action. Tubing sections were left in the beaker for 20 minutes to fill. Each segment was then tested for electrical conductivity to select for subsequent embedding into the micromolded PDMS channels as shown in Figure 17.

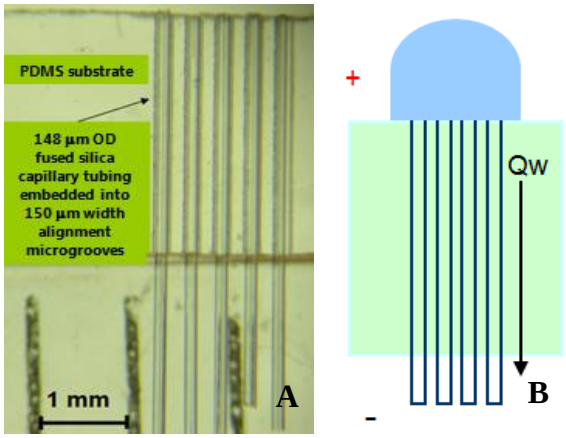

Figure 17. Capillary tubings were preloaded with methylene blue dye for visualization of filling, tested for conductivity and then embedded into the microchannels (A) for subsequent taper definition using HF etchant. A single droplet of water was then placed on the top-side of the tubing array (B) to provide a reservoir from which to pump water through the capillary once the assembly was placed in an electric field.

In order to select only those tubing samples that were completely filled, as this would indicate an electrically conductive pathway, the tubing section was placed between two syringes filled with water. Upon application of a voltage across the system, if a current was registered, the tubing was assumed to be conductive and was selected for placement into the device.

Approximately 50% of the tubing sections tested were actually conductive. After five conductive tubing sections were selected and inserted into the micropatterned PDMS, a single droplet of tap water was placed on the top of the microchannels in the PDMS section - covering the topsides of the pre-filled capillary tubings as shown in Figure 17 (B). An electrode was then epoxied onto the substrate as shown in Figure 18, while the opposite end of the tubing sections to be etched were immersed into the HF/oil solution. The other electrode was placed in the HF to form the required the electric field. A 1.1 kV potential was applied for 1 hour with a corresponding current

of 0.0220 μA.

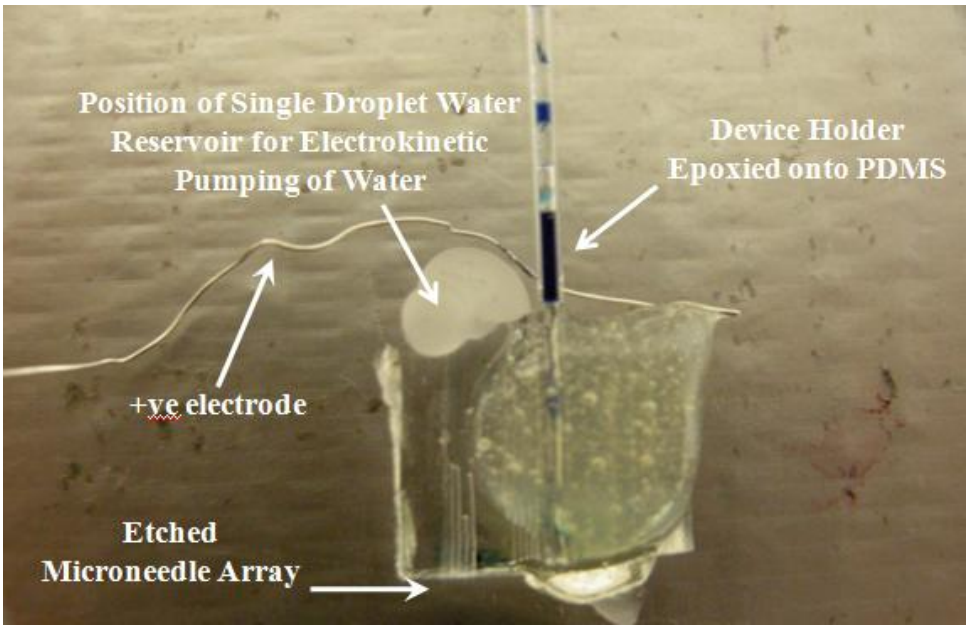

Figure 18. Experimental apparatus for parallel fabrication of microneedle arrays using a micromolded PDMS capillary tubing alignment positioner, a single droplet water reservoir and an electric field*

*Figure 18 shows hardened paraffin wax in the area which is normally occupied by the water droplet before etching. The image was taken post-etch and the wax was applied in order to fix the capillary tubing sections in place for imaging after alignment of the microneedles. As shown in Figure 17, tubing sections extended beyond the edge of the PDMS. The edge of the PDMS rests in paraffin oil during the etch process to avoid etching from the aqueous HF layer. As such, after microneedles are etched, the tubing sections can be pushed out of the other end as they are not permanently fixed.

4.3.5. Optical and SEM Microscopy

Microneedles and devices were imaged and dimensioned using an optical microscope. Samples were first gold-sputtered in a vacuum in an argon gas chamber at a rate of 3 Angstroms/s at 18 mA. Samples were sputtered for 30 seconds. Samples were then imaged at 10 kV with an SEM microscope [JSM-7000F, JEOL Inc., Peabody, MA] and [S-2150 SEM, Hitachi, Norcross, GA].

4.3.6. Mechanical Testing

4.3.6.1. Pipette Pulled Microneedles

An Instron 4411 Universal Testing System (Instron Corp., Norwood MA) fitted with a 50 N load cell was used to measure the strength of the bond between the glass microneedle and the PDMS microchannel. A crosshead rate of 10 mm/min was used for the tensile tests.

4.3.6.2. Surface Tension Fabricated Microneedles

In order to characterize the bond strength of different adhesives between embedded microneedles and their surrounding PDMS matrix, forces required for failure in both shear and in tension were measured with respect to the different bonding adhesives. A commercial tensile test machine (eXpert 5601, ADMET, Norwood, MA, USA) with a 50 lbf load cell (INTERFACE SM S-Type load cell, ADMET, Norwood, MA), was connected to a computer. Samples consisting of 10 cm long sections of either 323 μm glass or 363 μm

polyimide-coated tubing were embedded 15 mm into the PDMS section using different bonding adhesives as shown in Figure 19.

The PDMS section containing the embedded tubing was fixed to a metal plate. The metal plate was then clamped and attached to the load cell as shown in the figure. The tubing was clamped using a standard vice clamp taking care not to crush the tubing when clamping. Care was taken not to include the PDMS/tubing region in/near the clamp.

The samples were first loaded in tension and pulled at a crosshead displacement rate of 50 mm/min to failure. Load–displacement data was acquired at a sampling frequency of 32 Hz and downloaded to a computer (Wincom PLUS Serial Communications, ADMET, Norwood, MA). Microsoft Excel was used to obtain the failure stress characteristic of each bond tested based on the interfacial area between the tubing and the PDMS microchannel and the failure force.

A similar experiment was used to test the tubing under shear forces. The mode of the test machine was set to compression. The PDMS/tubing samples were clamped laterally so that the tubing was orthogonal to the vice. A probe was lowered at a speed of 50 mm/min until the tubing disengaged from the PDMS. The force was recorded and used to characterize the strengths of different adhesives.

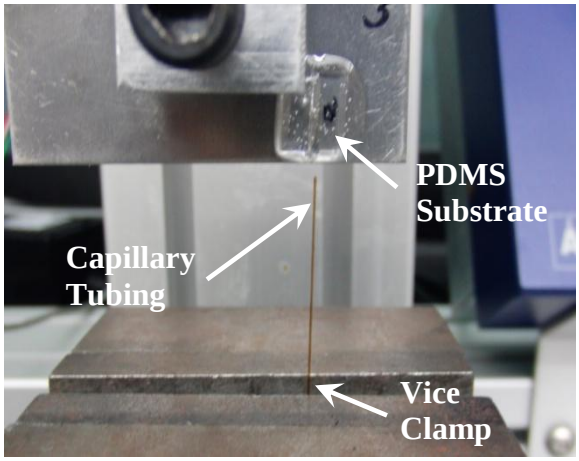

Figure 19. Tensile samples showing 10 cm long capillary tubing samples being pulled in tension from the PDMS substrates to which they are bonded to in order to determine the failure force of the interfacial bond

For tensile loading, four different bonding adhesives were studied: Sylgard 184 PDMS at base:curing agent ratios of 10:1, 3:1 and 30:1 and 10:1 with fumed silica viscosity enhancer. Upon mixing, the three PDMS mixtures at various ratios possess a low viscosity and flow rather rapidly to fill any void down to 100 nm (thus its prevalent utility in soft lithography).

As an alternative, PDMS can be thickened to a thixotropic substance by supplementing the PDMS with fumed silica [125]. For a 10 mL volume of PDMS base and curing agent mixture, approximately 0.85 g of fumed silica (Aerosil R Series Hydrophobic Fumed Silica, Germany) was added. At this viscosity, PDMS was unable to flow both due to gravity or viscous forces and was useful for situations whereby uncured PDMS flowed rapidly away from gaps. The force at which the bond failed was recorded for each of the tensile

tests. The corresponding stress at which failure occurred was calculated based on the tubing surface area.

As mentioned, the interfacial bond strength was also subjected to shear loading to determine the forces required for failure under expected shear stresses that the device would encounter during insertion into the eye. Figure 20 shows a schematic for the test using the same Admet system in compression mode to test failure under shear. The force at which the bond failed was recorded for each of the tests. The corresponding stress at which failure occurred was calculated based on the tubing surface area.

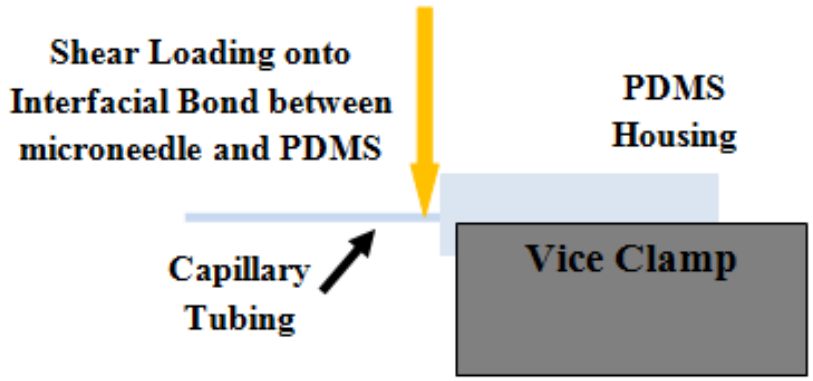

Figure 20. Schematic of specimen holder to measure bond failure force under shear loading

4.4.Materials/Methods for Drug Delivery Experimental Apparatus

4.4.1. Model Compounds

Five fluorescent compounds, either FITC-conjugated or native, were used in this thesis to study drug delivery from the fabricated devices: Rose Bengal (MW 1014 FU), 6-aminoquinolone (MW 144 FU), 40 kDa FITC-Dextran,

Rhodamine and Bovine Serum Albumin (FITC-BSA). All compounds were procured from Sigma Aldrich Corp., St. Louis, MO.

4.4.2. Trypan Blue Staining

Trypan Blue (Sigma Aldrich, St. Louis MO) staining was used to confirm insertion and penetration of the microneedles into the scleral tissue. The sclera was isolated from a whole globe, cut and washed in PBS. The section was laid flat on a petri dish filled with ice. An embedded 323 μm microneedle was used to penetrate the scleral section. After penetration, 50 μL of Trypan Blue was dispensed onto the injection site. After 30 seconds, excess Trypan Blue was rinsed from the tissue and the sampled visualized with microscopy for defects.

4.4.3. In-vitro Release from Microneedles

Devices were loaded with either Rose Bengal or 6-aminoquinolone to measure the release characteristics of the device in PBS. A syringe filled with a stock concentration of either dye (0.0125 mg/mL Rose Bengal; 0.00005 mg/mL 6-aminoquinolone) was placed into the PDMS microchannel and coupled to a syringe pump followed by insertion of the microneedles through a section of UV-cured collagen. The syringe pump was set to deliver a constant rate of 0.05 mL/min through the device into a reservoir for subsequent measurement of total accumulated dye. Total release time was 20 minutes.

All fluorescence was read using a Perkin–Elmer Victor 3 fluorometer. Readings for Rose Bengal were taken at two excitation wavelengths $\lambda_{ex,}$ 525 nm and λ_{em} 590nm. (The λ_{ex} 525 nm was unavailable so readings were taken with the available filters at λ_{ex} 485nm and λ_{ex} 544 nm and linearly interpolated to get the correct reading). Readings for 6-aminoquinolone were taken at λ_{ex} 355 nm and λ_{em} 535 nm. Concentrations in the samples were calculated using a regression on the linear range of the standard curve and are shown in Appendix 11.3. Adjustments during data reduction were made to account for background fluorescence detection in buffer.

Samples of release medium were read at two-minute intervals with the fluorometer over a 20 minute sampling period using a fluorescence plate reader with the appropriate filters.

4.4.4. Animal model: Porcine Eye

Whole porcine globes were obtained from Willie's Custom Meats (Troy, ON). Eyes were enucleated from adult pigs (50 kg average weight) within one hour of slaughter and then placed on ice for no more than an additional 30 minutes before the experiments. Excessive adnexal tissue and conjunctiva were trimmed from the eyes to reveal a globe with only an episcleral surface. Whole globes were then rinsed in phosphate buffered saline (PBS) pH 7.4 containing 0.02% NaN_3 (bacteriostatic) and kept in moist chamber conditions at 4° C for no more than 2 days for all subsequent experiments. Phosphate buffered solution

was prepared as follows: 1.32 g Na_2HPO_4, 0.345 g NaH_2PO_4, 8.5 g NaCl to a final volume of 1 L. The pH was adjusted to 7.4.

Porcine eyes were first characterized to determine scleral thickness around the circumference of the globe. Three individual pig eyes obtained from adult pigs were cut into four sections, or quadrants, as shown in Figure 21. Eyes were first cut circumferentially around the lower hemisphere using the optic nerve as a reference as shown by the red line. Each of the two halves were then cut into two equivalent segments. The cornea was completely removed before measurements were recorded. Each of the four quadrants was then cut into five equal size segments. Using a Vernier caliper with a digital readout, scleral thickness readings were taken ten times and averaged for each of the cut segments – twenty segments in total per eye.

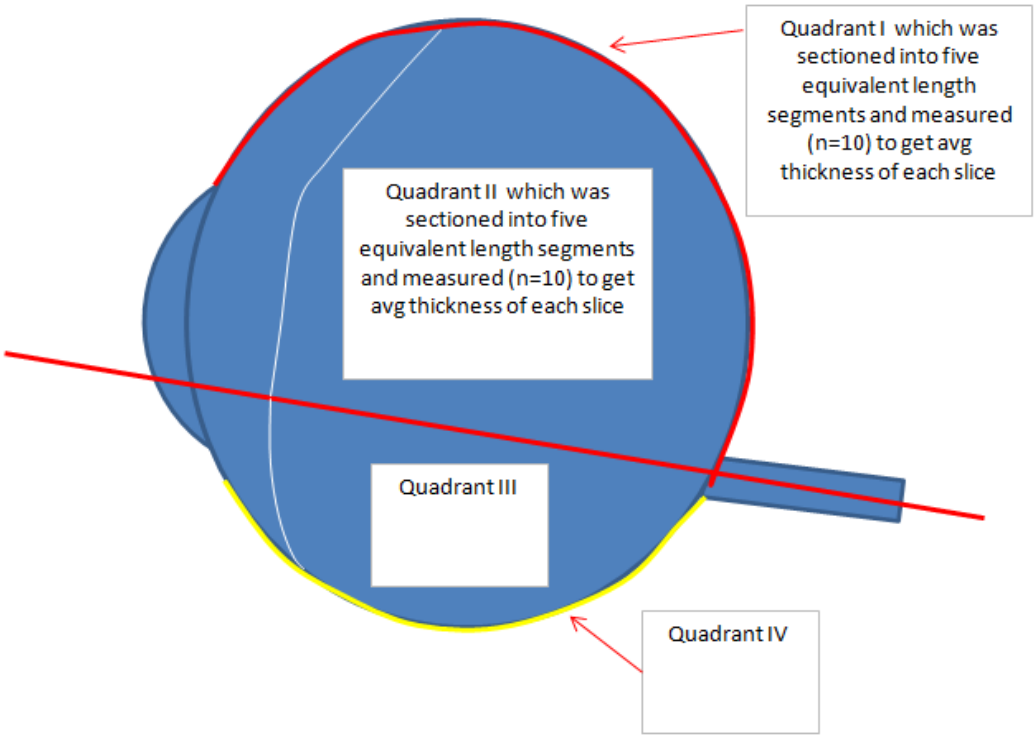

Figure 21. Sections from porcine eyes used to characterize average scleral thickness

4.4.5. Ex-vivo Drug Delivery Setup in Porcine Eyes

To demonstrate delivery in ex-vivo eyes, devices were coupled to a reservoir of the model drug being studied.

To construct the delivery setup after embedding of the microneedles, the PDMS section was first modified by cutting two angled edges on either side of the microneedle. This allowed both for more visual control of insertion while also allowing for less device interference with the curved surface of the globe that straight-edged PDMS devices were observed to encounter.

The unmodified free end of the tubing extending from the PDMS backside was then threaded through a 30 G stainless steel needle and epoxy glue was used to bond the needle to the tubing. In order to minimize the risk of tubing fracture, the length of tubing on the unmodified free end of the microneedles extending beyond the PDMS substrate was kept long, approximately 30 cm, to provide increased pliability and reduced chances of fracture for the tubing.

Retention of the polyimide coating on 95% of the length of the tubing instead of the typical full-length H_2SO_4 treatment for polyimide removal also prevented tubing breakage and associated loss of fluidic connection. This step was essential in conferring considerable flexibility to the glass tubing to avoid fracture and breakage during ordinary setup, handling and insertion.

Once the epoxy between the tubing and the needle was fully cured, the device was attached to a syringe filled with 0.1% trypan blue solution. Pressure was applied on the syringe to test for leaks in the system.

The whole globe was first pumped with water to approximately 15 psia as measured using a digital pressure gauge using a needle inserted into the optic nerve in order to recover the slight loss of scleral matrix rigidity of post-mortem eyes (Appendix 13.2 contains pressure calibration data for the pressure transducer). The pressure was maintained using a 3-way valve during the course of the infusions to prevent backflow and loss of pressure during infusion. The globe was then positioned in place to prevent rolling or displacement.

A simple manual method of insertion of the fluidically coupled device was used as shown in Figure 22. The microneedle was manually inserted into the sclera at a position approximately 10 mm posterior to the corneoscleral limbus (unless otherwise indicated). The microneedle remained embedded; an additional support was introduced to hold the reservoir tubing upright towards the syringe pump.

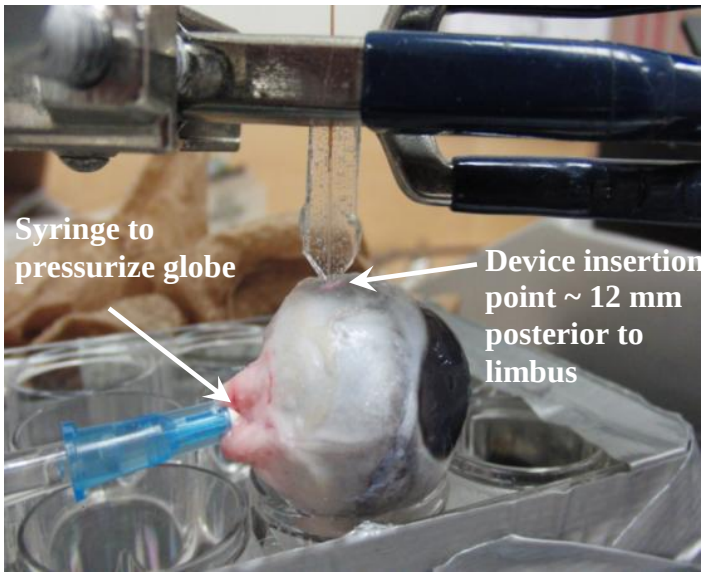

Figure 22**.** Microneedle device positioning into whole porcine globes followed by clamping of tubing for support for ex-vivo release studies

A flow rate of 1 mL/min of Rhodamine B from the syringe pump was started until flow from the microneedle tip was visible. Flow was then halted to allow the system pressure to equilibrate by removal of emergent dye droplets from the tip which was wicked with a Kimwipe until flow ceased. Once the system was at equilibrium, the pump was set to a delivery rate of 100–500

nL/min. Care was taken to avoid any dye accumulation on the episcleral surface upon microneedle insertion.

Several moistened paper towels were placed over the eye to maintain hydration of the eye during the experiment. Paper towels were replaced every 20 minutes to ensure a moist environment was maintained during the infusion.

After the infusion, the device was removed and the globe characterized for delivery.

4.4.6. Histology and Tissue Fixation

After the infusion experiment, whole globes were dissected with a circular cut approximately 1-mm posterior to the corneoscleral limbus to visualize both microneedle insertion and infusion into the various intraocular tissues. After removal of the cornea, the inner aqueous and vitreous humour and body were removed and inspected for dye accumulation. A cut was then first performed on the short axis of the globe towards the optic nerve insertion point while a second cut was on the long axis to lay the sample flat. The retina was gently removed with a cotton swab and inspected for staining. Sections containing sclera and choroid adjacent to the injection site were first optically imaged to assess delivery of compound to the scleral floor or the choroidal layers and then embedded in OCT (Optimal Cutting Temperature) (Somagen Diagnostics, Edmonton, AB) and flash frozen in isopentane previously cooled in a bath of

liquid nitrogen to prevent freezing artifacts. Samples were left at -80°C until ready for sectioning using a cryostat microtome.

Each sample was then sectioned into 50 μm thick sections using a Leica CM3050S cryostat microtome, mounted onto microscope slides and air-dried for analysis using a confocal microscope (Carl Zeiss LSM 510, Thornwood, NY) to show precise localization of the injected model compound. LSM 510 Image Browsing Software was later used to retrieve, view, edit and embed images.

A separate procedure was required to visualize the posterior layers of the porcine eye that included the retinal and choroidal layers as once globes are dissected it is nearly impossible to preserve the spatial arrangement of the neural retina and choroid due to their delicate compositions.

For visualizing the posterior segment, a whole porcine globe was placed in a flask of liquid N_2. While liquid-N_2 cooled isopentane was adequate to freeze smaller sections of scleral tissue containing the microneedle insertion site, this approach was not feasible for an entire globe (due to substantially higher isopentane volumes required for an entire globe). As such, to properly visualize the intact spatial arrangement of the posterior, full immersion of the whole globe directly in liquid N_2 was attempted. Though the globe immediately cracked/ruptured upon temperature depression, the entire globe was frozen and immediately embedded in melted paraffin wax and returned to the liquid N_2 flask for freezing. After embedding, a standing powered mechanical band saw was used to cut the embedded globe.

Sections from the globe were difficult to cut as the globe fractured into multiple pieces upon band saw blade contact. However, for simple tissue layer visualization purposes a section containing the posterior tissue arrangement was retrieved and is shown in Figure 23. The section was placed in 10% formalin for 48 hours and then placed in a plastic tissue cassette (VWR, Radnor, PA), labeled and placed back into the formalin solution for 1 hour. The sample was then transferred to a 50% ethanol solution for 30 minutes and then transferred to 70% ethanol for storage and transport to the histology lab for processing. Sections were 3-4 μm thick and were stained using haematoxylin and eosin (H&E) for visualization of the posterior microanatomy only, as shown in Figure 24.

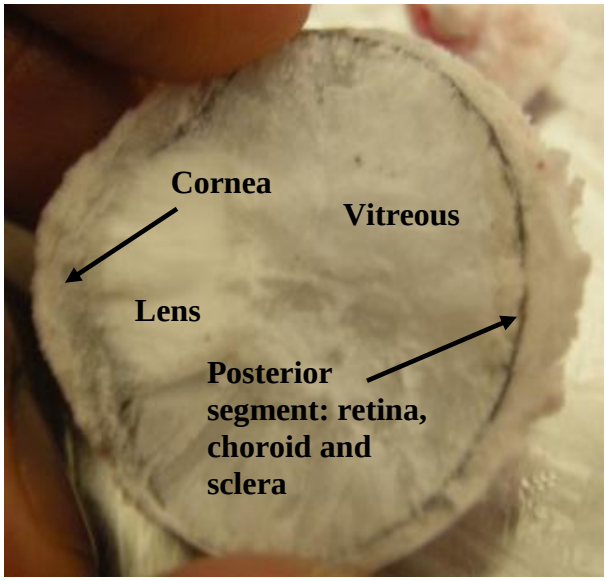

Figure 23. Porcine whole globe frozen in liquid N_2 and sectioned using a band saw. Spatial arrangement of the posterior section is intact and ready for chemical fixation. (The lens and vitreous are visible due to their high water content).

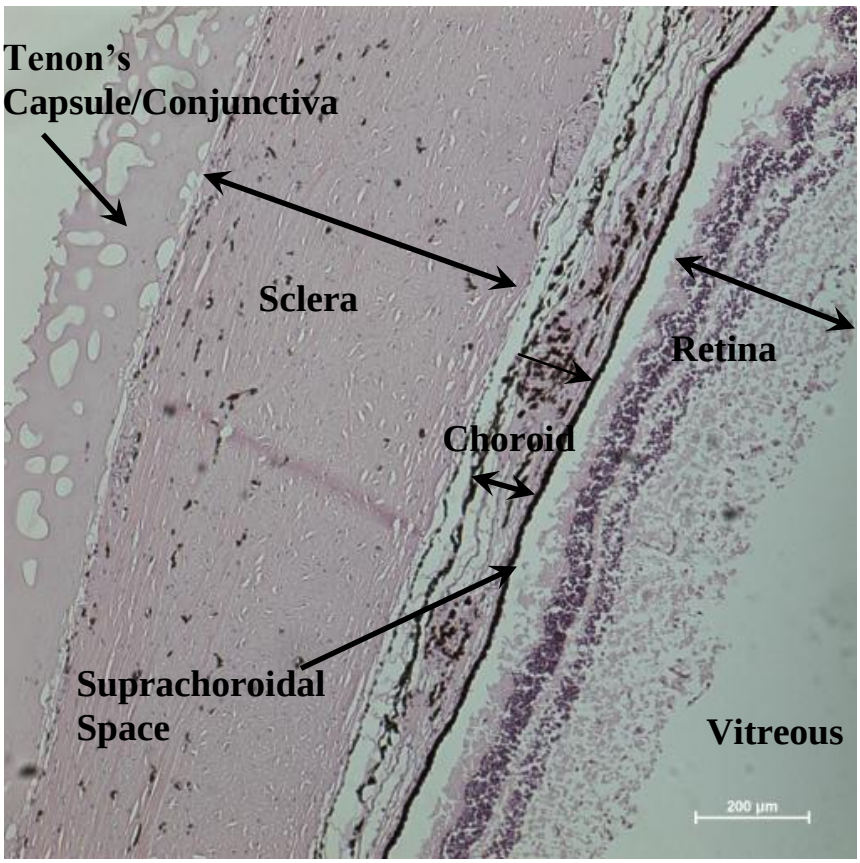

Figure 24. Tissue layers of the posterior porcine eye - as visualized from histological analysis of frozen, sectioned and H&E stained samples

4.4.7. Image Analysis

The intensity of rhodamine in the 50 μm tissue sections was measured with ImageJ, an open-source Java-based software, using a modified method of quantifying cell fluorescence intensity [126, 127]. To determine the level of fluorescence for a particular region of interest (ROI) in each of the tissue sections, an area was defined using the software's selection tools around the region containing the defect caused by the microneedle. An equivalent area was selected between tissue sections to compare change in intensity with tissue depth. Area,

integrated density and mean gray values for both the total image and the background were determined. To calculate the actual fluorescence intensity of the region, the mean fluorescence of the background readings was multiplied by the area of the ROI and then subtracted from the integrated density of the ROI to attain the corrected total fluorescence of the tissue section.

4.5.In-vitro Diffusion Experiments

4.5.1. Tracer Molecule

The change in apparent permeability of untreated and microneedle-pierced scleral tissue was determined using 40 kDa FITC-Dextran (Sigma Aldrich Corp., St. Louis, MO) as the tracking solute.

4.5.2. In-vitro Model: Bovine Eye

For delivery studies using whole globe models, eyeballs were used within 48 hours of the kill to ensure minimal degradation of vitreous humour which would contribute to loss of scleral tension and integrity. Whole bovine globes were obtained from a local slaughterhouse (Willie's Custom Meats 1346 4th Concession Rd W, Troy ON L0R 2B0).

Eyes were enucleated from steers shortly after death, obtained within one hour of the slaughter and then placed on ice for an additional 30 minutes until dissection in the lab. After removal of the adnexal tissue, conjunctiva, cornea, anterior segment and vitreous body, scleral sections from the upper hemisphere

were cut and stored at 4°C in phosphate buffered saline for no more than 72 hours. Care was taken not to gouge the episcleral surface during trimming and removal of the conjunctival tissues.

4.5.3. Diffusion Chamber

A two chamber side by side diffusion cell (Permegear, Bethlehem, PA) was used to measure transscleral permeability of the solute using either unmodified, intact bovine sclera or scleral sections that were pierced through with a single 323 μm OD/10 μm tip ID. Scleral tissue was excised from the superior temporal region of the bovine eye and placed between the two chambers of the permeation cell. A solution containing 1.67 mg/mL of the solute was loaded into the donor chamber with the episcleral side facing the donor and uveal side facing the receptor chamber which was filled with phosphate buffered saline (PBS pH=7.4) as shown in Figure 25. This concentration was chosen as for convenience in measurement of 25 mg FITC-Dextran crystals followed by dissolution in 15 mL PBS using a standard 15 mL polypropylene centrifuge tube (VWR, Radnor, PA). Both sides were continuously stirred. The cross sectional area of the used in the calculations was based on a cross sectional area between the chambers of 10 mm^2. The chambers were initially filled with PBS on both sides and run for 20 minutes to equilibrate the tissue sample and ensure that there were no leaks. The buffer was then removed from the donor chamber facing the episcleral side and loaded with the solution

containing the fluorescent marker. 200 μL aliquots were taken every hour over the course of a study.

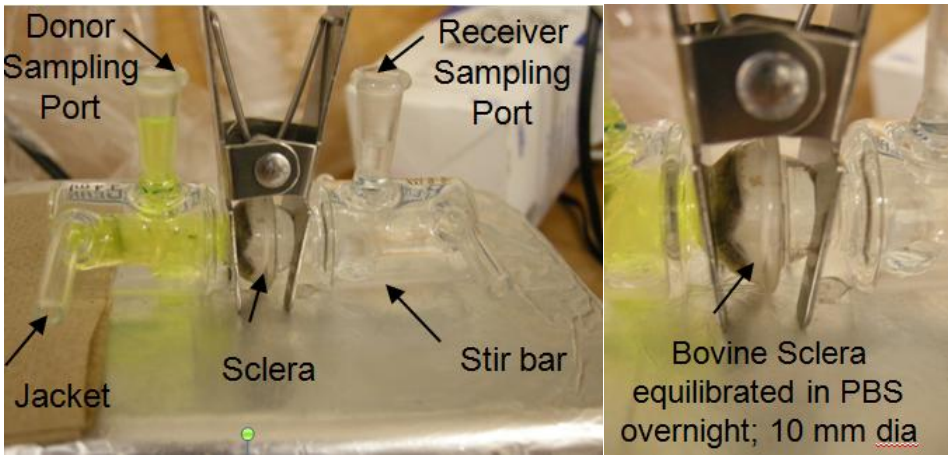

Figure 25. Two-chamber permeability experiment to determine diffusion of 40 kDa FITC-Dextran through a section of bovine scleral membrane.

4.5.4. Scleral Permeability

The total accumulated mass was calculated (both chamber volumes were 3.7 mL) and from the flux data, a steady-state permeability (K_{trans}), a solute-specific parameter through the sclera, was then calculated using Equation 4 [128]:

$$K_{\text{trans}} = \frac{R_{\text{total}}}{(t)(A)} \times \frac{1}{D} \qquad \text{Equation 4}$$

where R_{total} is the represents the total number of moles of dextran that diffused through the sclera over a time *t*, in seconds, *A* is the exposed area of the tissue between the chambers and *D* is the concentration of the compound in the donor chamber. The coefficient gives the velocity of the molecule through the tissue

and has units of cm/s which represents its diffusion through the buffer and the sclera as a whole.

For FITC-Dextran, the excitation wavelength was 418 nm and the emission wavelength 520 nm. Samples were read and then returned to the receptor chamber. Standard curves of fluorescence versus concentration, shown in Appendix 13.3, were obtained by serial dilution of the FITC-dextran in PBS. Concentrations in the samples were calculated using a regression on the linear range of the standard curve.

Chapter 5 In-vitro Delivery Using Embedded Microneedles

5.1. Prototype Device and Pipette Pulled Microneedle Measurement

To demonstrate that microneedles could indeed effectively penetrate the tough, fibrous outer tunic of the sclera and deliver compounds to the eye, a prototype using pulled microneedles was first tested.

A stereoscopic image showing the device fabricated with the pulled microneedles is shown in Figure 26 (A). Dye was injected into the 300 μm device microchannel using a syringe attached to a stainless steel 30 G needle which was inserted into one of the 10mm X 20 mm reservoirs. The side angle view shown in Figure 26 (B) shows the identical device with the microneedles fully filled with the dye without any leakages. A close angle view of the four microneedles, spaced approximately 5 mm apart, dispensing the test dye through the open tips is shown in Figure 26 (C).

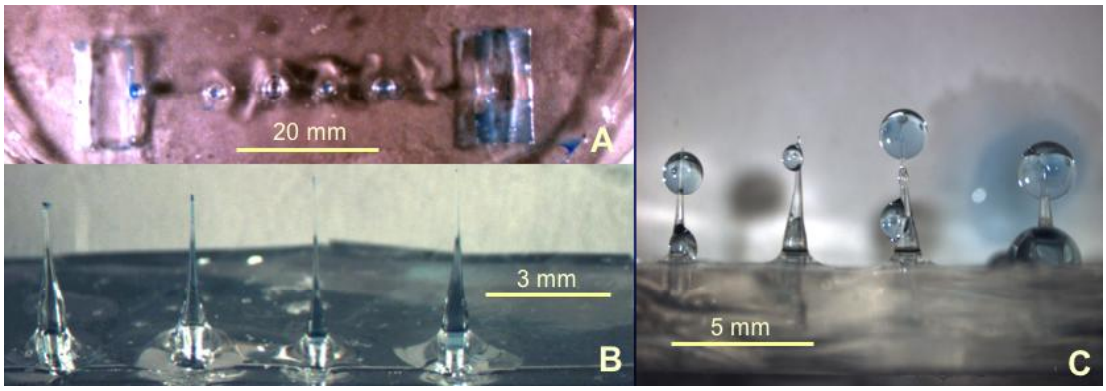

Figure 26. Stereoscopic images showing delivery of dye in pulled microneedles integrated into the assembled micropatterned PDMS device. Microchannels were 300 μm wide and 5.0 cm long flanked by terminating 1.0 x 2.0 cm^2 rectangular reservoirs on either end. Aerial view (A) of the device showing pulled microneedle tips aligned with the underlying 300 μm microchannel; side angle view (B) filled microneedles without any leakage; solution emerging (C) from the 2-um tips.

Figure 27 shows a representative SEM image of a pulled micropipette and the corresponding long taper and tip. Although the actual pulled structure possessed long tapers with very small tip dimensions, close-scale imaging of the tips showed that the tips did not actually themselves terminate into a sharp point and that tip quality was poor and inconsistent as shown in the figure. This observation was consistent in each of the tips imaged with SEM. However, as the taper occurred over several millimeters, the overall structure was hypothesized to still be able to penetrate biological tissue.

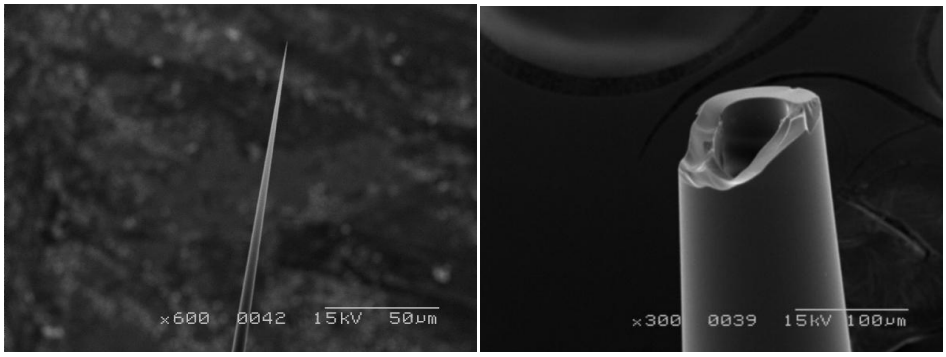

Figure 27. Characteristic taper and tip appearance on micropipettes pulled from capillaries. Although pulled micropipette tips appeared extremely sharp, images analyzed under increased magnification showed that the actual tip did not terminate into a defined sharpened tip.

The pulled micropipette tips were imaged using SEM. The tip ID and tip OD were measured from the images as shown in Figure 28. The cone angle, an indicator of tip sharpness, was extremely small and therefore impossible to measure at the required precision. Cone angle measurements give an indication of the sharpness of the tip with larger cone angles correlating with decreasing tip sharpness. As the actual angles could not be measured with any accuracy, it was

noted that the observed angles were actually much smaller than one degree. Although the taper lengths were on the order of 1 cm long, it was expected that only a segment of the actual taper would be retrieved and used for the device as fracture and buckling would most certainly result under the forces of insertion and penetration into test tissues.

The process generated micropipettes with a mean tip ID of 3.07 μm ± 2.04 μm, tip OD of 5.89 μm ± 3.07 μm and taper length of 9.01 mm ± 0.25 mm. As discussed, cone angles were not measured but appeared to be within a fraction of one degree.

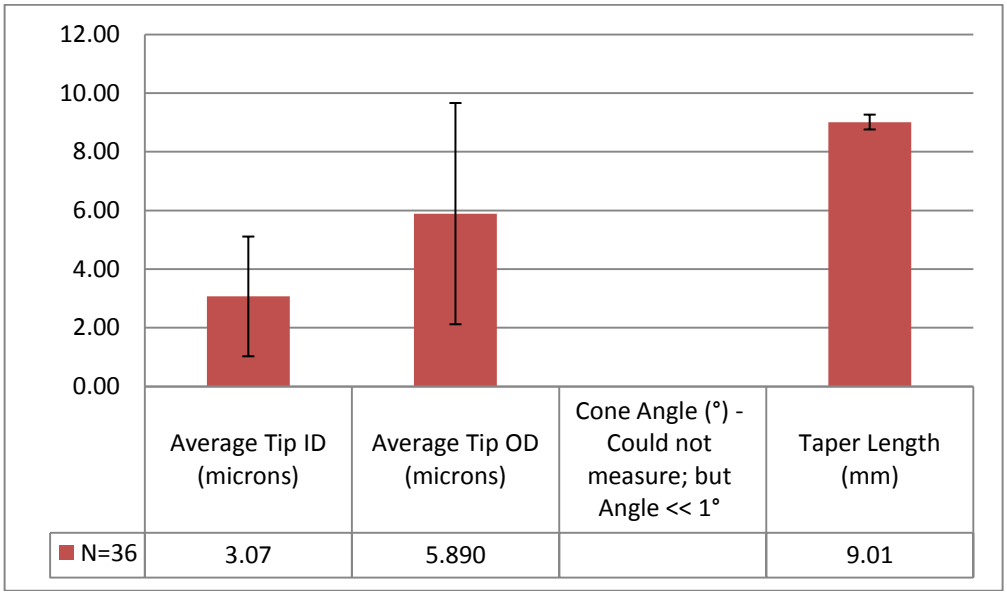

Figure 28. Mean tip ID, tip OD, cone angle and taper length for pulled micropipette tips. Tips were pulled from 1.00 mm OD/0.50 mm ID standard wall borosilicate capillaries using the P-97 Puller at #33 program conditions.

5.2.Penetration of Collagen/Bovine Sclera and Release in PBS

The microneedles penetrated UV-crosslinked collagen and bovine sclera without breaking or delaminating form the PDMS matrix as shown in Figure 29. The average strength of the bond between the microneedles and PDMS was 4.8 MPa based on six trials of the tensile test.

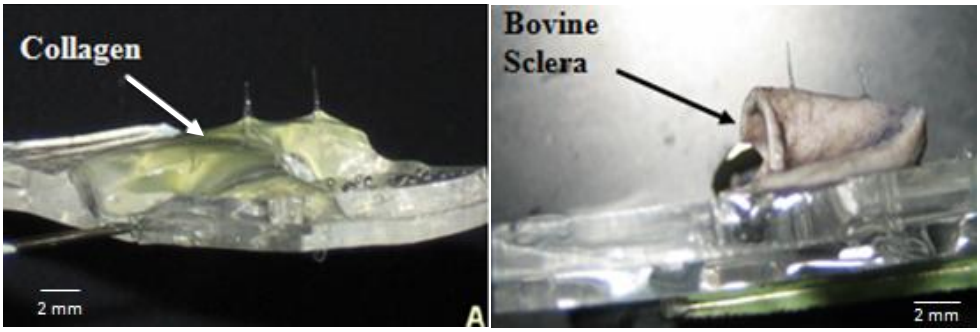

Figure 29. Microneedle penetration of UV-crosslinked collagen (A) and excised bovine sclera (B). Insertion and penetration was achieved without microneedle fracture.

To demonstrate delivery, the devices were loaded with either Rose Bengal or 6-aminoquinolone. A needle coupled to a syringe containing each dye was placed into the PDMS microchannel. The syringe was placed into a syringe pump to deliver a constant rate of 50 μL/min through the device into PBS. Figure 30 shows streaklines of continuous flow of Rose Bengal from the microneedles.

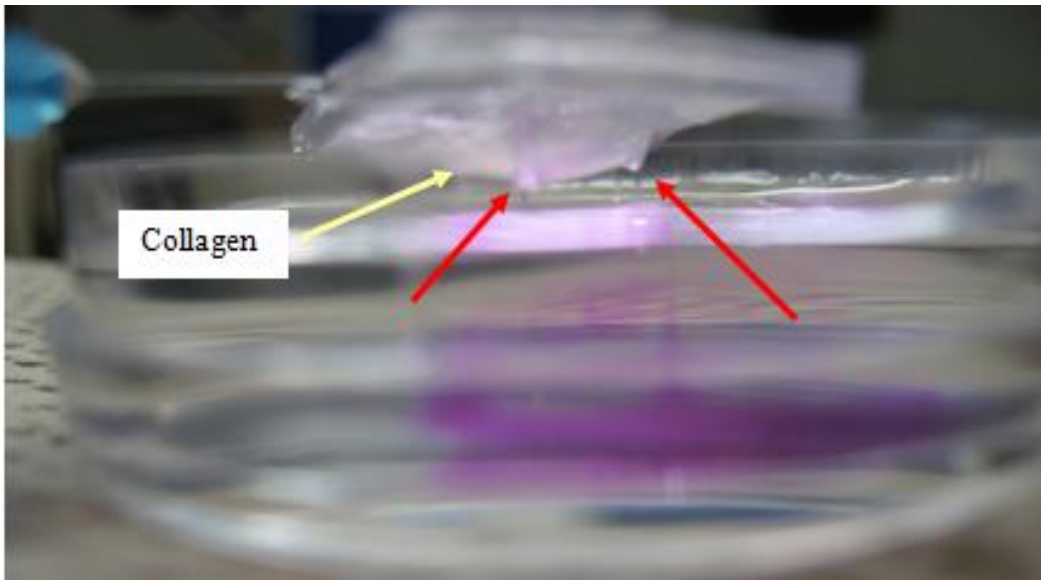

Figure 30. Continuous delivery of Rose Bengal solution at a rate of 50 μL/min. Red arrows indicate the fixed location of the microneedles in the reservoir from which visible streaklines appear.

The device delivered both compounds at the same rate independent of the compound molecular weight and chemical properties, Figure 31. The total measured accumulated mass of both compounds delivered was equivalent to the total mass delivered - evidence of continuous and clog-free delivery over three independent experiments using the same device.

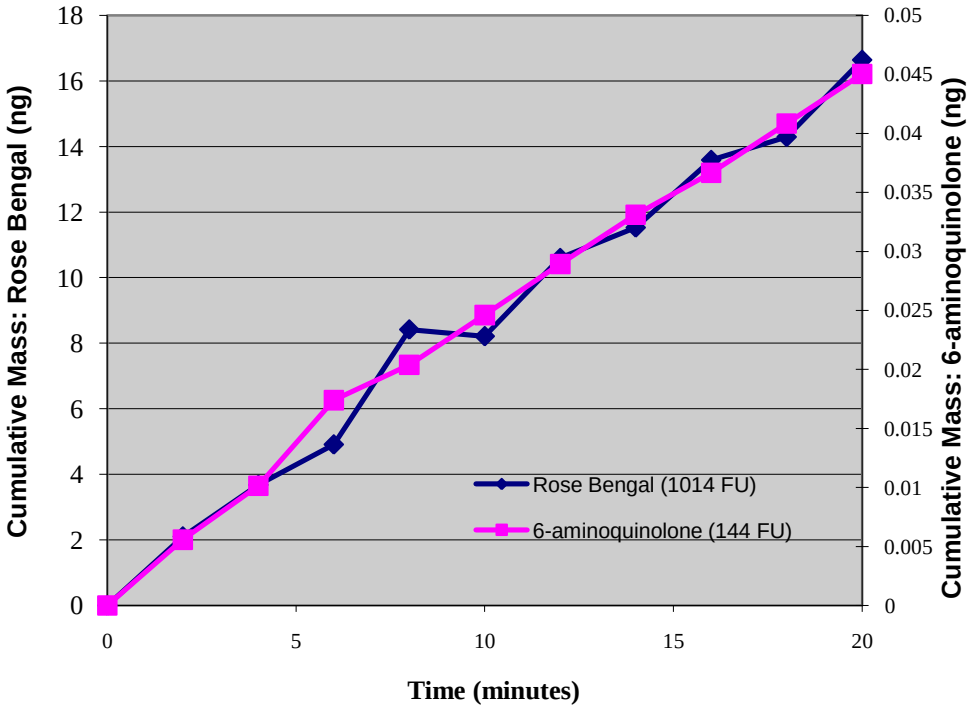

Figure 31. Delivery of model compounds through the assembled device using active pumping at a rate of 50 μL/min of Rose Bengal solution (12.5 μg/mL (N=2)) and 6-aminoquinolone (0.05 μg/mL (N=3))

The device was then inserted into the vitreous so that microneedles could penetrate the intraocular tissues. A 10 mL volume of 0.5 mg/mL Rose Bengal dye was pumped through the device with a syringe pump at a rate of 1 mL/hour. After 8 hours, the eye was assayed for penetration of dye. Approximately 0.0202 mg of dye was detected in the aqueous component of the vitreous body with most of the dye localizing to the gel phase of the vitreous and uveal side of the sclera. The vitreous body was received and separated into the two phases. Dye was delivered to both the vitreous and the posterior space as shown in Figure 32. Rose Bengal dye accumulation was visually evident as shown in panel A and at the posterior pole B.

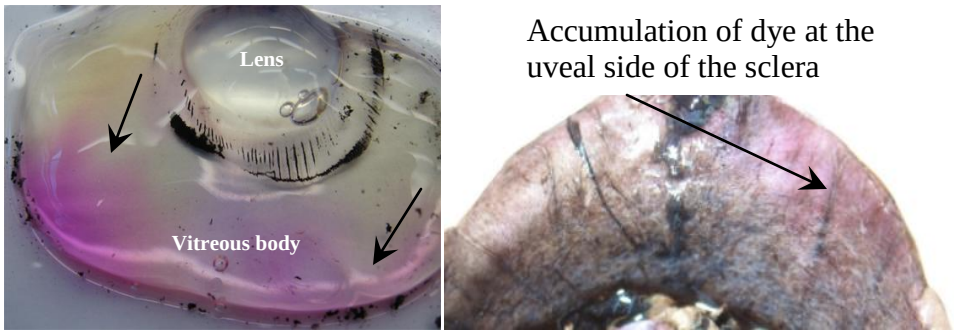

Figure 32. Delivery in ex-vivo bovine eye: intravitreal delivery (A) of dye and (B) dye penetration in the posterior segment after release from the microneedle array

This method allowed provided solution release from a flexible microneedle based device that formed the basis for the remainder of the work. Though delivery was successful using microneedles fabricated using the pipette pulled microneedles, it was determined that microneedles fabricated using an alternative method would improve upon the limitations of pipette pulled tips.

Chapter 6 Fabrication of Single Microneedles using Surface Tension

The first objective was to demonstrate that the hypothesized microneedle fabrication process using surface tension effects could achieve hollow tapered microneedle shapes capable of tissue penetration. Figure 33 shows resultant single microneedles generated using surface tension effects between the fused silica capillary tubing, the HF etchant, air and the paraffin oil as described in Section 4.3.3.2. Single microneedles were obtained from independent etch runs from both larger diameter 323 μm OD tubing and smaller 126 μm OD tubing. Both sets of tubing possessed ID values of 10 μm which were preserved via continuous pumping of water through the inner bore during the chemical etching process.

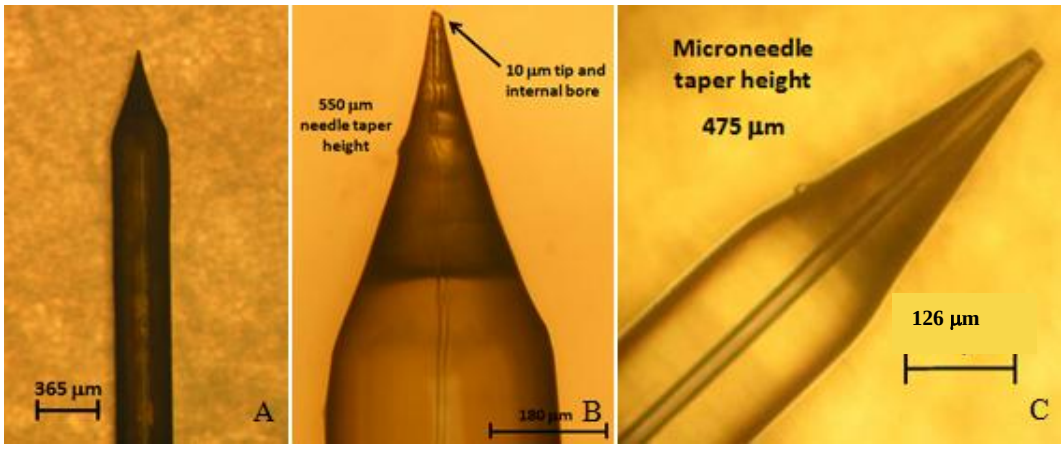

Figure 33. A 323 μm OD/10 μm ID hollow glass microneedle fabricated using surface-tension mediated tip sharpening (A) at 40X magnification. Similar shapes and tip diameters were obtained for 126 μm OD/10 μm ID microneedles (B). A near-field image of a 126 μm OD/10 μm ID microneedle at 200 X magnification (C) shows the uniform and symmetrical structure obtained.

Figure 34 shows several independently etched microneedles fabricated using 323 μm capillary tubing.

The average tip ID and tip base OD of the larger tubing on etched microneedles was 323 µm and 10 µm ID, respectively - equivalent to the dimensions of the starting tubing material. Average tip taper length was 502 µm with a mean cone angle (the angle of the tip with respect to the midline axis of the tubing) of 35°, Figure 35.

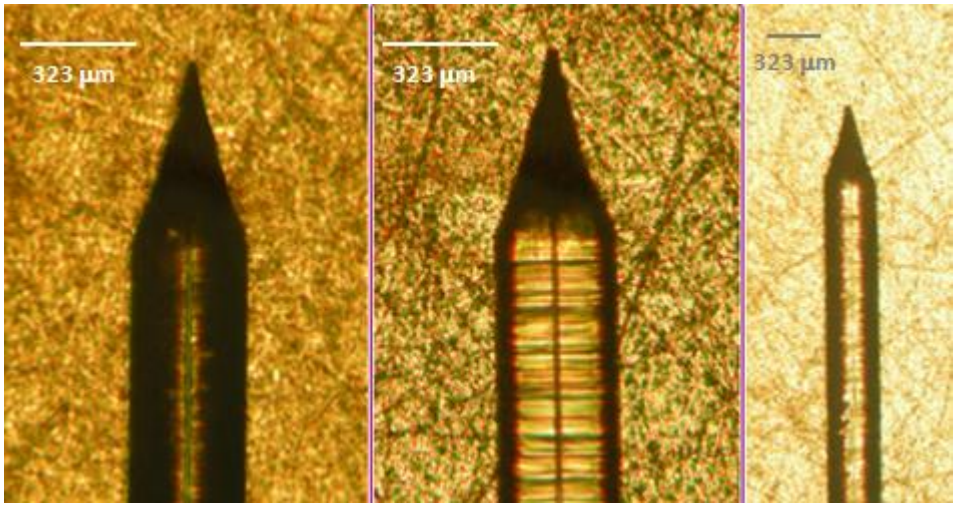

Figure 34. Images show 323 µm OD/10 µm ID tipped microneedles obtained independently illustrating a repeatable resultant shape, taper length and cone angle using the etch processes.

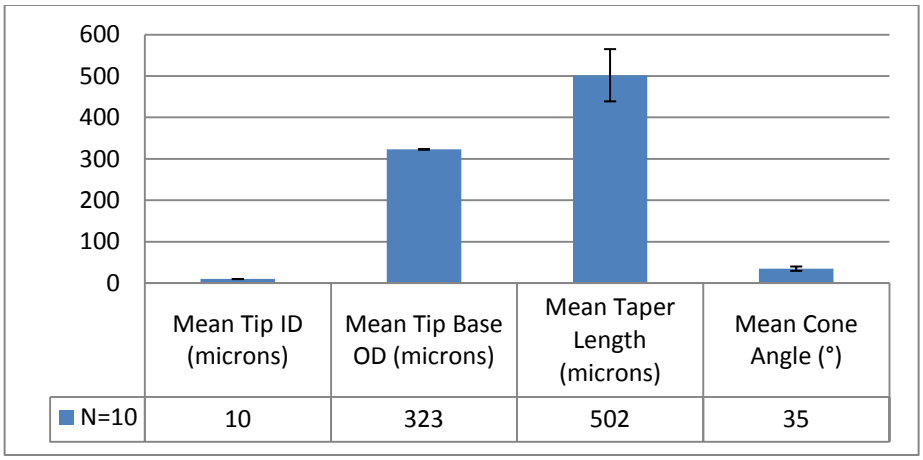

Figure 35. Mean tip ID, tip base OD, taper length and cone angle for microneedles fabricated from 323 µm OD/10 µm ID capillary tubing using surface tension mediated chemical etching.

Figure 36 shows images of three independently etched microneedles fabricated using 126 µm OD capillary tubing. The average tip ID and tip base OD of the smaller tubing was 126 µm and 10 µm ID, respectively - again, representative of the dimensions of the starting tubing material. The average tip taper length was 234 µm with a mean cone angle of 34°, Figure 37.

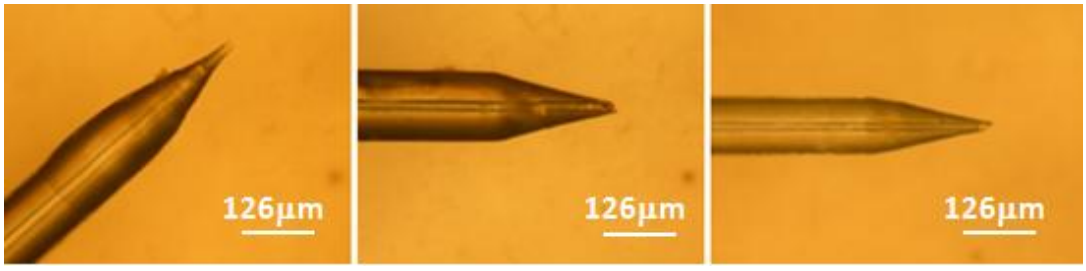

Figure 36. Images show 126 µm OD/10 µm ID tipped microneedles obtained independently illustrating a repeatable resultant shape, taper length and cone angle using the etch processes. Slight visible taper asymmetry was attributed to slight misalignment from a true vertical position of the tubing with the chemical etchant during the chemical process.

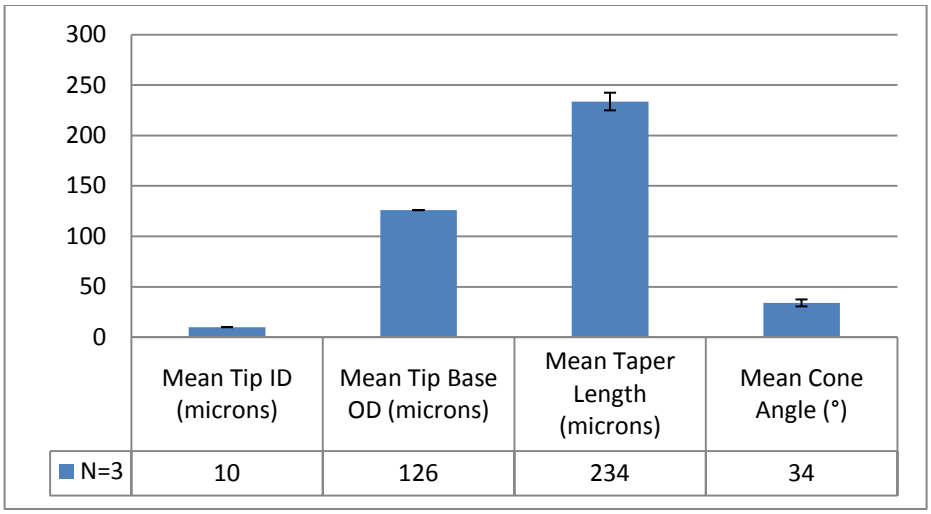

Figure 37. Mean tip ID, tip base OD, taper length and cone angle for microneedles fabricated from 126 μm OD/10 μm ID capillary tubing using surface tension mediated chemical etching.

The mean cone angles of the etched microneedles were significantly greater than those observed with microneedles pulled on the pipette puller. This result was consistent with previous observations reporting that chemical etching methods typically yield larger cone angles than laser-based heat and pull methods [129]. The mean tip ID, tip base OD and cone angle were conserved between the two capillary tubing sizes studied while an observed variation in the mean taper length was observed. One reason for this effect could be the extended reaction times resulting from a greater mass of fused silica that must be consumed by the etchant as the contact angle would be the same for any diameter of tubing.

The method used to make these microneedles has not been described before. The method combines the pumping of water through the internal bore to conserve the native ID with Turner's methods (as described in Chapter 3.2.2) that use an

organic overlayer to modify the interfacial angle. These tips thus created have much shorter taper length and greater cone angles than those fabricated for the nanospray emitters. As the tubing is gradually consumed by the etchant, the products of the chemical reaction fall due to gravity as they are heavier than HF [130]. This continuous flow of products influences the etching rates at different depths as it is filled with both the acid and the products of the ongoing reactions. This causes the meniscus weight to increase to a point after which the weight of the liquid in the meniscus exceeds the surface tension forces causing the meniscus to fall to the next point of stability where the magnitude of surface tension forces at the new position balances the weight of the volume within the new meniscus, Figure 38 [130]. This process continues until a sharp, tapered point is completely formed and an interfacial meniscus is no longer visible. The tip remains protected from further chemical attack by the surrounding solvent.

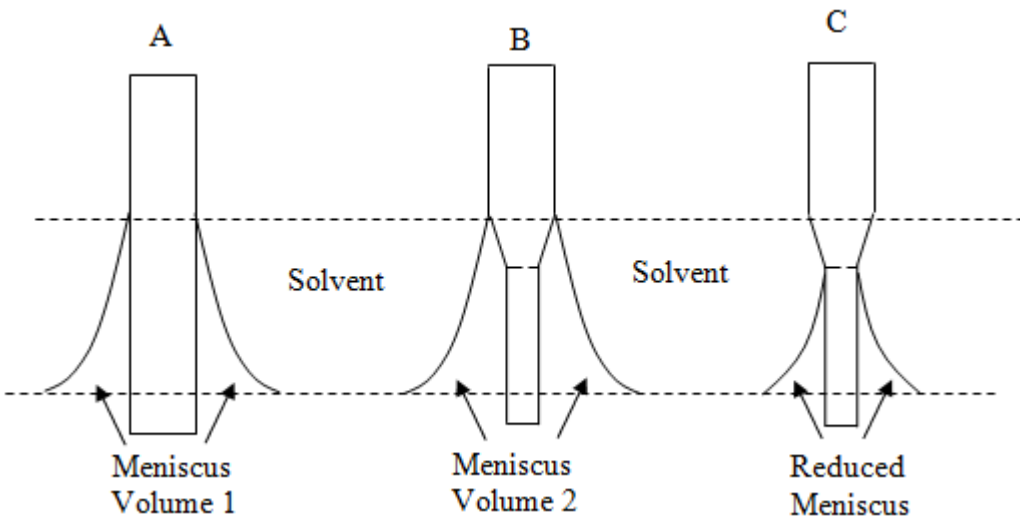

Figure 38. Evolution of taper on an optical fiber via meniscus based chemical etching. Figure adapted from [130].

Previous work done to observe the in-situ evolution of the tapered structures using HF showed that the meniscus does not necessarily slip vertically as a function of the reduced diameter but rather "jumps" down in 5 μm increments at a time allowing the meniscus to remain attached to one positional line of contact until the weight of the meniscus exceeds stiction forces due to surface tension [130].

Even broader cone angles can be realized by reverse etching where the tip is introduced into the HF from the bottom of the etch container while an organic overlayer of a higher density than the HF (e.g. chloroform) rises above [110]. A reduction of the meniscus height is observed in this scenario during tip etching suggesting that the meniscus must rise along the fiber working against gravity forces - leading to wider cone angles

To control the tip angle, it should first be noted that the meniscus height is controlled by the force balance between the surface tension force and the weight of the etchant that has risen along the length of the fiber [131]. Even a minor change in the meniscus height yields a large increase in the volume, and subsequently weight, of the etchant that needs to be counterbalanced by a significant rise in surface tension forces; in contrast, small increases in surface tension have a minor effect on the meniscus height due to this relationship between meniscus height and volumetric-based weight [131].

The meniscus height is directly related to the change in contact angle at the interface as the contact angle affects the profile of the meniscus and the associated volume and weight of the etchant. As such, the meniscus height and the

corresponding resultant tip profile depend primarily on one variable - the contact angle [131]. The final tip shape is governed by the density difference, surface tension and contact angles at the interface [131]. When etching is performed on bare tubing the meniscus formed by the etchant along the fiber is governed by the acid-oil-silica interface - as the fiber is consumed its diameter is reduced in accordance with the laws of superficial tension [132]. The meniscus height falls as the fiber is etched - however the meniscus remains constant when there is a protective coating on the tubing causing the tip formation to be a diffusion driven process [132].

Chapter 7 Site-specific Ex-vivo Delivery via Single Embedded Microneedle

7.1.Embedding Single Microneedles in Micropatterned PDMS Substrates

To demonstrate penetration and delivery in biological tissues, single fabricated microneedles first required integration into a supportive substrate that would adequately handle the forces of penetration. To provide both a flexible backing for compliance with the underlying sclera and a grip for handling the microneedle during device penetration into the model tissues, individually fabricated microneedles were embedded into micropatterned PDMS substrates. Precision alignment of 126 μm-OD fused silica capillary tubing was performed using the process flow shown in Figure 39 . PDMS polymer was cast and molded using a micropatterned master wafer. The tubings were then embedded into micromolded grooves.

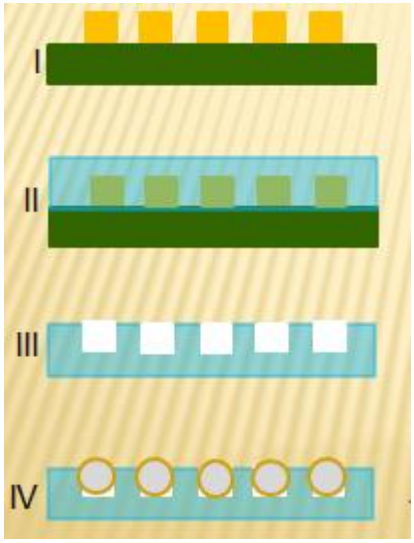

Figure 39. Process flow showing embedding of microneedles into PDMS: the master SU-8 microfabricated mold containing the positive relief microstructured

pattern (I) is used to cast microchannels in PDMS (II) possessing the negative impression of the master mold features (III). The microneedles are then subsequently embedded into the microchannels (IV) for precise alignment and interneedle spacing.

A device showing an example of an embedded microneedle with a length of approximately 300 μm before and after fixation is shown in Figure 40.

Microneedles could be set to any specified length and permanently affixed so that solution delivery to a specific tissue target in the posterior eye could be achieved. (Surface tension forces between the PDMS prepolymer, the glass tubing and air cause uncured PDMS to rise on the edges of the capillary. It was found that this could typically be prevented by dispensing less PDMS glue during the final fixation process to minimize the volume of PDMS that would be subjected to surface tension forces.)

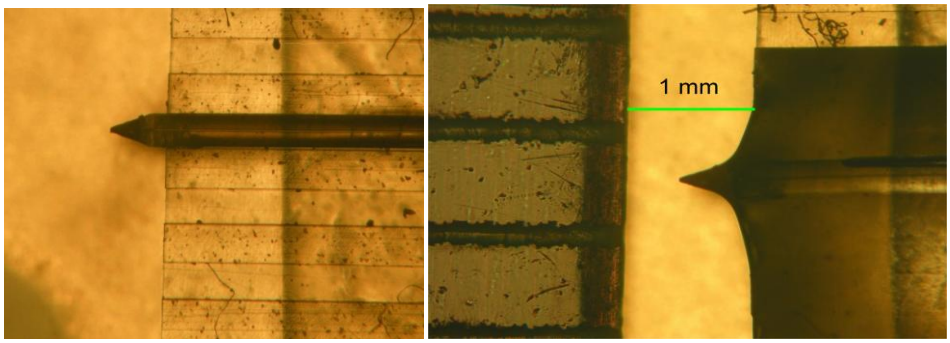

Figure 40. Before final bonding of the tubing (A) and after fixation (B) of a 323 μm OD/20 μm ID microneedle with a corresponding 20 μm tip

Figure 41 shows microneedles positioned at different heights using SU-8 positional markers on the micropatterned length defining master mold. Microneedles could be positioned within a range of 0.050 – 1.1 mm at 50 μm increments. The approach

provided the necessary control over the device dimensions based on delivery to particular tissue target.

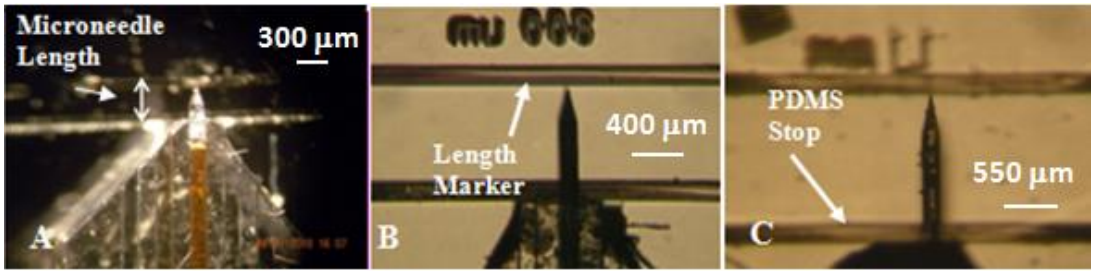

Figure 41. The front edge of the straight-cut PDMS is placed flush against the PDMS stop patterned in SU8. The microneedle is then manually positioned to the desired length using a microscope. Microneedles are shown at different lengths of (A) 300 µm (B) 800 µm and (C) 1.1 mm.

Ordinarily, PDMS prepolymer was dispensed to barely cover the surface area of the PDMS section housing the microneedle; however, if excessive PDMS was dispensed, the prepolymer would flow over the edge of the PDMS and onto the base of the microneedle – even at the elevated temperature of 120°C. As it was difficult to accurately measure microscale volumes of prepolymer, it was estimated that no more than several hundred µL was required for fixation of the microneedle into the alignment grooves.

7.2. Microneedle Penetration of Bovine Sclera

Once the microneedle was embedded, the next objective was to test whether the embedded microneedle could insert and penetrate into the sclera without delamination delamination or fracture of the microneedle. Accordingly, an ex-vivo model using enucleated bovine eyes was first developed. Trypan blue was used to visualize a

microneedle induced defect on isolated bovine sclera using the smaller dimensioned microneedle.

Figure 42 shows the insertion point revealing successful penetration of a 126 μm OD/10 μm ID microneedle on the episcleral, or outer, side of the sclera.

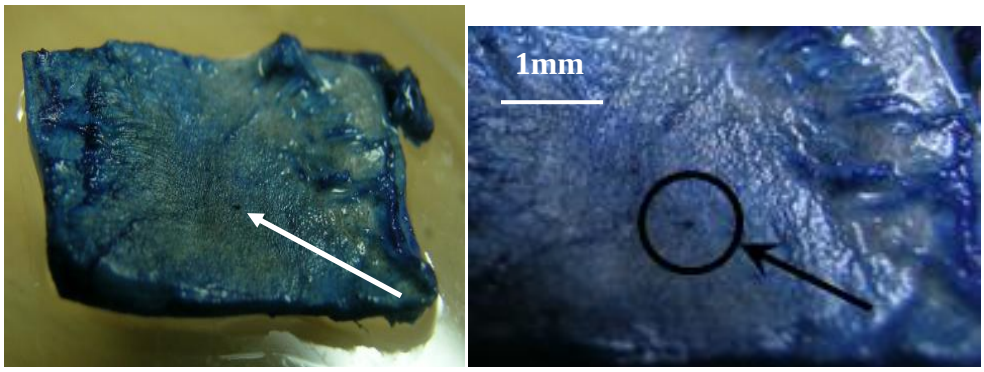

Figure 42. Microneedle insertion point in bovine sclera after penetration using a single embedded 126 μm OD microneedle on the episcleral side using trypan blue staining of porcine sclera after treatment with a single 126 μm OD microneedle with a 10 μm tip.

To show adequate penetration into the scleral tissues, a single embedded 126 μm OD/10 μm ID microneedle, approximately 450 μm tall, was used to pierce the episcleral side of a section of isolated bovine sclera. As shown in Figure 43, the microneedle was able to not only pentrate the sample, but was able to adhere to the tissue with sufficient frictional forces between the microneedle surface and the surrounding organic matrix to remain attached under the weight of the tissue section itself.

A subsequent test using a freestanding device representative of an actual drug delivery application wherein the device would remain embedded within the sclera

is shown in Figure 44. The device remained embedded after microneedle insertion and also remained fixed within the scleral matrix upon inversion of the globe by further subjecting the device to gravitational forces as shown in Figure 45. The 126 μm OD/10 μm ID microneedle was subsequently removed manually leaving behind a visible defect.

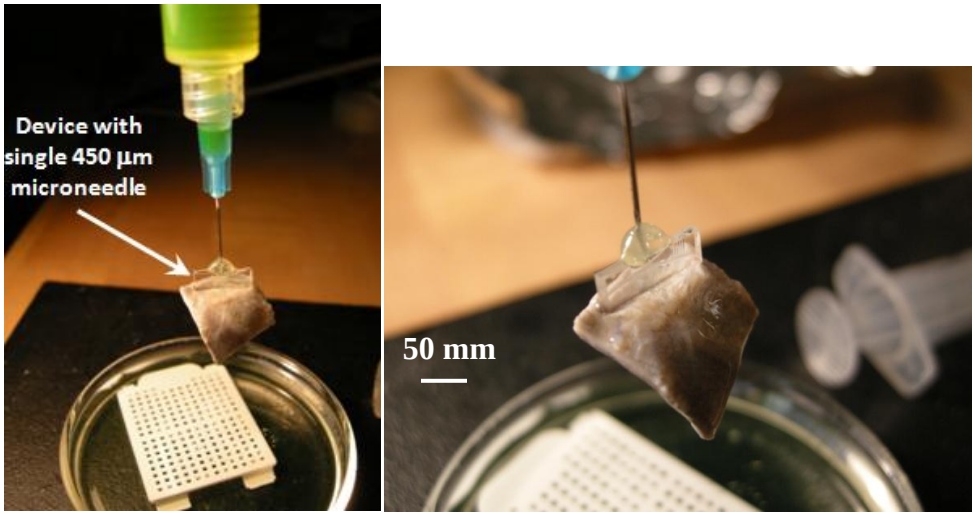

Figure 43. Insertion of a single 450 μm tall 126 μm OD/10 μm ID microneedle into excised bovine sclera; penetration was sufficient to raise the sample due to frictional adhesion between the microneedle tip and tissue. The tissue remained adherent to the tissue and did not fall under its own weight.

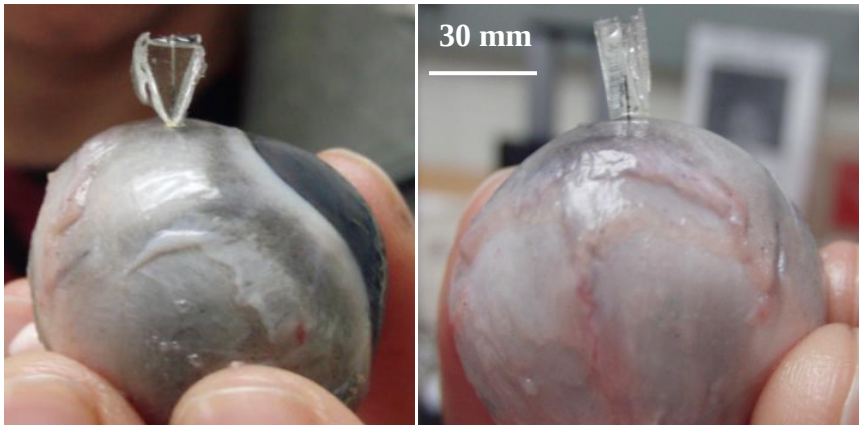

Figure 44. A single microneedle inserted into a whole bovine globe was able to insert and remain adherent with the scleral matrix. The adhesion (i.e. frictional forces) between the microneedle and the tissue was adequate to balance the weight of both the PDMS substrate and the embedded microneedle.

Figure 45. Strong adhesion forces between a single microneedle embedded in a PDMS substrate prevent decoupling of the device under gravity forces (A) and visible insertion point (B) remaining in the sclera after manual removal of the device.

7.3. Increase of Transscleral Permeability using Microneedle Induced Defects

Once microneedle insertion and penetration into scleral tissues and whole globes was confirmed, studies were then performed to determine whether perforations made by embedded microneedles actually penetrated sufficiently through the sclera to alter the permeability of a model compound through the scleral matrix. Transscleral permeability of a 40 kDa FITC-Dextran molecule – a commonly used model compound for transscleral flux - was measured on sclera isolated from whole globes subjected to microneedle insertion.

Diffusion experiments were first performed on intact sclera with no defects. Experiments were then repeated on sclera that was treated with microneedles to examine any changes in apparent permeability based on the treatment.

Figure 46 shows the accumulated mass transferred, averaged between three independent experiments, calculated from fluorescence intensity measurements taken from the receptor chamber for 40 kDa diffusing through intact bovine sclera. During each of the experiments, the compound was not detectable for the first six hours. Approximately 0.215 $\pm$ 0.1 μg of dextran diffused across intact sclera over 8 hours.

Based on the fluorescence reading at 8 hours, a K_{trans} = 1.0 X 10^{-8} cm/s was calculated for the intact sclera based on a 9-mm orifice, a 3.4 mL chamber volume and an initial donor concentration of 1.67 mg/mL. The dextran molecular weight was 40,000 g/mol.

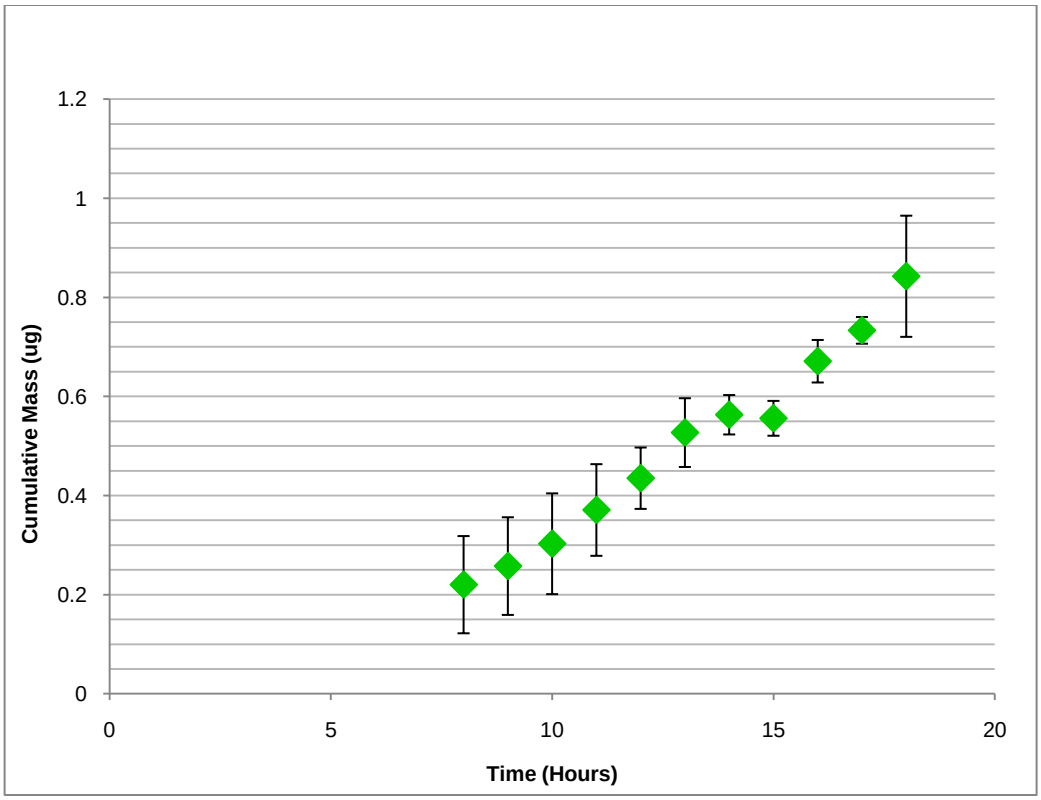

Figure 46. Average Cumulative Mass vs Time for 40 kDa-Dextran Transfer across Intact Bovine Sclera at 25°C (N=3)

To assess whether transscleral permeability increased upon treatment of the sclera with a 1 mm tall 323 μm OD/10 μm ID microneedle, a section of isolated sclera was laid on a flat surface. The embedded microneedle was used to make five random insertions into the tissue. The section was then placed in the diffusion chamber using the same set of experimental parameters as the intact case and fluorescence readings were taken for up to 48 hours.

Figure 47 shows that after approximately 8 hours, the total accumulated mass in the receptor chamber was between 11.4 μg $\pm$ 0.71; a 50-fold increase in total mass

transferred. For the apparent permeability calculation, the K_{trans} due to the defects was calculated after 8 hours. The $k_{transapp}$ = 3.73 X 10^{-7} cm/s for the microneedle treated sclera – an increase of one order of magnitude.

Jiang *et. al.* stated that there may be utility in residual perforations or "holes" in tissue to increase the corneal permeability to topically applied drugs. They found that a single orifice created by a microneedle creating an opening with a cross-sectional area of 8.5 X 10^{-5} cm^2 resulted in undetectable changes in the permeability of fluorescein in the cornea. They further calculated that approximately 66 perforations of specified area would be required to increase the permeability of the cornea by a factor of two as holes introduced by microneedles result in local enhancements to tissue permeability but the overall contribution was minor compared with the overall surface area of the cornea itself [87].

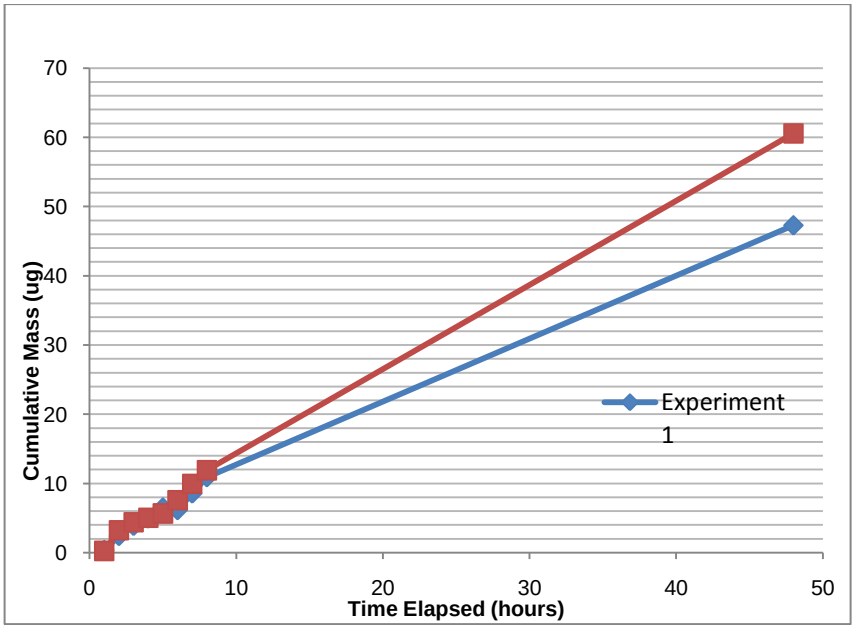

Figure 47. Cumulative Mass vs Time for 40 kDa FITC-Dextran in Bovine Sclera penetrated 5 times with a 1 mm long 323 μm OD/10 μm ID microneedle

Microscopic images of the defects introduced by the 1mm tall 323 μm OD/10 μm ID microneedle are shown in Figure 48. The defect size was approximately 300 μm in diameter.

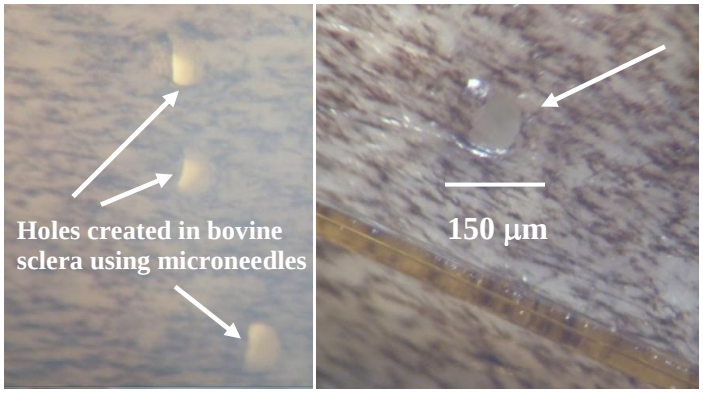

Figure 48. Perforations in bovine sclera after penetration using a 1 mm tall 323 μm OD/10 μm ID microneedle. Defect sizes are approximately 150 μm dia estimated using a section of 150 μm capillary tubing.

With defects introduced into the tissue, the enhancement of permeability was dramatic as would be expected with holes introduced across a 9 mm diameter circular section of sclera.

Permeability of 40 kDa FITC-Dextran has been reported in rabbits to be 2,79 $\pm$ 1.58 X 10^{-6} cm/s though it was stated that solute diffusivity in bovine sclera and human sclera is generally to be lower than that for rabbit sclera [14]. The permeability of 40 kDa FITC-Dextran in isolated human scleral specimens has been experimentally determined to be 49.0 $\pm$ 24.0 X 10^{-7} cm/s, so the experimentally determined value for 40 kDa FITC-Dextran in bovine of 1.0 X 10^{-8} cm/s is reasonable and consistent with these reported findings [133].

7.4. Trypan Delivery using a Single Embedded Microneedle

As embedded microneedles were able to achieve sufficient penetration within scleral tissue, the next objective was to demonstrate active delivery to specific intraocular tissue layers using microneedles embedded to various lengths in an ex-vivo model. For these studies, whole porcine globes were used. Porcine eyes have previously been found to serve as excellent models for human eyes [34]. To confirm the suitability of porcine globes to serve as a reasonable model for delivery, microneedles of both sizes, 126 μm OD/10 μm ID and 323 μm OD/10 μm ID were inserted into fresh porcine globes. Both sizes of microneedle penetrated the sclera with ease, Figure 49. Additionally, the 1-mm tall device remained embedded in the tissue balancing the entire weight of the PDMS structure.

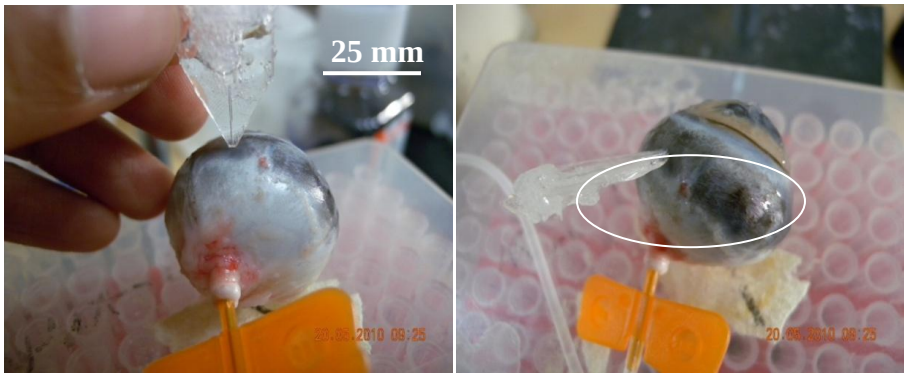

Figure 49. Insertion and retention of a 1-mm tall 323 μm OD/10 μm ID microneedle into porcine whole globes

To estimate expected thicknesses to be encountered by the microneedles, Figure 50 shows average scleral thickness from three measured whole porcine globes.

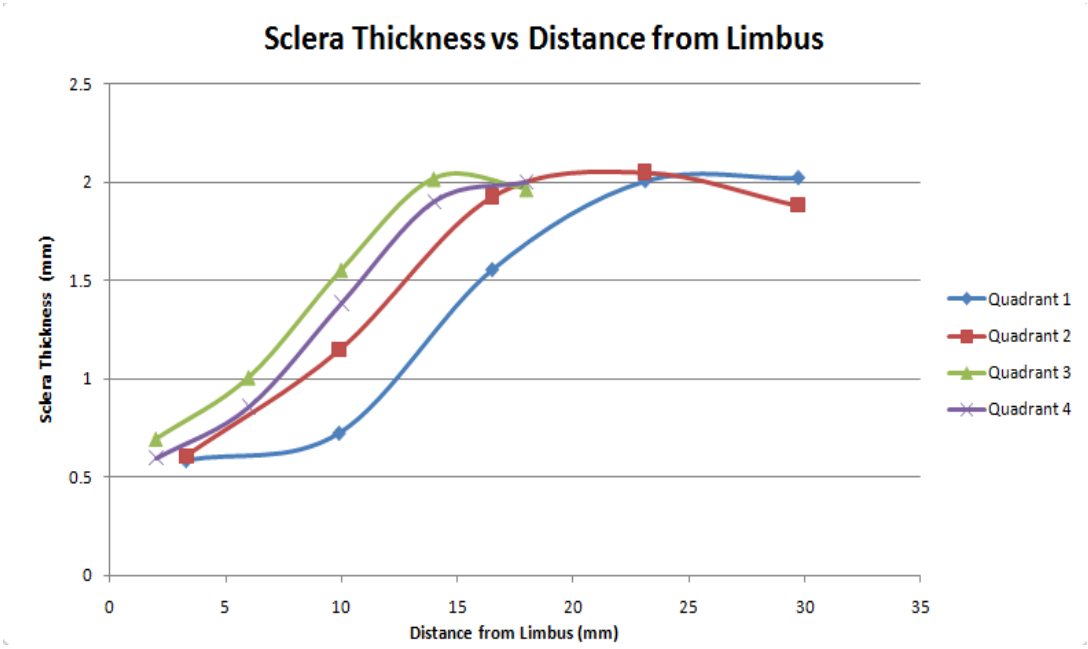

Figure 50. Average scleral thickness with respect to distance from the corneoscleral limbus for the four quadrants defined

Measurements for the porcine sclera thickness were reasonable compared with earlier published measurements of 0.43 mm + 0.13 mm approximately 6 mm from the limbus in adult porcine pigs (weight $\geq$ 27 kg) [134]. As the eyes used for the thesis came from animals that were approximately 50 kg, the thickness approximately 5 mm from the limbus is slightly higher but close to previous reported measurements. Previously reported thickness values at 10 - 12 mm posterior to the limbus, where microneedles would be inserted, were between 0.6 - 0.9 mm. Slightly greater thickness values, between 0.65 - 1.5 mm were found in porcine eyes used in this study.

Trypan blue was initially selected to test for delivery to the tissues due to ease of visualization for both tissue penetration and leaks within the delivery system.

The first successful trypan blue infusion was performed with a126 μm OD/10 μm ID microneedle was embedded to a height of 750 μm as shown in Figure 51.

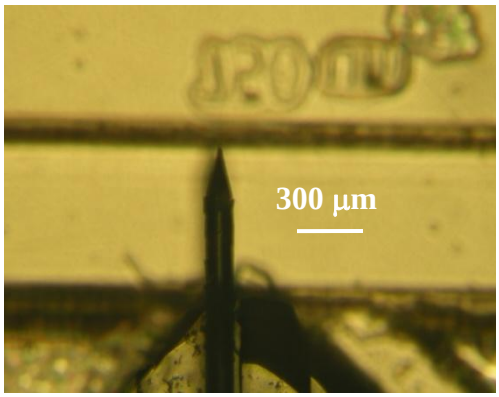

Figure 51. A 126 μm OD/10 μm ID microneedle set to a height of 750 μm using the dimensions defined in the SU-8 master wafer.

The microneedle was connected to the syringe and the syringe was attached to a nanoliter pump. After inflating the globe to recover tension, the microneedle was then inserted into the surface of the globe until it was firmly held within the sclera. The flow rate was then set to 100 nL/min. A total volume of 5.1 μL was delivered over the 51 minute infusion time. After the infusion, device was removed and the injection site was inspected for penetration.

Figure 52 shows the insertion point of the microneedle approximately 12 mm posterior to the limbus. After infusion, the whole globe was dissected to assess localization of injected trypan blue. The vitreous showed no evidence of trypan blue dye indicating that the microneedle had not penetrated fully though the posterior tissues and retina. The retina and choroidal layers were then peeled away

from the sclera using a cotton swab. However, as the choroidal layer is blue-green in color, it was not possible to assess trypan blue delivery to the choroid.

Finally, a small section of sclera surrounding the insertion point was cut. The thickness of the sclera at the injection point was measured to be approximately 800 μm. This was consistent with the observation that the microneedle had not penetrated through to the vitreous. Histological analysis of the samples showed evidence of trypan blue infiltration into the tissue was observed as shown in Figure 53.

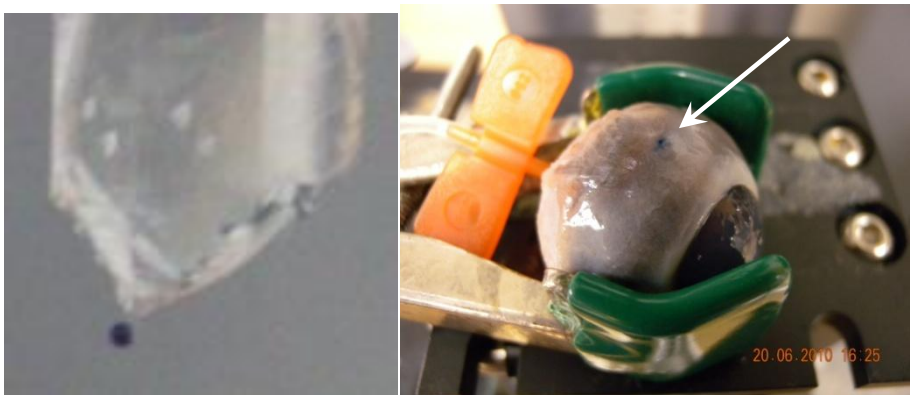

Figure 52. A 126 μm microneedle showing a droplet of trypan blue from a 126 μm OD/10 μm ID; the insertion point (white arrow) is visible after the device was removed

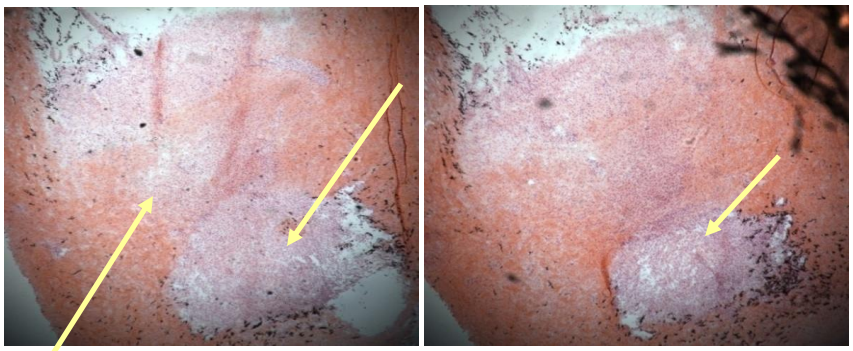

Figure 53. Arrows indicating sections of intrascleral trypan blue delivery using a 750 μm tall 126 μm OD/10 μm ID microneedle

7.5.Intravitreal Delivery of Rhodamine

In order to demonstrate site-specific delivery of rhodamine using a microneedle of a defined and precise length, it was hypothesized that a single hollow 365 μm microneedle, embedded to a height of 1.1 mm, could deliver the model drug solution intravitreally as the average thickness of the sclera at a position 12 mm posterior to the limbus is approximately 0.8 – 1.2 mm. For this particular experiment, a 1.1 mm tall 323 μm OD/10 μm ID microneedle was used to deliver rhodamine at a rate of 200 nL/min for a total infusion time of 65 minutes. The device used for the experiment is shown in Figure 54.

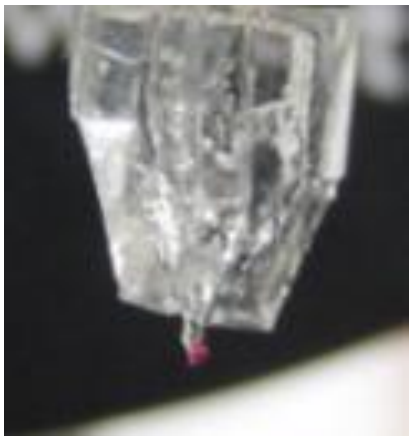

Figure 54. Droplet of rhodamine emerging from the tip of a 1.1 mm tall 323 μm OD/10 μm ID microneedle

The injection site on the globe was always estimated to be approximately 12 mm behind the limbus. After the 65 minute infusion, the device was removed from the globe and dissected to investigate localization of the dye.

The scleral section containing the insertion point was excised and measured to be approximately 300 μm thick. The excised tissue was embedded in OCT, snap frozen in liquid nitrogen-cooled isopentane and cut to 50 μm sections. The thickness of the sections however was increased to 50 μm after losing the bulk of the sample when first attempting to cut sections at a thickness of 10 μm on the cryostat. Due to the presence of the microneedle-induced defect in the tissue, ultra-thin sections were difficult to retrieve from the cryostat stage after cutting. As such, the cutting thickness was increased to 50 μm. Accordingly, the visibility of the microneedle indentation and observation of fluorescence could easily be detected while maintaining tissue section integrity and continuity. The sections were dried in graded ethanol and H&E stained and viewed using the LSM510 confocal microscope as described in Section 2. Figure 55 shows both an optical image and a fluorescent image of a 50 μm section showing an indentation due to the microneedle penetration. The fluorescent image, with background fluorescence due to the H&E stain (H&E staining was abandoned hereafter as it was not necessary), shows a localized area of greater signal intensity near the defect. Figure 56 shows a section taken several sections towards the insertion point and away from the section shown in Figure 55. The microneedle insertion depth is approximately 100 μm suggesting that complete scleral penetration had not been achieved.

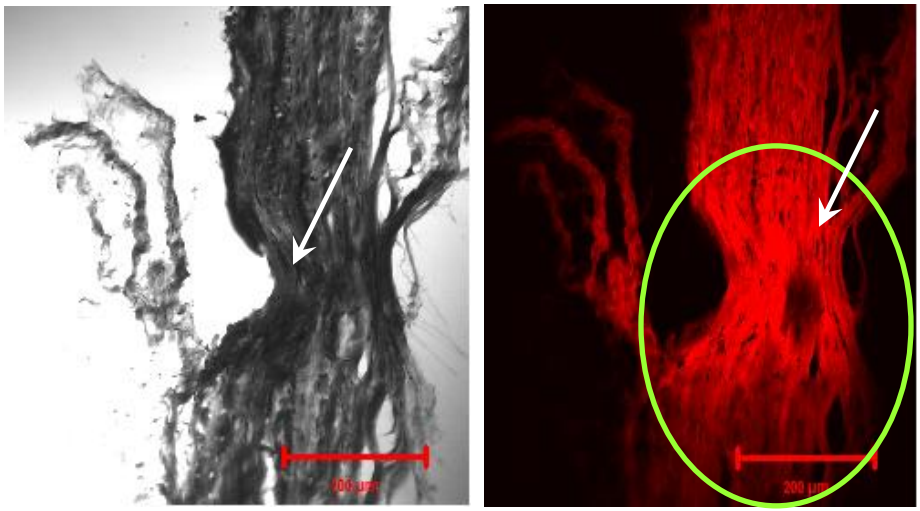

Figure 55. Light microscope image of section showing evidence of microneedle insertion (white arrows) at a distance away from the central point that actually penetrated the sclera. 50 μm sections were cut across the plane containing the insertion point to reveal the cross section. Sclera from this particular sample was measured to be ~300 μm thick. The fluorescence image shows enhanced fluorescence signal indicating (circle) rhodamine infusion near the microneedle insertion site

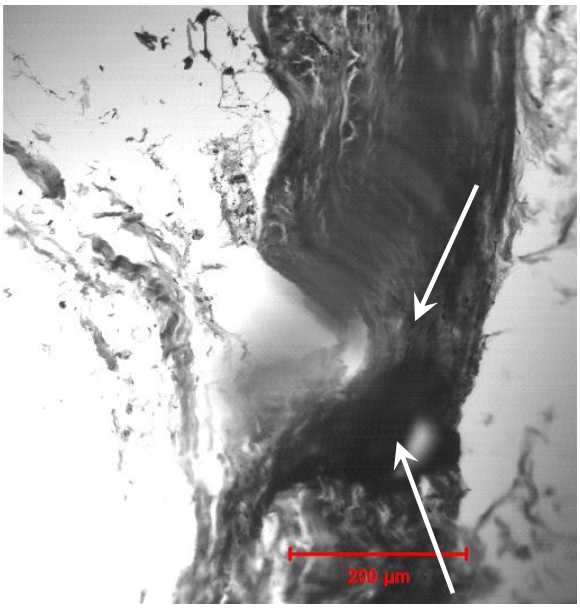

Figure 56. Light microscopy image of a section cut several sections away from the previous section in the direction towards the microneedle insertion site showing increased depth of penetration (indicated by arrow)

Though histological analysis revealed intrascleral delivery, a portion of the injected 13.2 μL of rhodamine was visible within the vitreous body post-infusion as shown in Figure 57(A).

Figure 57 (B) shows a control vitreous that does not present with any trace of dye in the visible range. The slight tint of color visible in control vitreous was attributable to minute retinal membrane. It is presumed that although there was no evidence of complete microneedle penetration, the intrascleral depot of dye delivered to the 300 μm scleral membrane was sufficient to allow solute transport to the vitreous body over the 65 minute delivery period.

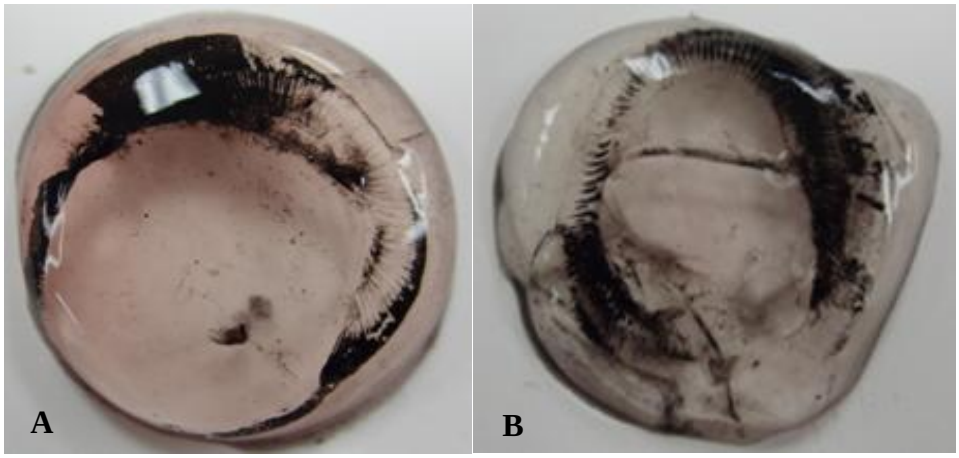

Figure 57. Rhodamine B was injected at a flow rate of 200 nL/min for 65 minutes. Post-dissection inspection revealed accumulation of the delivered 13.2 uL (A). Control vitreous body (B) is shown for comparison.

A repeat of the infusion experiment was performed using a 1.1 mm long 323 μm OD/ 10 μm ID microneedle at a flow rate of 500 nL/min for 40 minutes.

After the infusion period, histological analysis and globe dissection was performed to determine localization of dye. Globe dissection did not show any observable levels of rhodamine at the scleral floor, choroid, retinal or vitreous layers. However, images of histological sections containing the microneedle insertion point showed evidence of microneedle defects co-localized with fluorescence from the injected compound as shown in Figure 58.

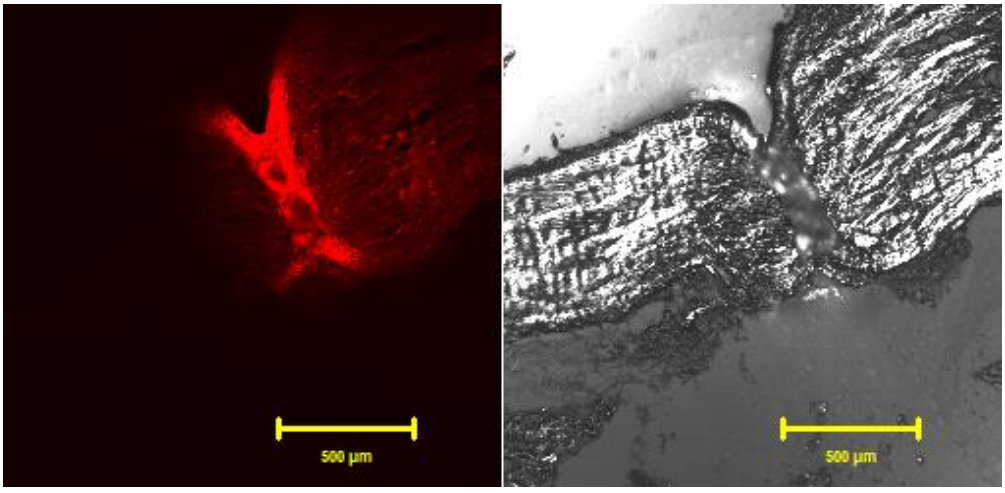

Figure 58. Intrascleral release of rhodamine associated with penetration of microneedle

Although microneedles were observed to penetrate the sclera, full penetration across the sclera was not observed. This was attributed to the insufficient stability of an early delivery setup that used a manually adjustable micromanipulator to insert the microneedle into the whole globe. It was assumed that the manual speed associated with the micromanipulator was too slow to effectively penetrate the sclera. Improvements to the setup were made to ensure microneedle penetration was equivalent to the total microneedle length and a shift to manual insertion was

implemented to impart a swift, instantaneous insertion approach for device insertion.

The next infusion was performed using a 323 μm OD/10 μm tip 1.1 mm tall microneedle without the micropositioner using manual device insertion as previously described in the Methods section. The device was inserted into fresh porcine whole globes at a random position and connected to a syringe pump using a delivery rate of Q = 500 nL/min. A total of 20 – 25 μL of dye was delivered for each of the experiments described. The total infusion time was 25 minutes.

Figure 59 and Figure 60 show the results from this delivery experiment. After infusion, the eye was dissected and analyzed. Upon extraction of the vitreous body, a single depot of rhodamine was visible as shown in Figure 59. The layers of the posterior segment were analyzed and no dye was found in the retina, suprachoroidal space or the scleral floor. Inspection of the sclera did reveal a single through hole, with no observable evidence of dye, as shown in Figure 60 indicating that the microneedle successfully pierced through the intraocular tissues using manual device insertion to deposit the total volume of 20 uL into the vitreous. The sclera at the insertion site was measured to be 300 μm thick.

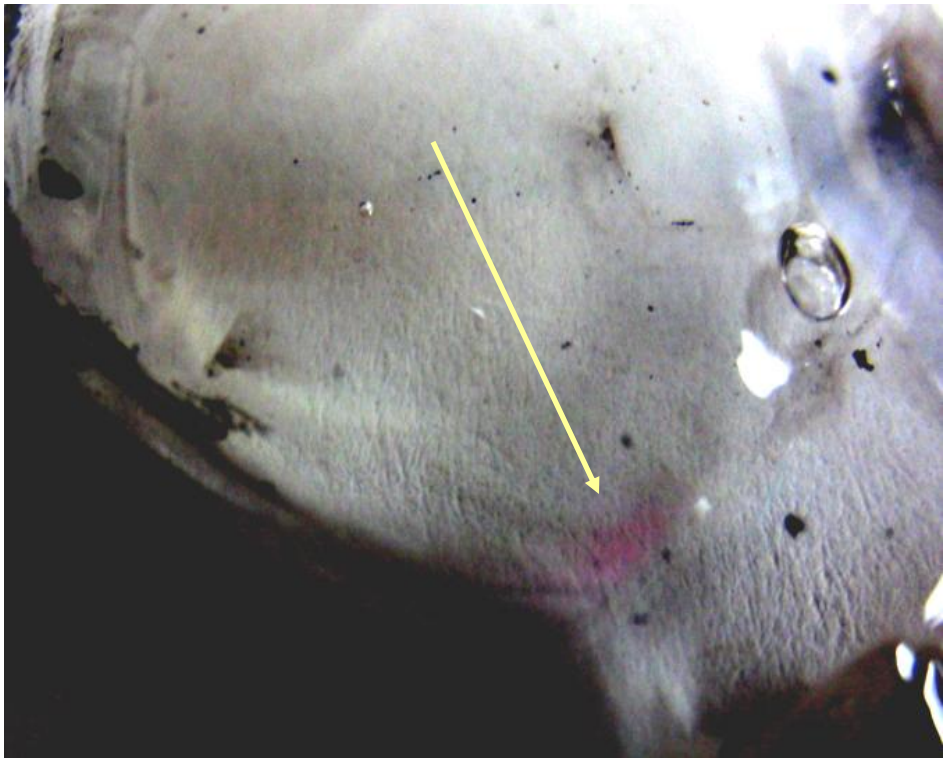

Figure 59. Depot of Rhodamine B delivered intravitreally over 25 minutes

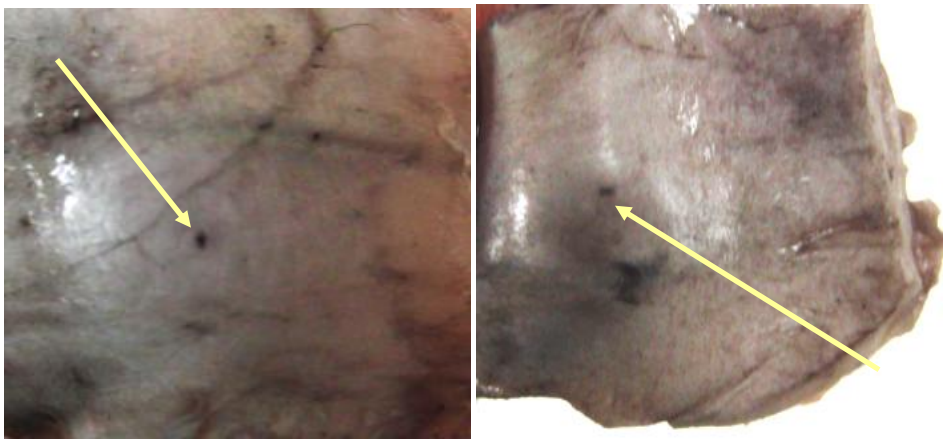

Figure 60. Episcleral side insertion point (A) and uveal side defect (B). There was no evidence of transscleral, suprachoroidal or retinal delivery – only the singular intravitreal depot.

Figure 61 and Figure 62 show fluorescent and corresponding light microscope images taken with the confocal microscope showing release of rhodamine into the

sclera. The microneedle indentation point is clearly visible in both cases. Though the microneedle was 1.1. mm tall, the sections shown were taken some distance from the central point of insertion. As such, a reduced depth of insertion was observed in the images.

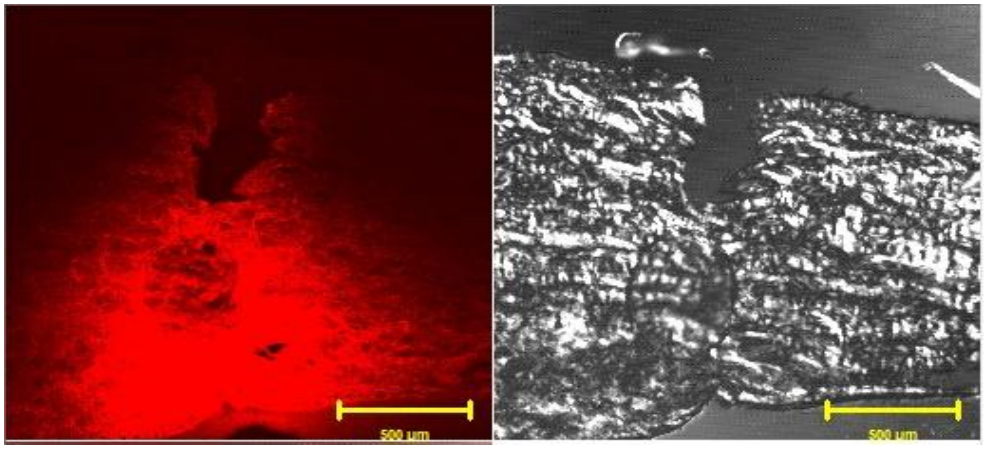

Figure 61. Intrascleral/transscleral release of rhodamine after infusion; note microneedle insertion point

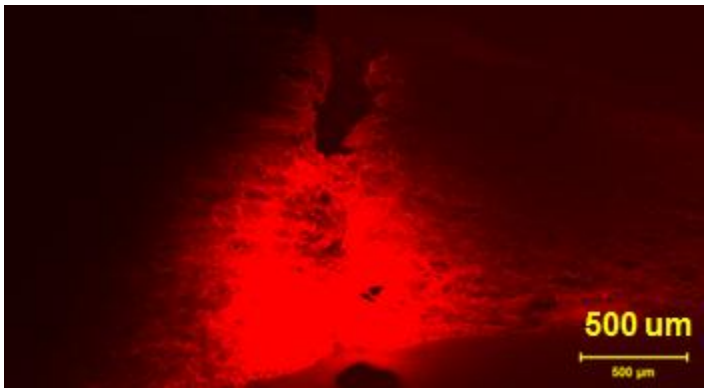

Figure 62. Microneedle insertion point showing attenuation of fluorescence signal proximal to the region adjacent to the microneedle-induced defect.

Interesting to note is the difference in localization between the two intravitreal infusions. In the first case, the rhodamine had completely dispersed into

the aqueous phase of the entire vitreous most likely a result of an extended run time of the experiment for 65 minutes after intrascleral depot delivery of the rhodamine. In the second case however, the run time was only 25 minutes and the corresponding dispersion radius is contained to the localized site of injection within the vitreous body itself.

To demonstrate that delivery of rhodamine was solely due to active pressure actuation through the microneedle with negligible delivery contribution due to passive diffusion, a control experiment was performed whereby conditions were identical to those used in the preceding three experiments except that the infusion rate at the syringe pump was set to Q = 0 nL/min. The device was inserted into the eye, and though coupled fluidically to the rhodamine reservoir, was set to Q=0 flow rate for 40 minutes. After 40 minutes, the device was removed. Though, the insertion point was visible there was no dye accumulation in the vitreous even though the microneedle had fully inserted and penetrated through the sclera as shown in Figure 63.

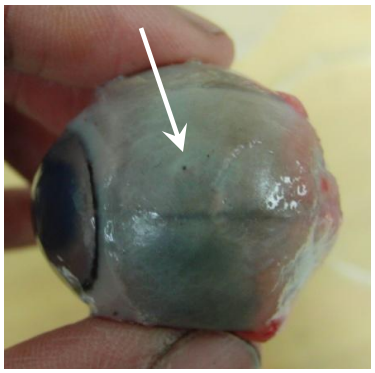

Figure 63. Visible insertion point (shown by arrow) on globe after mock delivery experiment

Figure 64. Microneedle insertion point (shown by arrow) is visible on the uveal side indicating microneedle penetration through the sclera. However, there was no observable evidence of any dye released to the vitreous humour through passive diffusion alone.

7.6. Transscleral, Suprachoroidal and Retinal Delivery of Rhodamine

To further study the effect of altering microneedle length on delivery target, infusions were performed using slightly shorter microneedles 1 mm in length using the dimensioning tool with a 365 μm OD/10 μm ID tip. Dye was delivered at the same position on the whole globe at a slightly greater rate of 500 nL/min for 43 minutes. Upon dissection of the eye, no dye was visible within the vitreous body. However, there was visible dye localization to the virtual space between the retina and choroid (typically referred to as the suprachoroidal space) as shown in Figure 65 (A). Dye was also visible on the actual scleral floor as shown in Figure 65 (B) after removal of the choroid with a cotton swab while further dissection showed that most all of the 26.5 μL of dye segregated to the retina as shown in Figure 65 (C).

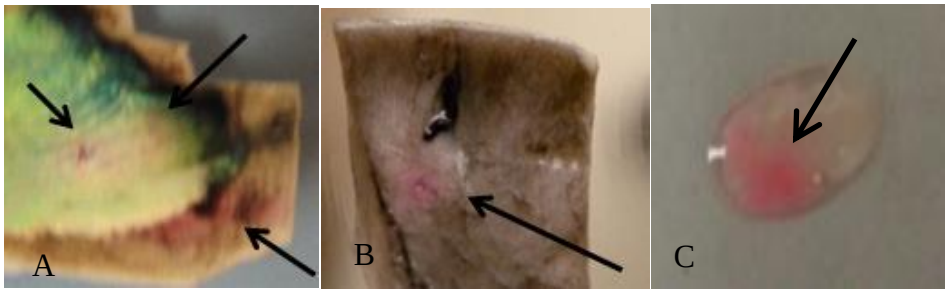

Figure 65. The device, this time embedded with a 1 mm long 323 μm OD microneedle with a 10 μm tip was inserted into an identical position on the porcine globe. Rhodamine B was injected at a flow rate of 500 nL/min. A small portion of the total 26.5 μL delivered volume had localized to the suprachoroidal space just anterior to the choroid (A) while further revealed staining of the scleral floor with a microneedle impression (B). Most of the volume delivered had flowed to the retina as shown in (C).

Though the microneedle was only 100 μm shorter in height, it was sufficient to prevent delivery into the vitreous humour in this case. It should be noted however that this could either be attributed to a slightly shorter microneedle or inter-animal variation in scleral thickness distribution. For example, the section of sclera shown in Figure 65 (B) illustrates how dramatic the gradient of tissue thickness with radial position in sclera can be. The sample shown is approximately 7 mm x 5 mm in area while the measured thickness gradient within the small 35mm^2 area was greater than 1 mm.

The scleral sample was then analyzed using confocal microscopy to observe depth of microneedle penetration into the sclera and whether the fluorescent dye solution was actually delivered intrasclerally in addition to the sites previously identified, i.e. to the scleral floor, the retina and the suprachoroidal space. Microscopic analysis of tissue cross-sections near and across the microneedle

insertion pathway showed that the microneedle completely penetrated the sclera at the insertion point of the microneedle tip as shown in Figure 66 (A). This image is consistent with the visual observation of rhodamine on the scleral floor shown in Figure 65 (B). Evidence of intrascleral penetration was observed at sections several hundred microns away from the point of microneedle traversal. However, consistent with the fact that the tip opening was at the central portion of the serial cuts, the amount of dye delivery was higher within the scleral tissue when compared with the tissue section containing the insertion point. Figure 66 (B) - Figure 66 (F) show sections taken from the central section where intensity of rhodamine is not as high. Note depth of penetration is reduced with an associated reduction of fluorescence intensity indicative of decreased volume of rhodamine as distance increases from the point of microneedle insertion.

Retina samples were further imaged using fluorescence microscopy to confirm the visual evidence of rhodamine penetration of dye. This is shown in Figure 67 (A) while no autofluorescence was observable in control retina Figure 67 (B).

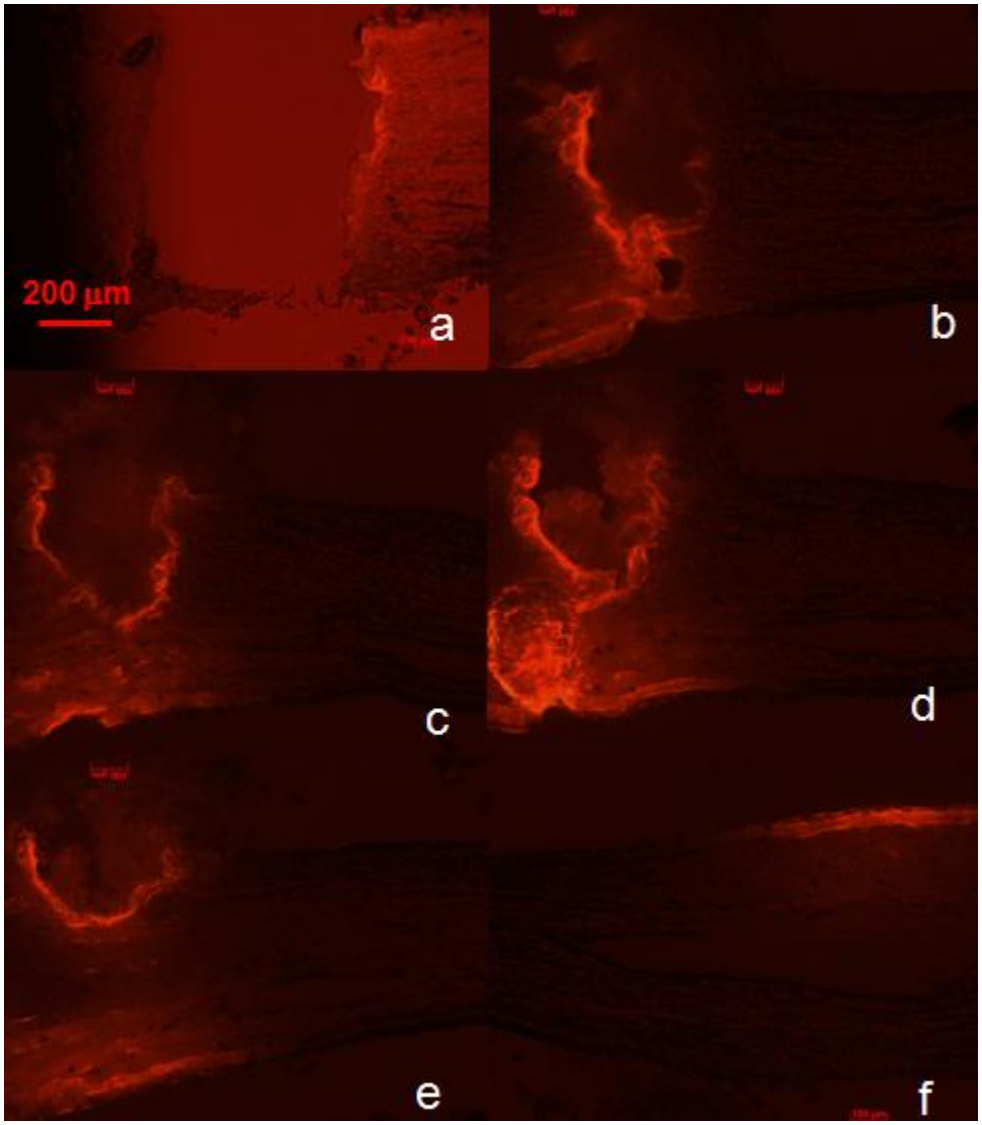

Figure 66. Post-delivery images of porcine sclera taken using confocal microscopy showed transscleral penetration of the 1 mm microneedle delivering Rhodamine B at the insertion point (a) 100 µm from the insertion point (b) 200 µm from the insertion point (c) 250 µm from the insertion point (d) 300 µm from the insertion point (e) 450 µm from the insertion point and (f) 500 µm from the insertion point.

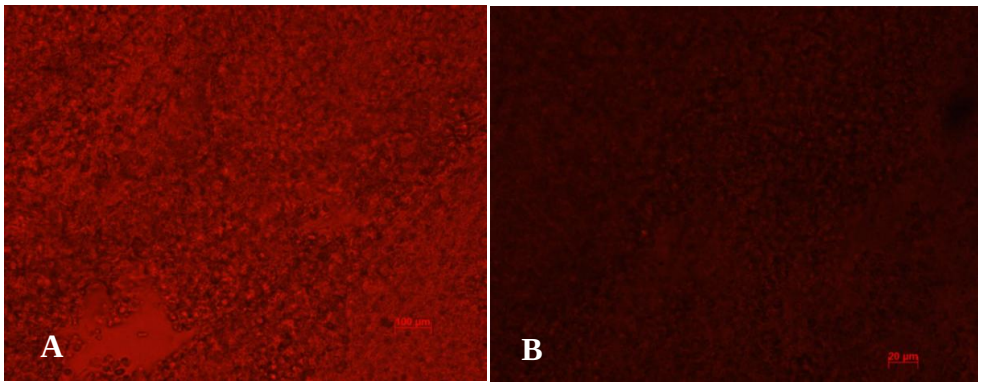

Figure 67. Accumulation of a portion of the 26.5 uL rhodamine dispensed was visually observed in detached retina and further confirmed using fluorescence microscopy (A). No autofluorescence of equivalent intensity could be detected in control retina samples (B).

7.7. Intrascleral Delivery of Rhodamine

The most dramatic impact on localization of delivery was evident when the next infusion was performed with a microneedle embedded to approximately 400 μm using the dimensioning wafer. An image of the microneedle is shown in Figure 68.

The 400 μm microneedle was manually inserted into a fresh porcine eye. The syringe pump was set to a Q=500 nL/min for a total of 25.5 minutes for a final delivery volume of 12.7 μL rhodamine. After the device was removed, the eye was dissected and evaluated. The sclera was measured to be ~400 um thick at injection site. Rhodamine was only observed on the scleral floor. No evidence of dye was observed on the choroid, retina or vitreous.

Figure 68**.** A 323 μm OD/10 μm ID microneedle embedded to approximately 400 μm

Figure 69 shows both delivery of rhodamine and penetration of the microneedle through the sclera. As mentioned, dye was not visible in any of the other layers of the posterior tissues.

Figure 69. Post-delivery inspection of ocular tissues showed that rhodamine was only delivered to the scleral floor for the infusion case employing a 400 μm microneedle. The thickness of the sclera at the insertion point was also measured to be about 400 μm.

Following optical imaging of the rhodamine stained sclera, the tissue sample was snap frozen and cut on the cryostat in 50 μm cross sections parallel to the plane

of insertion. From the optical image, it was assumed that most of the delivered rhodamine volume of 12.7 μL was delivered to the scleral floor. However, as shown in Figure 70, the intensity of delivered rhodamine was the greatest between 150 – 550 μm above the scleral floor and tapered off to non-detectable levels by the time the entire tissue sample had been sectioned. Figure 71 shows the corresponding confocal microscopy images and associated fluorescence intensity graphs. Note that though the actual thickness of the tissue containing the defect created by the microneedle was 400 μm, the actual tissue sample was greater due to steep thickness gradients across the sclera in the vicinity of the microneedle insertion site. The last image, approximately 750 μm from the scleral floor, shows no evidence of rhodamine infusion as it was located at some distance lateral to the site of injection.

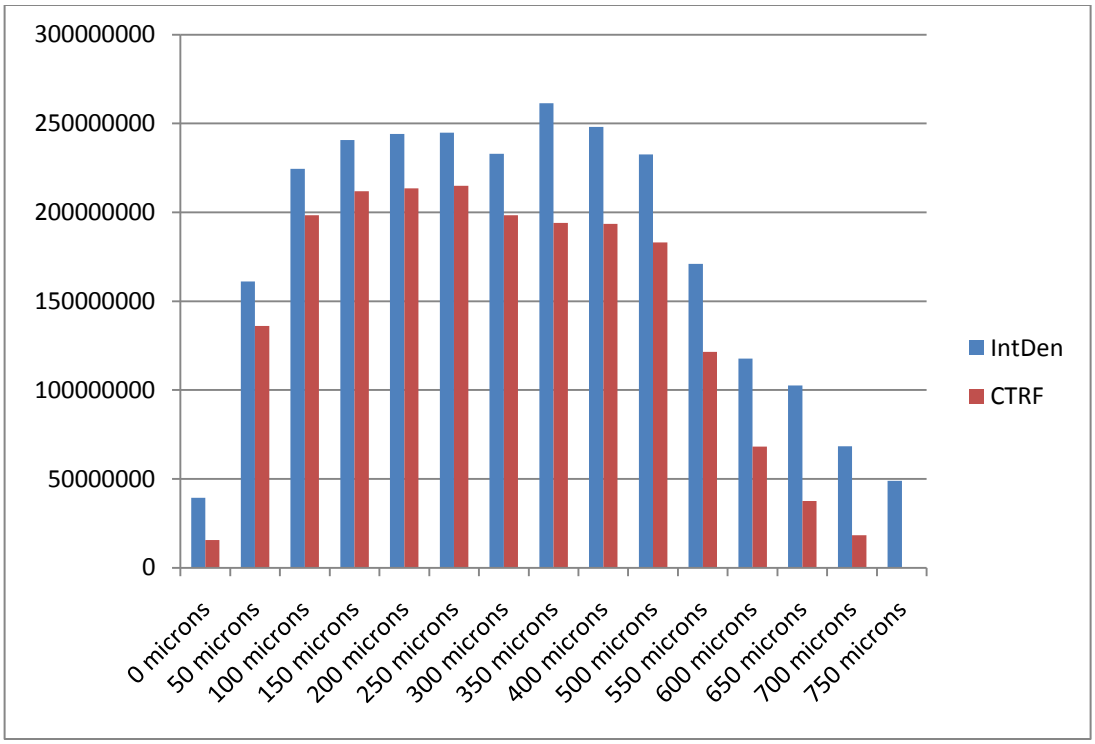

Figure 70. Corrected Total Region Fluorescence (CTRF) levels in porcine sclera with increasing distance from the scleral floor. (0 microns represents the uveal side of the sclera; 750 microns is the episcleral end).

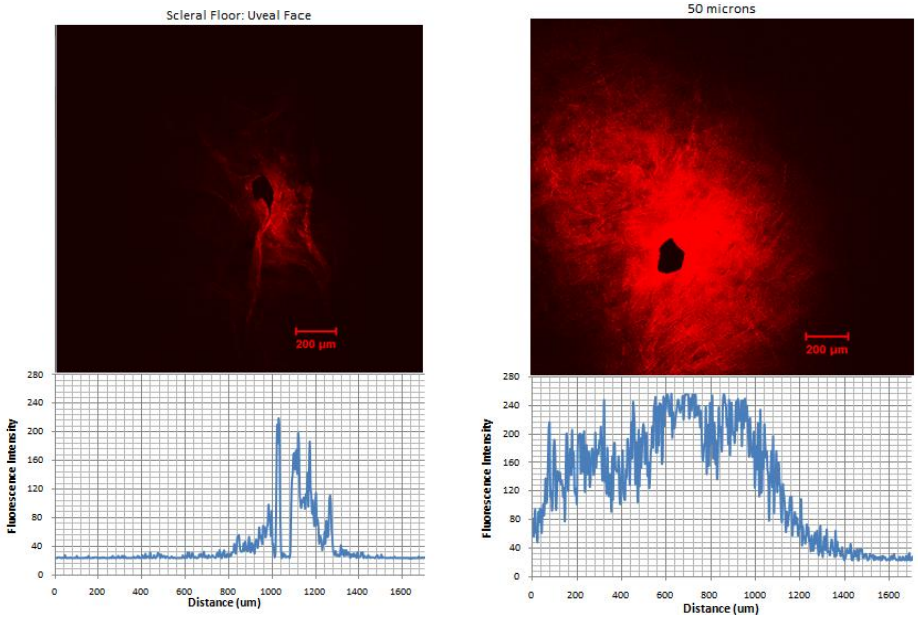

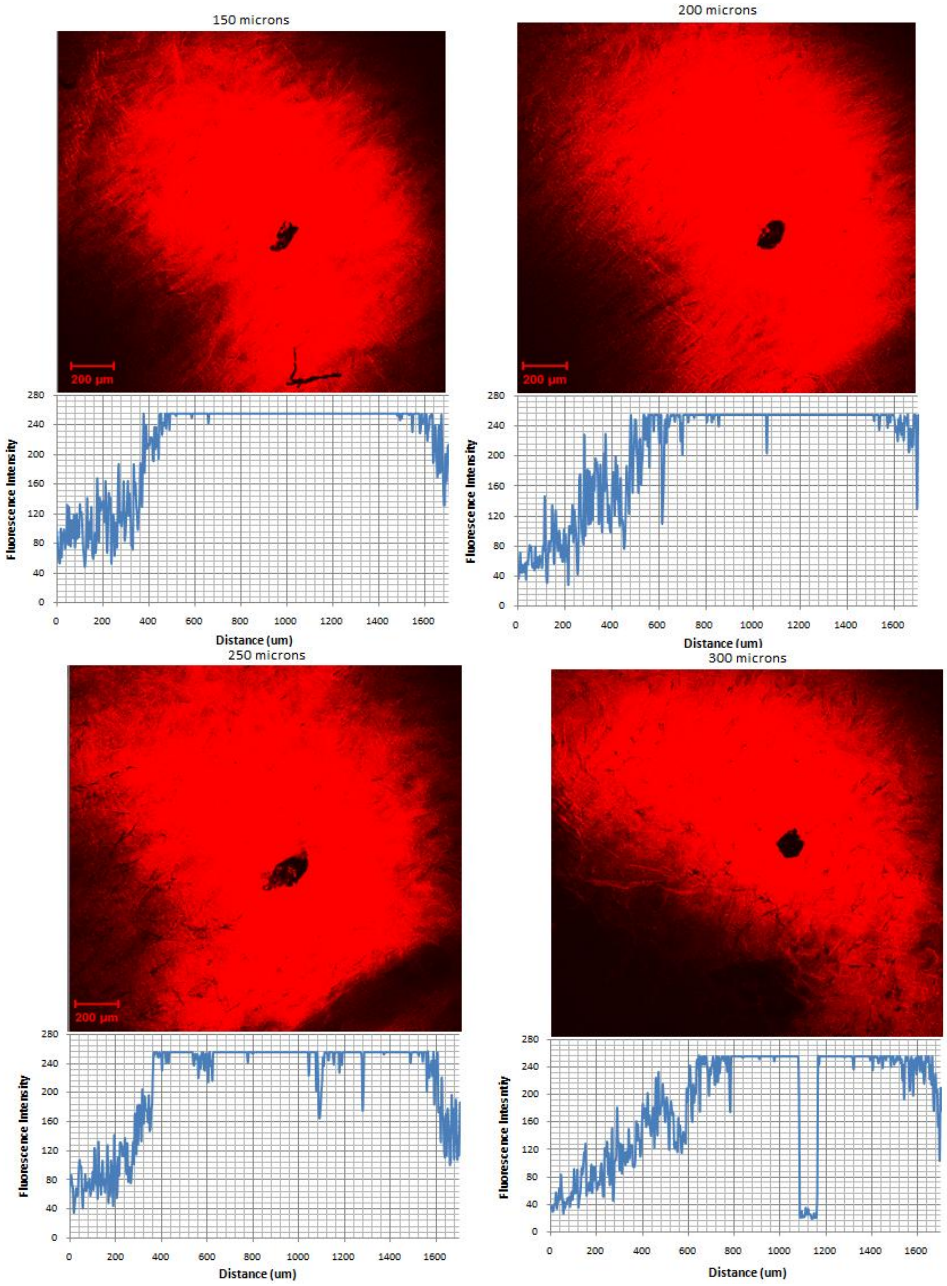
150 microns
200 µm
Fluorescence Intensity
Distance (um)
200 microns
200 µm
Fluorescence Intensity
Distance (um)
250 microns
200 µm
Fluorescence Intensity
Distance (um)
300 microns
Fluorescence Intensity
Distance (um)

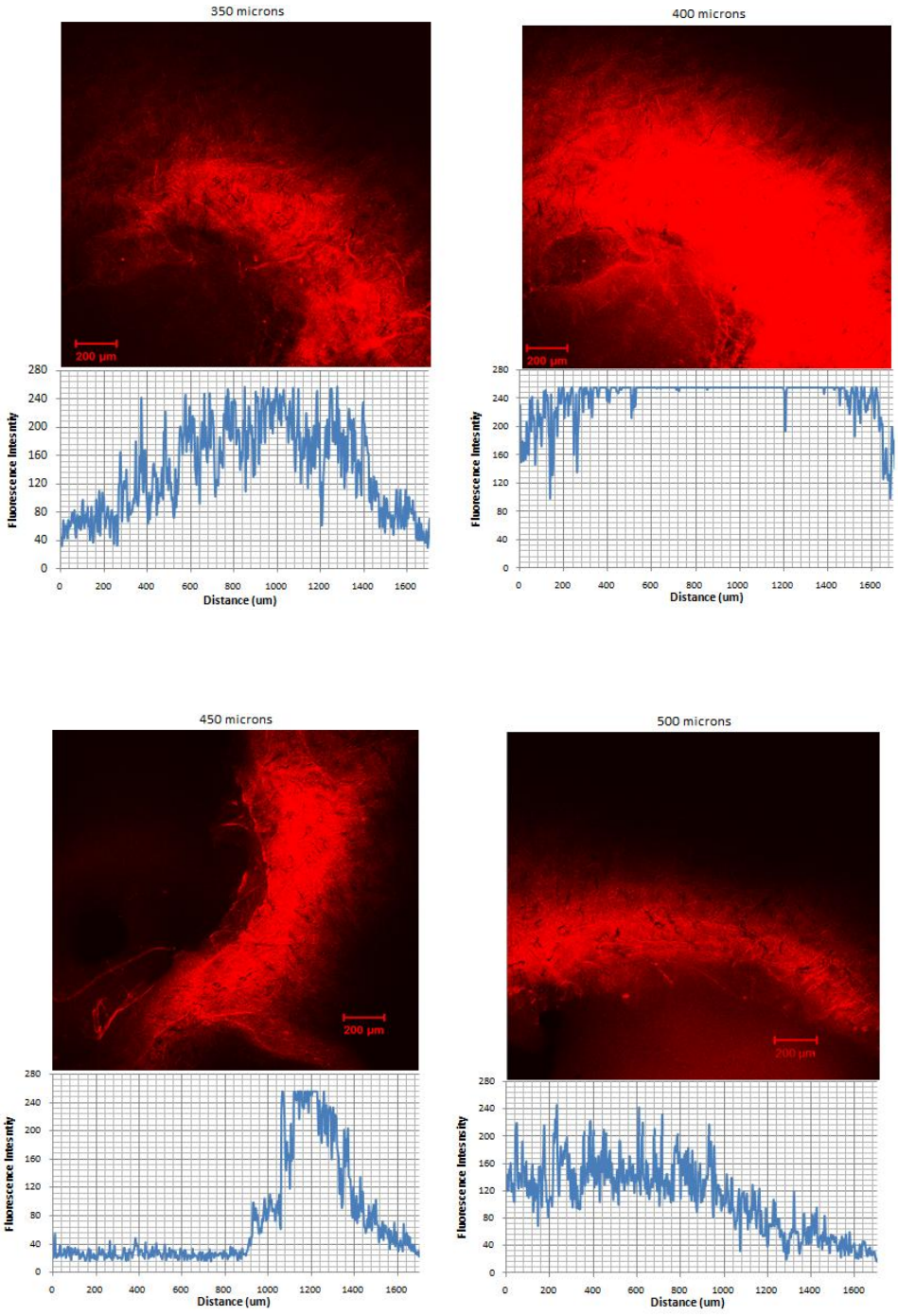
350 microns
200 µm
Fluorescence Intensity
Distance (um)
400 microns
200 µm
Fluorescence Intensity
Distance (um)
450 microns
200 µm
Fluorescence Intensity
Distance (um)
500 microns
200 µm
Fluorescence Intesisity
Distance (um)

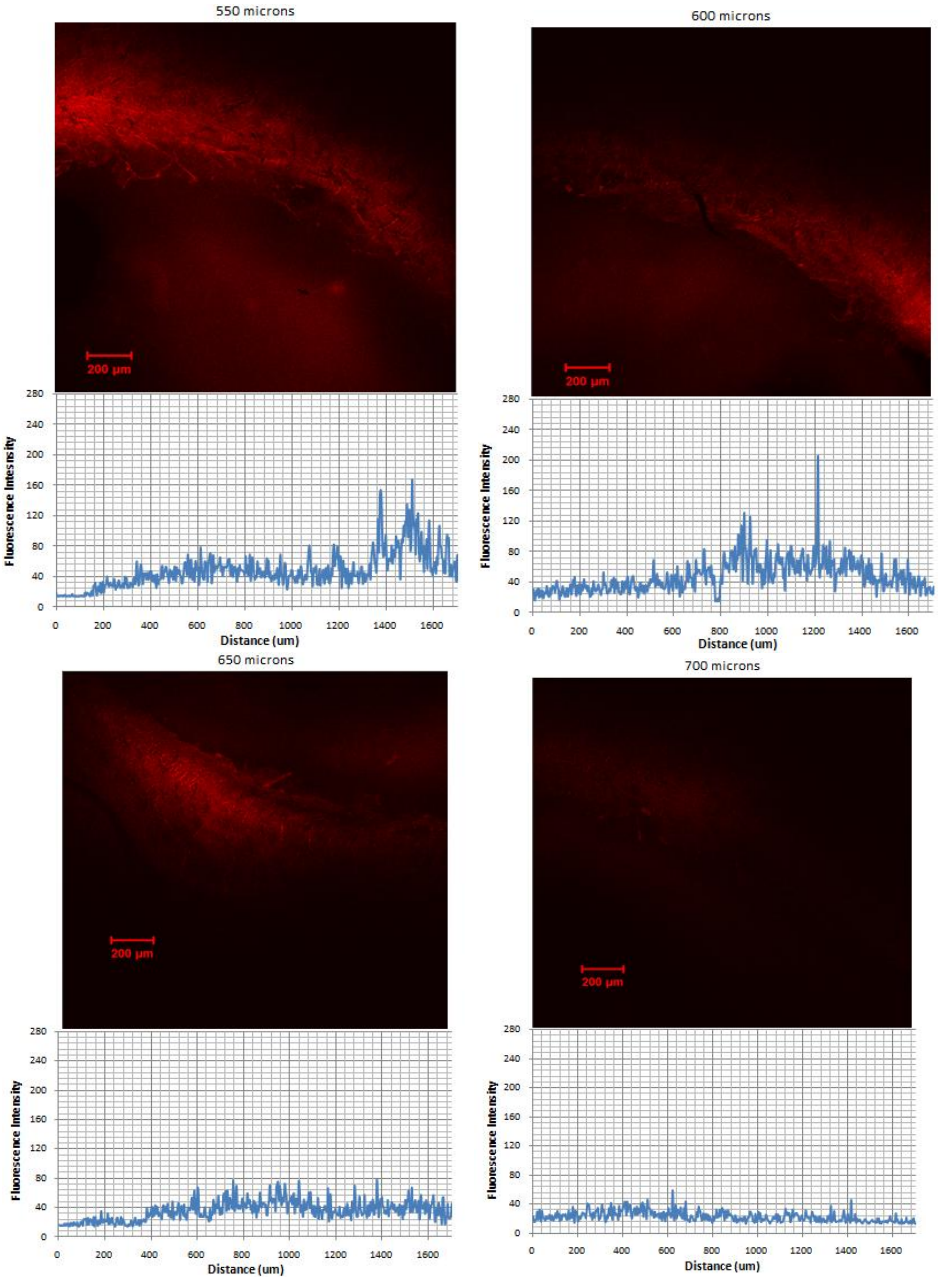
550 microns
200 µm
Fluorescence Intensity
Distance (um)
600 microns
200 µm
Fluorescence Intensity
Distance (um)
650 microns
200 µm
Fluorescence Intensity
Distance (um)
700 microns
200 µm
Fluorescence Intensity
Distance (um)

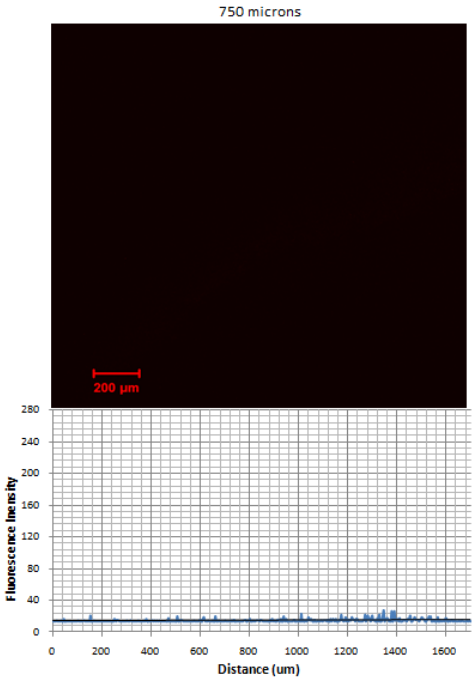

Figure 71. Porcine sclera infused with 12.7 µL rhodamine using a 400 µm long 323 µm OD/10 µm ID microneedle. Images are shown in order starting from the scleral floor at 0 microns.

The first demonstration of intrascleral and intracorneal drug delivery was reported by Jiang *et al*. 2007 [87]. Single microneedles, 500 - 700 μm in length and 200 μm X 50 μm in width, were cut from sheets of stainless steel using an infrared laser. Microneedles were dip-coated with either sulforhodamine or FITC-BSA for in vitro and histological demonstration of intrascleral delivery. The microneedle penetrated scleral sections of human cadaver sclera to a depth of 300 μm after 20 seconds of microneedle treatment. Microneedles were also dip-coated in pilocarpine, a stimulant for iris muscle contraction for glaucoma treatment, for in vivo intracorneal delivery in rabbits. A single microneedle enabled 69% bioavailability of pilocarpine in rabbits as opposed to control animals that received topical eye drops where only 1% bioavailability was observed (based on total post-delivery drug accumulation in the aqueous humour) illustrating the dramatic increase of solute delivery to intraocular tissues.

In 2009, Jiang *et al*. further demonstrated intrascleral delivery of sulforhodamine and micro/nanoparticles using a hollow glass microneedle [92]. A single glass microneedle was fabricated from a 1.5 mm OD/0.86 mm ID borosilicate cylindrical glass micropipette. The micropipette was pulled with a pipette puller to form a tapered microneedle-like structure and beveled using a pipette-specific beveled glass grinder to form the microneedle. The microneedle was extremely long, 3-4 cm, and depth of insertion into the sclera had to be manually controlled using a vertical rotary micropositioner. Microinfusion of both sulforhodamine and FITC-tagged micro- and nanoparticles was attempted on

human cadaver sclera. Approximately 10 - 35 μL of sulforhodamine was delivered intrasclerally. Microinfusion of nanoparticles was also successfully demonstrated while microparticles were unable to dispense from the orifice of the microneedle tip due to blockage related to the fibrous scleral microstructure [92]. Accordingly, co-injection of microparticles with both hyaluronidase and collagenase enabled delivery into the sclera.

Patel *et. al.* presented the third and most recent research related to microneedle-based ocular drug delivery by demonstrating suprachoroidal, the virtual space between the sclera and choroidal layers, delivery of fluorescently tagged nanoparticles in ex-vivo rabbit, pig and human globes [93]. Single glass microneedles were fabricated again using a pipette puller as described by Jiang *et. al.* [92]. Microneedles were 800 - 1000 μm tall, however depth of insertion could not be achieved by the device itself and was manually controlled using a micropositioner.

Although pipette pulled microneedles are currently the only approach to glass microneedle fabrication, there are limitations to this method to which etched microneedles improve upon. Pipette pulled structures tend to vary in quality as they are mechanically processed, and require post-pull processing such as grinding or beveling to produce an asymmetrical tip that is sufficiently sharp to penetrate tissue [135]. This grinding action would also lead to an increased chance of introducing particulates into the diminutive inner conduits causing blockages. Further, due to the nature of the process, the inner diameter of the tube decreases along the length

of the taper terminating at its smallest size at the tip orifice making the capillary tube much more prone to blockages [136, 137]. The mechanical method of pulling leads to microstructures of varying quality [135].

Finally, due to the heat and force based mechanical approach to tip pulling, the process inherently leads to structures of varying quality [135]. In contrast, microneedles fabricated using the approach developed yields 100% repeatability with respect to tip ID and tip OD due to the chemical based approach. As long as the etchant concentration, organic overlayer, etch time and capillary tubing size remain constant, a very high repeatability of microneedle dimensions and shape is attainable.

It is understood that the forces required to penetrate tissues decrease with sharper tips, i.e. needles with decreasing cone angles, that would otherwise buckle the microneedle [81]. However, microneedles that were chemically etched were able to penetrate the globe without buckling and that the supporting backing provided the necessary "penetration stop" to ensure the microneedle embedded to a fixed distance within the tissues. The resultant geometry observed on the etched structures allowed microneedles to withstand handling, insertion and removal forces due to the wider base than pipette pulled tips which have extremely low cone angles and very long taper lengths.

It was also observed that the longer tapered microneedles from pipette pulled microneedles failed earlier due to shear loading upon insertion while the etched microneedles did not. While the average force required for interfacial bond failure

did not actually fracture the tubing (but delaminated the tubing from the PDMS), it is expected that lower shear stresses on the taller, tapered structures would be tolerated due to the width of the structure and is critically dependent on the slenderness ratio (a ratio used in compression members to define the equivalent length of the microneedle to the radius of gyration of the structure). Furthermore, the etching process naturally self-terminates at a single sharp point and does not require any post-processing steps except for neutralization of HF in a saturated bicarbonate solution after which the microneedles are ready for integration and delivery.

7.8. Intrascleral delivery of BSA

A final experiment was performed to deliver FITC-BSA, a model protein based drug, using a 323 μm OD/10 μm tip 1.1 mm tall microneedle. The device was inserted into a fresh porcine globe and connected to a syringe pump using a delivery rate of Q = 500 nL/min.

A total of 20 – 25 μL of dye was delivered during the experiment. Figure 72 and Figure 73 show the confocal and light microcopy images taken at the injection site. Though penetration, intrascleral and transscleral delivery was confirmed, delivery to the internal membranes upon post-infusion dissection was difficult to confirm due to the absence of color in the FITC-BSA solution.

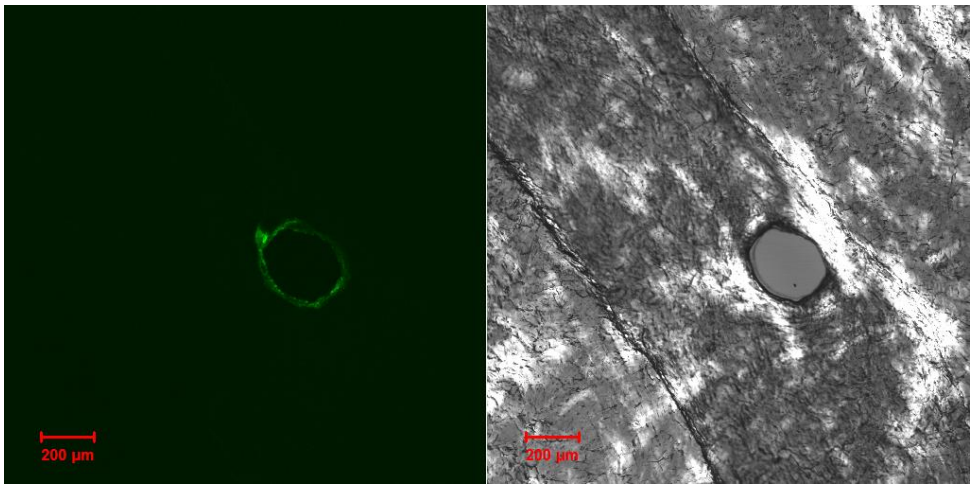

Figure 72. Cross sectional section through insertion point showing a 250 µm diameter orifice through the sclera with BSA visible at the circumference of the orifice.

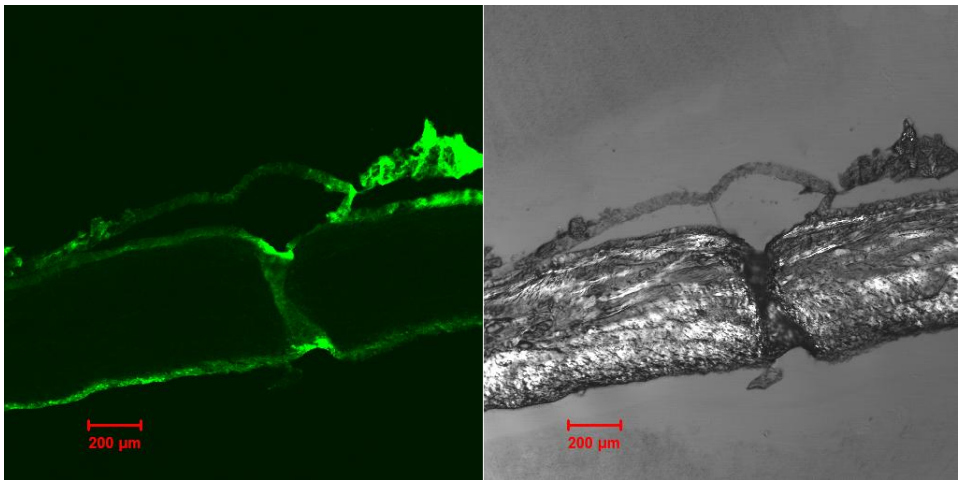

Figure 73. Images taken from the same scleral section showing delivery of FITC-BSA

The FITC-BSA was used as a more realistic model of an actual protein/aptamer based drug that would be used for treatment of a particular pathological disease.

Chapter 8 Interfacial Bond Strength Characterization

The strength of the interfacial PDMS/glass bond between the capillary tubing and the underlying PDMS substrate was characterized as delamination of the microneedle from the substrate was identified as a potential mode of failure during device insertion or removal from the ocular surface. Due to the widespread use of PDMS in microfluidics and biomedical microdevices, its bonding strength to other substrates, and especially PDMS itself, has been well characterized using plasma oxidization, heat, pressure, and chemical bonding. The most commonly used approach, air or oxygen plasma treatment has been widely used and characterized due to its practicality and irreversible bonding outcomes. The bond formation is established through generation of reactive radical species of surface silanol (Si–OH) groups on the PDMS surface that, in close conformal contact to another planar PDMS surface can form Si–O–Si covalent bonds [118]. However, this approach proved unfeasible for embedding cylindrical glass structures into cured and micropatterned PDMS substrates as conformal contact between the microchannel and the tubing surface was not achievable due to the lack of chemical reaction to form the covalent linkage required for bonding.

Furthermore, as the device fabrication procedure that was the most suitable during active delivery into the eye evolved to retain the native polyimide coating on the capillary tubing, oxygen plasma activation was no longer relevant. As such, an alternative bonding method using uncured PDMS prepolymer, mixed at several different base:curing agent ratios, was characterized as discussed below.

Tensile samples were made and tested using the method described. Based on the results of the tensile tests, the 3:1 ratio possessed the strongest bond among those tested, Figure 74. As expected, the 30:1 failed at a much lower threshold due to the low proportion of cross-linking compounds resulting in compromised bond strength. The average failure stress for the 3:1 ratio was significantly stronger than the typically recommended base:curing agent ratio of 10:1. Interestingly, when adding 0.85 g fumed silica to the 10:1 compound, the bond strength was also significantly higher than that of the standard case but not as strong as the 3:1 combination. As such, the 3:1 ratio was selected as the method of bonding for the microneedle to the PDMS substrate.

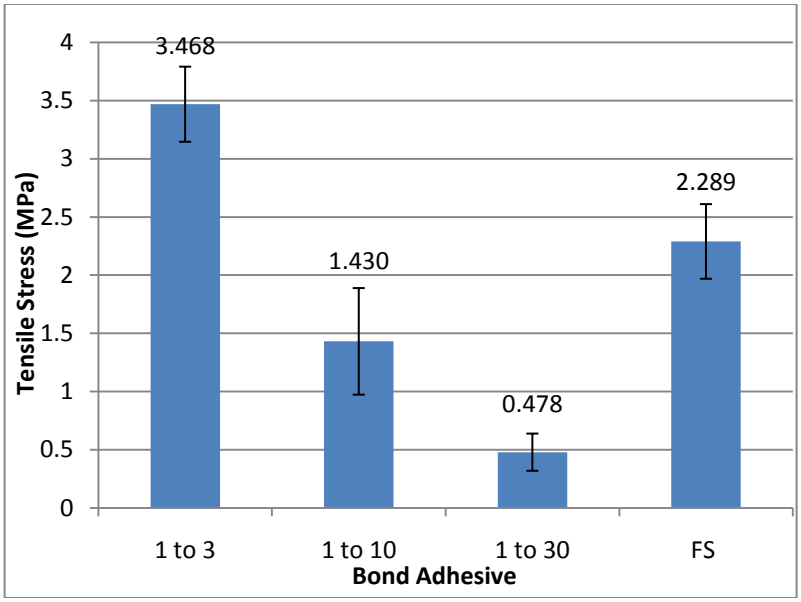

Figure 74. Average failure stress under tensile loading for the interfacial bond between 363 μm OD polyimide coated tubing and 10:1 PDMS for four different bonding adhesives: PDMS at ratios of 10:1, 3:1 and 30:1 base:curing agent and 10:1 PDMS with 0.085 wt% fumed silica

The average tensile force required to break the bond between the polyimide tubing and the PDMS using the strongest adhesive, the 1:3 ratio of PDMS adhesive, was 12.4 $\pm$ 4 N. Though the actual forces required to insert the microneedle were not measured, other work has shown that microneedles can insert into the epidermis in vitro using a manual force of approximately 10 N without microneedle breakage [61].

The 1:3 PDMS ratio adhesive was then used to test the interfacial bond when subjected to only shear loading to determine failure under expected shear stresses that the device would encounter during lateral forces that would induce bending moments during insertion into the eye [114]. Tubing with the native polyimide coating withstood slightly greater shear loading at the interface between the tubing and the PDMS than the bare silica case as shown in Table 8 for N=3 experiments.

Table 8. Failure Shear Stress for Tubing/PDMS Interface

Shear Force Required to Dislodge Tubing from Microchannel (N)	Stripped Bare Tubing	Polyimide Coated Tubing
Sample 1	1.307	1.963
Sample 2	1.253	1.793
Sample 3	1.29	1.481
Average	1.283	1.746
Std. Deviation (N)	0.028	0.200
Tubing OD Diameter (mm)	0.325	0.363
Bond Length (mm)	15	15
Bond Area (mm^2)	15.3	17.2
σ_{shear} (MPa)	0.0838	0.1015

Chapter 9 Durability Study

To assess the durability of the devices, a set of tests were conducted whereby a device was repeatedly inserted and removed from a whole porcine globe until a failure occurred. A failure was defined as one of four events:

(i) fracture at the tapered tip portion of the microneedle

(ii) fracture along the unembedded microneedle shaft

(iii) tubing delamination from the microchannel

(iv) tubing fracture within the embedded PDMS matrix

Table 9 reports the outcomes of the insertion/removal tests. For the set of four independent tests performed, no failures at the microneedle tip or shaft were observed. In each of the tests failure occurred either via delamination and/or fracture of the embedded tubing within the PDMS microchannel. This observation is consistent with the results of the shear and tensile tests which showed that the microneedles failed at much lower shear loading stresses than in tensile loading, i.e., embedded tubings are more likely fail due to fracture at either the interface or through delamination within the PDMS microchannel. In contrast, tensile stresses at the interface required for delamination were higher which is consistent with the observation that 10 insertion/removal cycles were required before the tubing became delaminated from the surrounding PDMS matrix. It is concluded that the microneedle tips are sufficiently strong to withstand insertion/removal forces and that the failure is currently restricted by the strength of the interfacial bond between both the bare glaass and PDMS and the polyimide coating and PDMS.

Overall, devices tested in this study were sufficiently strong to withstand insertion/removal forces for the single-use format for which they were intended. As such, the devices as designed are capable of both inserting into an ex-vivo porcine eye without failure and being removed without delamination or breakage for a single-use application.

Table 9. Outcomes of single embedded 323 μm microneedle durability tests in whole porcine globes

Microneedle Sample/Length	**Mode of Failure**	**Number of Insertions/ Removal till Failure**	**Comments**	**Figure Number showing Image**
A/1.3 mm	iii	10	Microneedle displaced into the PDMS microchannel on the 10th insertion; no visible damage to the microneedle tip	Figure 75
B/1.0 mm	iii,iv	6	Tubing fracture occurred within the PDMS microchannel after dislocation into the microchannel	Figure 76
C/630	iii,iv	4	Tubing fracture occurred within the PDMS microchannel; microneedle remained embedded in the eye	Figure 77
D/700	iii,iv	6	Tubing fracture occurred within the PDMS microchannel; tubing further dislocated from the microchannel	Figure 78

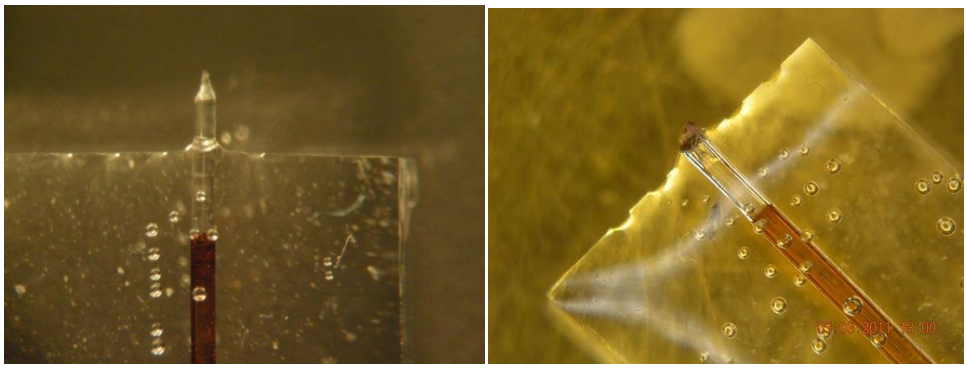

Figure 75. Microneedle A: before and after images after 10 attempts of insertion and removal into a whole porcine globe

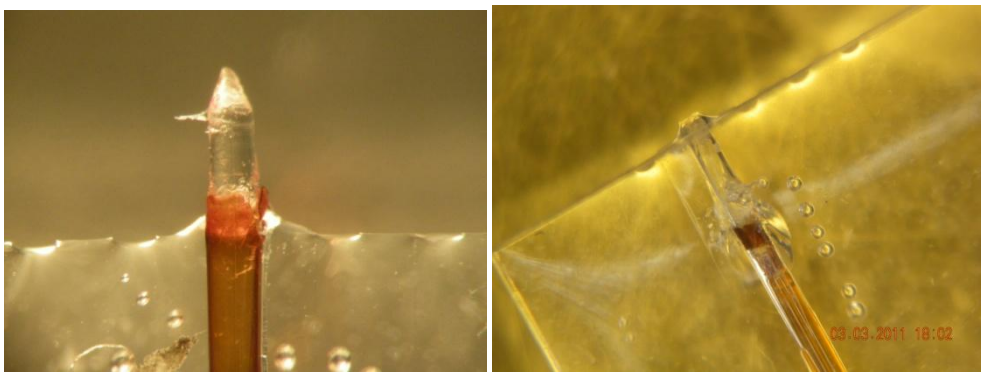

Figure 76. Microneedle B: before and after images after 6 attempts of insertion and removal into a whole porcine globe

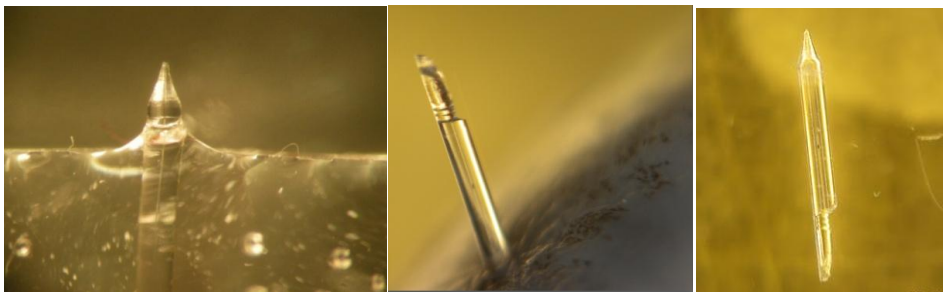

Figure 77. Microneedle C: before and after images after 6 attempts of insertion and removal into a whole porcine globe

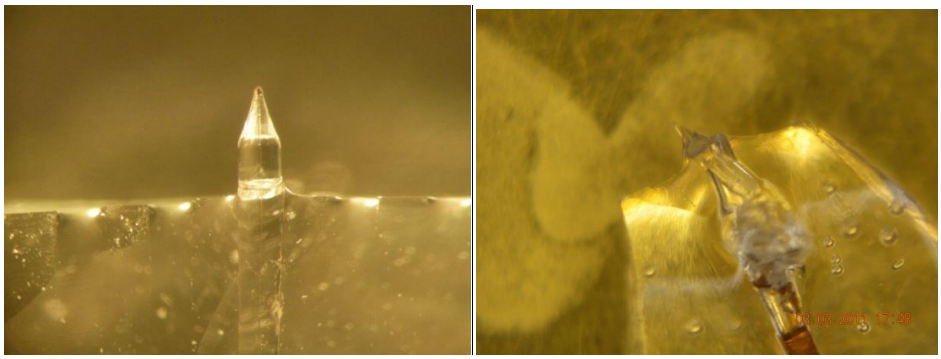

Figure 78. Microneedle D: before and after images after 6 attempts of insertion and removal into a whole porcine globe

Chapter 10 Microneedle Arrays: Fabrication, Integration and Application

10.1. Etching of Microneedle Arrays

After a repeatable process to produce a single hollow microneedle had been developed, a low-cost method of fabricating arrays of microneedles was developed based to mimic the "batch processed" nature of conventionally microfabricated microneedle arrays. Having a rapid throughput fabrication approach enabled high numbers of microneedles to be etched at a time for further processing and integration into the final device. Only the smaller 150 μm capillary tubing could be batch processed due to its very low bending radius which enabled the flexibility required for array etching. Figure 79 shows the resultant 126 μm array of 15 microneedles formed during the one-hour etch.

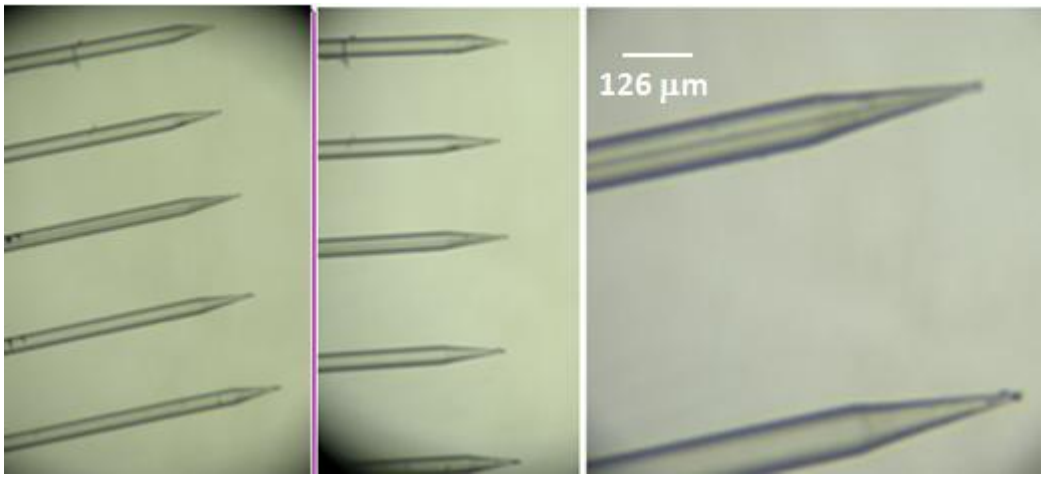

Figure 79. Resultant 126 μm OD/10 μm ID microneedles fabricated using the described process

Repeats of the etch process resulted in an approximately 80% success rate of fabricating similar microneedles of 126 μm OD/10 μm ID tip and a taper length of three times the tubing OD as was observed during the single capillary tubing etches. As observed in the fabrication of single microneedles, the mean tip ID of 10 μm and OD of 126 μm were conserved across each of the 34 samples measured with no variation, Figure 80. The mean taper length was 369 μm ± 54 μm which was significantly longer than microneedles etched individually. This was attributed to the interference of neighboring meniscuses during the array etch process. The mean cone angle was 18.3° ± 2°, smaller than individually made microneedles, and consistent with the longer taper lengths observed which have associated sharper tips (smaller angles).

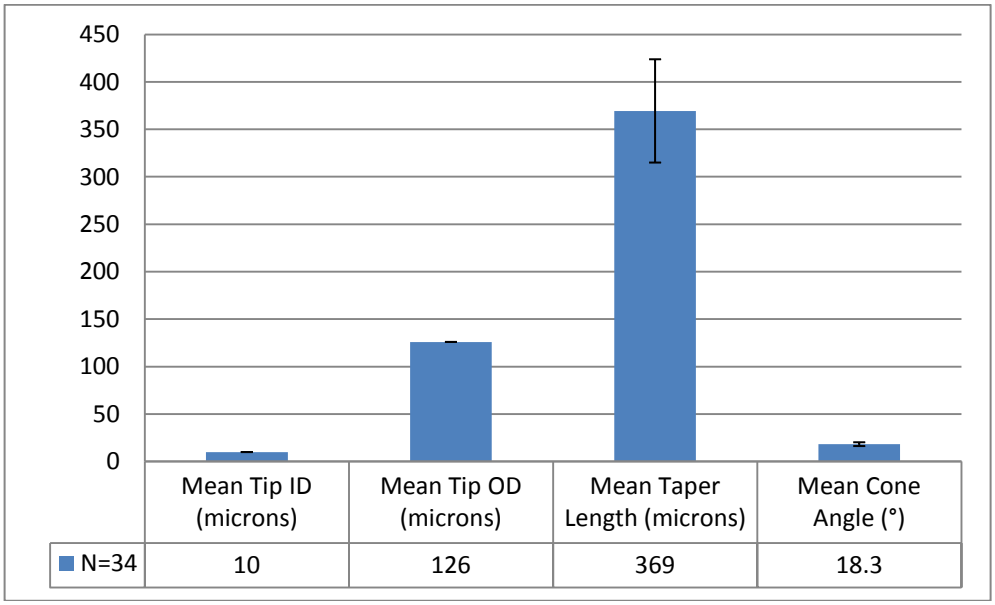

Figure 80. Mean tip ID, tip Base OD, taper length and cone angle for microneedles fabricated from 126 μm OD/10 μm ID capillary tubing using array based fabrication.

10.2. Integration of Array-Etched Microneedles

Microneedles were embedded to form one-dimensional linear arrays with two, three and five microneedles as shown in

Figure 81. Due to the small volumetric dosing capacity of a single microneedle, certain applications may require higher delivery rates. As such, additional microneedles may be easily incorporated into the particular design based on a required dosing regimen.

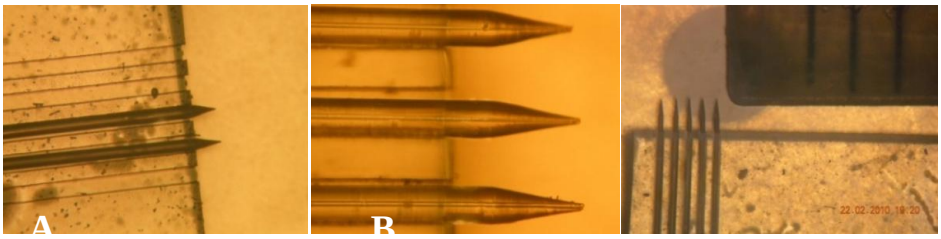

Figure 81. Construction of one-dimensional linear arrays of two 323 μm OD microneedles (A) three 323 μm microneedles (B) and five 126 μm OD microneedles (C) using the methods described.

Figure 82 shows how microneedles are easily aligned in-plane to form a linear array of uniform height. In this particular series, after microneedles are rolled into their alignment grooves (I), microneedles are adjusted using a planar, stainless steel plate to push the microneedles to more equivalent lengths (II) and then further adjusted to set all the microneedles with the range of the target height (III) and then finally set to a particular height (IV) - in this case 450 μm. After the microneedles were set to their target height, the assembly was moved to a hotplate and permanently bonded as described. Microneedles are held in

place with sufficient strength by the interference-fit between the microneedles and the microchannel and do not shift during transport to the hotplate. Figure 83 shows the linear array after bonding the microneedles in place.

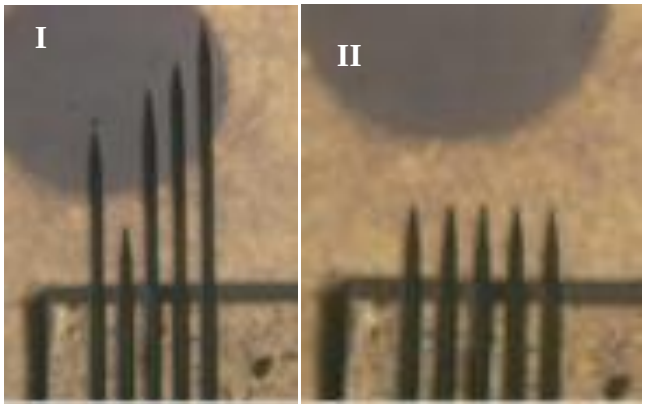

Figure 82. Series of images showing how microneedles are aligned using a flat stainless steel panel and a microscope. Once tubing sections containing the sharpened tips are rolled into their grooves (I) the lengths are adjusted for equivalency by pushing the needles back to set the target length (II). In these images, 5 X 126 μm OD microneedles are shown at a length of approximately 450 μm.

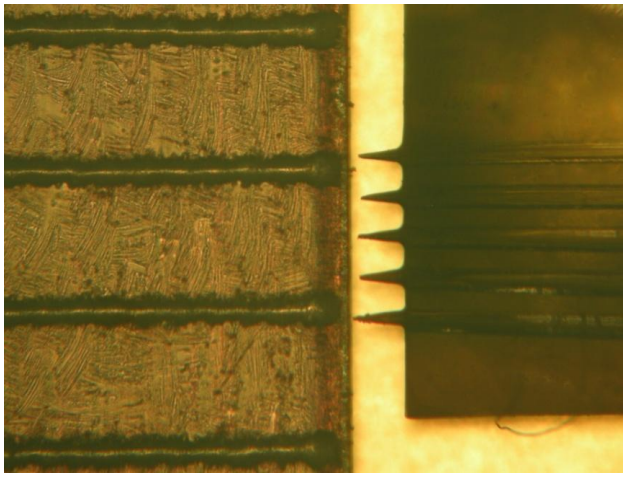

Figure 83. Five-microneedle linear array after embedding shown next to mm-scale markers

Figure 84 shows SEM images of the same 5 microneedle device. During embedding, PDMS flows into the microchannels securing the tubing into place. The images show minor incomplete filling of the microchannels. However, microneedles are still strongly bonded to the PDMS substrate.

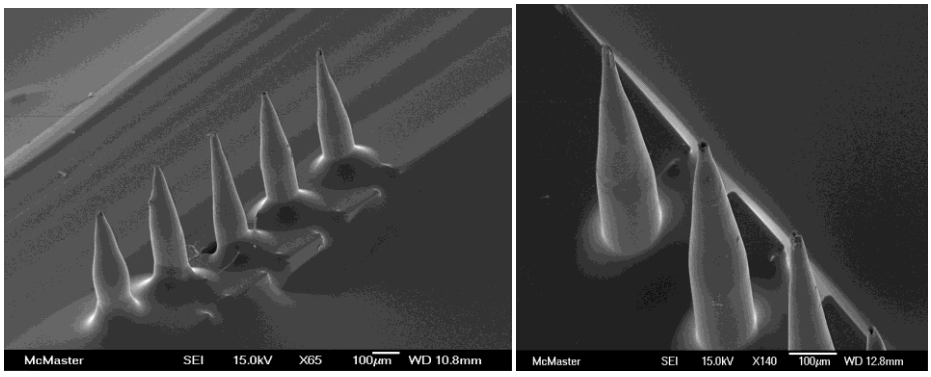

Figure 84. SEM images of a 5 X 126 μm OD/ 10 μm ID microneedle array

Figure 85 shows the relative size of two 126 μm microneedles embedded into PDMS next to a dime and also next to a standard 30-gauge needle commonly used for intravitreal injection. From this juxtaposition, microneedles are a less invasive route for delivery of compounds, not only to the intravitreal space, but to any tissue layer with the eye. Moreover, the most notable difference between the two needles would be the ID. The ID for the 30 Gauge needle is 140 μm which is consistent for delivery of the sizable 60 μL depot of drug injected intravitreally every 6-8 wks. However, the ID in the microneedles is only 10 μm and is on-scale for delivery at lower and more controlled rates over prolonged durations. Moreover, the depth of insertion is much more controllable and on-scale with the microscale dimensions of the various tissues of the eye. While the larger needle penetrates several centimetres

into the eye and delivers a single dose that is rapidly cleared by the ordinary dynamic aqueous and vitreous flow pathways in the eye, the microneedle penetrates only micrometers deep and can actually take advantage of the various ocular tissues as rate-controlling membranes to control the release of solute over longer durations at a specified tissue target at rates that are therapeutically useful.

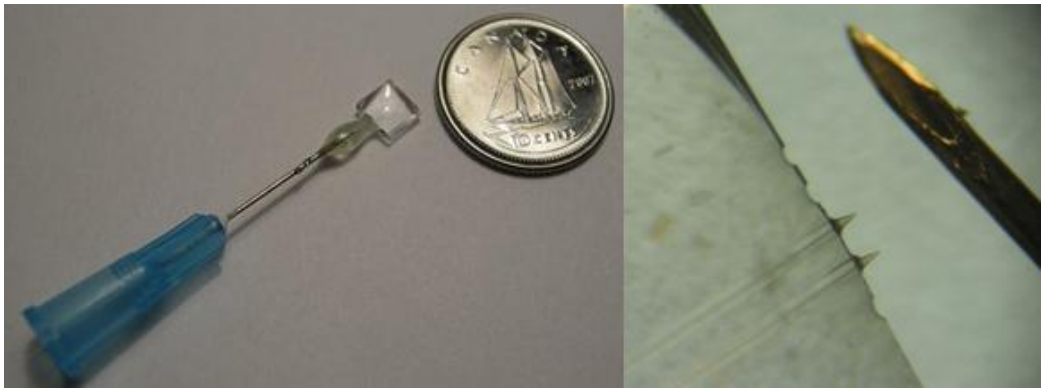

Figure 85. Size comparison of 2 X 126 μm OD/10 μm ID microneedles embedded into micropatterned PDMS substrates. Microneedles are shown next to a 30 Gauge stainless steel needle (305 μm OD X 140 μm ID) currently used for intravitreal injections

After testing a single microneedle, an array of five 123 μm microneedles was inserted into excised bovine sclera, Figure 86. Again, the microneedles were able to be inserted and remain within the tissues even under body forces when inverted.

Figure 86. Insertion and retention of an array of 5 X 126 μm OD 500 μm tall microneedles

10.3. Variation using Electroosmotic Pumping

This section presents an improved method of batch fabrication of hollow microneedle arrays for drug delivery. The previous sections presented a multi-step method of device integration wherein microneedles were first fabricated, using either a single-mode or array method, and then subsequently embedded into micropatterned substrates. The objective in this section was to develop a one-step method whereby microneedles could be etched and immediately used in their intended application by using an electric field to pump water in microchannels – a convenient option for fluid actuation when designing microscale systems.

As discussed earlier, microneedles were fabricated using the isobaric pumping of water through the inner capillary tubing bores to prevent surface tension mediated influx of acid etchant so that inner diameters equivalent to the

native dimensions of the manufacturer's specifications could be generated. The formation of sharp tips was a result of the dynamic positional change of the interfacial meniscus between the organic overlayer and the acid etchant due to the reduction of the diameter of the glass fiber being etched as the water was pumped through. The approach however required tubing lengths of 10 cm and multiple processing and handling steps for subsequent device integration.

Figure 87 (A) illustrates the method previously used for microneedle fabrication from capillary tubings.

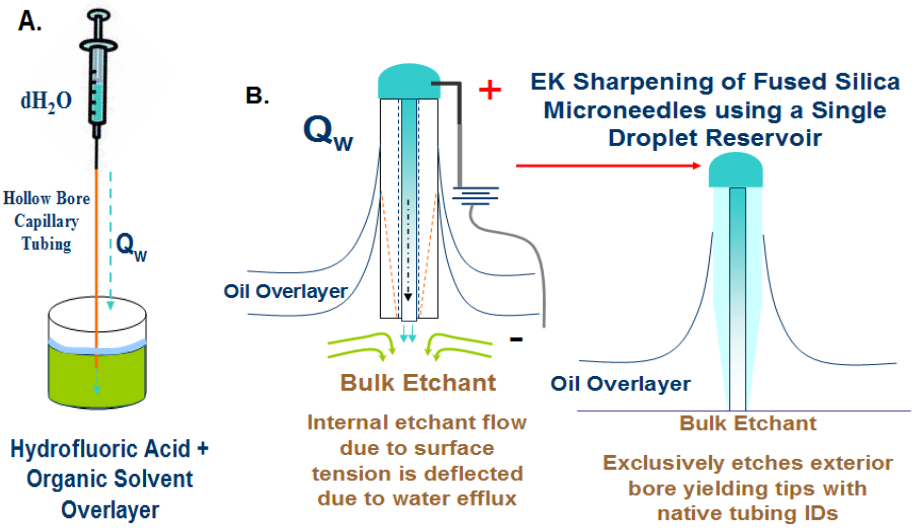

Figure 87. Schematic of the principle behind microneedle fabrication using pressure driven (A) and single droplet electroosmotic actuated flow (B) of water efflux through the inner bore of the capillary tubing to prevent internal etchant rise

Figure 87 (B) also shows the process whereby a single droplet can be used as a reservoir from which water can be pumped through a capillary using electroosmotic forces at an applied voltage between the droplet reservoir and the acid etchant.

Figure 88 (A) shows a post-etch image of the resultant array of microneedles embedded into the underlying PDMS substrate immediately after retrieval from the hydrofluoric acid. As the capillary tubings are not permanently fixed during the etching process, they can be repositioned and aligned as shown in Figure 88(B). Figure 89 (A) shows a side-angle view of the array after alignment. The dimensions of the microneedles formed in the etch are shown in Figure 89 (B).

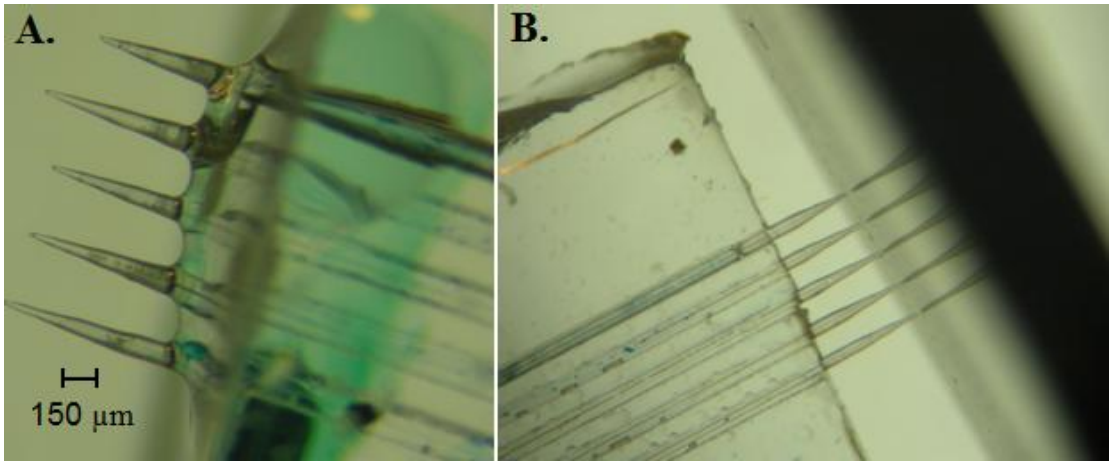

Figure 88. Post-etch optical image (A) showing the resultant array of etched microneedles within the PDMS substrate. Capillary tubings are not fixed during the etching process and can hence be easily positioned (B) for precise planar alignment after etching.

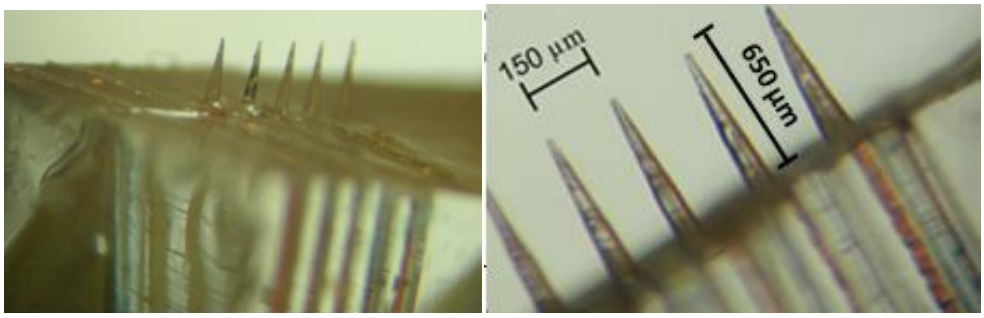

Figure 89. Post-alignment optical image (A) of microneedles at an interneedle pitch of 150 µm. Top view (B) of linear array showing precision spacing of the microneedles embedded in the PDMS matrix – device is ready to be used within a drug delivery setup.

As expected, the mean tip ID and tip base OD were conserved and were equivalent to the native dimensions of the tubing. However, the mean taper length of 634 µm $\pm$ 64 µm was significantly longer than equivalently sized microneedles etched using pressure driven pumping while the mean cone angle was reduced to 14.8 µm, Figure 90. This increase in taper length was attributed to the closely arranged microneedles in the PDMS substrate as the tubing in the pressure driven pumped configuration were spaced at a distance of 363 µm apart while the capillary tubing in the substrates for electrokinetic etching are 150 µm apart. This phenomenon of increased taper lengths and reduced cone angle with decreasing interneedle spacings during the etch process has previously been observed. By employing a parallel-etching approach, cone angles in the range of 7° - 22° were achievable using v-shaped microgrooves at precise spacings etched using KOH in silicon [131]. Reducing the gap distance in conjunction with the number of fibers simultaneously etched resulted in an increase in meniscus height with an associated lengthening of the taper and reduction of tip

angle [131]. The observed increase in taper length and reduction in cone angle of the electrokinetically etched microneedles as a result of gap distance reduction when compared with pressure-driven array fabricated microneedles is consistent.

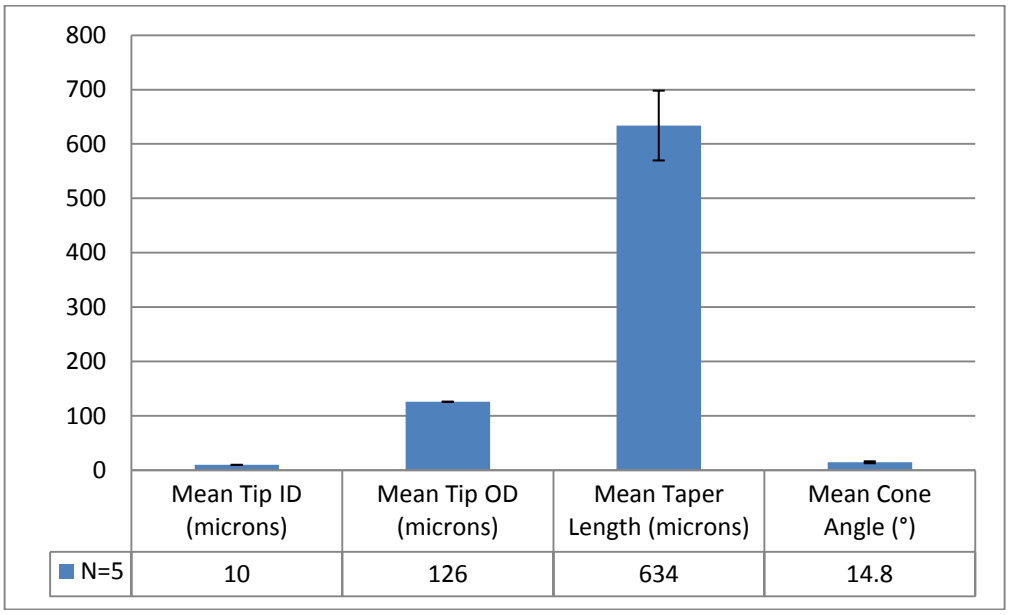

Figure 90. Mean tip ID, tip base OD, taper length and cone angle for microneedles fabricated from 126 μm OD/10 μm ID capillary tubing using an electrokinetic method of array based fabrication.

The approach discussed in this section offers several advantages over pressure-driven fabrication in that the tubing/substrate assembly and microneedle may be fabricated in a one-step simplified process using electroosmotic pumping. When water is in contact with silica, adsorption equilibrium at the glass/water interface results in ionization of SiOH groups on the glass surface producing negatively charged SiO^- on the surface of the glass. This accumulation of charge attracts H^+ groups from the water to migrate towards the layer of negative charge

termed the electrical double layer [138]. When this charge separation is placed in an electric field, the positive ions move towards the electrode of opposing charges due to electrostatic forces. As a result, flow in the rest of the microchannel is initiated due to transfer of viscous drag effects into bulk flow. Employing this phenomenon allows for reduction of consumption of expensive capillary tubing due to the minimized lengths required for device construction using this approach.

Chapter 11 Conclusions/Future Work

While the eye has efficient anatomic and physiological protective barriers these barriers also provide equally excellent barriers to solute transport to the intraocular tissues. Diseases of the posterior eye encompass pathologies of the posterior sclera, uveal tract, vitreous, choroid, retina and optic nerve head – all of which have responded positively to new classes of emerging pharmacotherapies as comprehension of ocular disease progression improves, as better and more sensitive diagnostic techniques are developed and as more drug discovery efforts aimed towards antiangiogenic compounds and neuroprotectants are pursued [34]. Microneedle based delivery offers a minimally invasive approach for site-specific ocular delivery - after depositing depots of drug within the sclera, drugs may diffuse to surrounding tissues for therapeutic relief.

There are three major tissue barriers for the non-corneal pathway of absorption: (1) the conjunctiva which is composed of tight epithelial junctions of multilayer cells, (2) the proteoglycan/collagen matrix of the sclera and (3) the retinal pigment epithelium (RPE)-choroidal layer comprised of tight epithelial junctions of monolayer cells [13, 17]. The presence and prevalence of these tight junctions serve to diminish solute flux of even the smallest hydrophilic compounds in both the conjunctival and RPE layers [34]. Differential diffusion profiles have been observed based on a particular drug compound's lipophilicity: for hydrophobic drugs it was found that the RPE-choroid layer is the rate-limiting barrier, while for hydrophilic drugs, the conjunctiva was more restrictive to large,

polar compounds [14, 133, 139-141]. Microneedles offer a way to circumvent these drug specific variations by directing drugs to non rate-limiting tissue layers based on the particular drug's physicochemical properties.

Furthermore, if penetration of drugs across the conjunctival epithelium and the RPE can be improved, drugs can reach their intended site of action. For example, though the sclera is permeable to macromolecules up to 70 kDa, the choroidal blood flow pathway and the retinal pigment epithelial cell layer in the neural layer are major barriers to drug penetration as it is widely known that the choroid is the most vascularized tissue of the eye and as such, choroidal blood flow and choriocapillaris fenestrations can lead to the rapid removal of compounds diffusing through the sclera [21, 34, 142]. As the choroid is perfused with these choriocapillary vessels – which form a tightly packed network with a surface area equivalent to twice the choroid area - a method of bypassing this region will assist in achieving constant concentration gradients by avoiding these outflow pathways altogether[34]. Based on the precision of clinical scleral thickness measurement instruments, such as ultrasound biomicroscopy, microneedles could be set to a defined length to cross these barriers and deposit drugs at the specific pathological site within the eye. More specifically, if a microneedle could be set to a specific length, based on each individual patient's ocular measurements, choroid-mediated clearance could be significantly reduced if not altogether avoided.

From a systemic delivery perspective, the permeation of drugs to the posterior segment is restricted by the blood retinal barrier which consists of both

an outer barrier comprised of the retinal pigment epithelial layer (RPE) and an inner layer which consists of the endothelium of the retinal vessels [34]. For drugs to penetrate these barriers, a drug compound should be specifically synthesized to possess appropriate membrane partitioning characteristics through diffusion driven transport or the drug should present on either the cell surface receptors of the RPE cells or the retinal blood vessel surface for carrier-protein mediated active transport [34]. Microneedles offer an accurate method of directing individual drugs to tissues containing cells expressing their specific cognate receptor. Coupling controlled release mechanisms with specific drug targeting to different cells in the barrier layers that may express different carrier proteins (e.g. amino acid transporters, peptide transporters, monocarboxylic acid transporters, nucleoside transporters, organic cation transporters and efflux systems) significantly enhances the probability of efficient drug penetration directly to the intended diseased tissue [34]. 30% of commercial drugs target carrier proteins so any device that can dispense and delivery drugs close to these tissue barriers that possess these transporters will hold promise to delivery drugs to these anatomically privileged sites in order to enhance ocular bioavailability [34]. Microneedles can achieve this and further dose at any specified rate.

Furthermore, many drugs may be eliminated posteriorly through the blood retina barrier to the main systemic circulation [27]. Considering that these drugs could be actively delivered through the microneedles in a sustained, controlled and prolonged manner, repeated interventions could be diminished if not altogether

eliminated. Essentially, increasing the drug bioavailability by bypassing a particular drug's barrier will help achieve successful posterior penetration.

The work in this thesis describes a new method of directing delivery of solutes at fixed rates into intraocular tissues using microneedle-based devices that can be controlled for needle lengths. Microneedles can not only direct drugs to the appropriate tissues, they can also bypass regions of limited permeability. As an example, the sclera is a well-known diffusion barrier to molecules larger than 70 kDa; however collagen fibrils which span the eye in parallel bandings underneath the episcleral region have more open aqueous spaces when compared with the proteoglycan composition of the outer matrix providing lower resistance pathways to enhance diffusion driven transport [34]. If microneedle lengths could be adjusted to deliver drugs directly to this layer, difficulties crossing the outer matrix would be removed.

Commercially, the pursuit of new methods to better deliver existing drugs to pathological sites offers a better investment than simply developing new pharmaceuticals as the cost of new drug development - from bench to market - is estimated to be at least $150 million [7]. This provides an incentive to improve on actual delivery vectors for these existing pharmacotherapies that currently show demonstrated attenuation of disease processes in the eye.

Currently, the two most widely prescribed drugs for wet AMD include Macugen® (Pfizer Inc., NY, NY) and Lucentis® (Genentech Inc., San Francisco, CA) while off-label prescription of the anti-cancer drug Avastin® (Genentech, Inc.,

San Francisco, CA) for treatment of CNV has greatly increased in recent years. Macugen®, a pegaptanib sodium injection, is a 28-base pair RNA aptamer that binds $VEGF_{165}$ (vascular endothelial growth factor), a particular pathogenic isoform of a family of growth factors, which induces choroidal neovascularisation – the clinical hallmark of wet, or exudative, AMD that ultimately leads to complete loss of vision [143, 144].

Ongoing research efforts into the molecular pathology of sight threatening diseases such as AMD and diabetic retinopathy have well established elevated $VEGF_{165}$ levels in patients affected with these diseases [20]. The oligonucleotide contains a 5'-polyethyle glycol group to increase the half-life of the aptamer in the vitreous, i.e. reducing the rate of vitreal clearance to the plasma, while also attenuating diffusion away from VEGF [145]. Aptamers carry both a high molecular weight due to large nucleic acid groups and negative charge and have historically required intravitreal administration to confer therapeutic effects against their pathological targets [26]. Additionally, nucleic acids have limited stability in biological media and are therefore both rapidly destabilized and cleared in the vitreous humour as the half-life of NX1838, an oligonucleotide-aptamer inhibitor of VEGF/vascular permeability factor, is approximately 94 hours following intravitreal injection [146]. This could lead to loss of therapeutic function as it is recognized that aptamers fold into highly specialized 3-D structures for specific binding to the active site, or functional domain, of their cognate protein - $VEGF_{165}$ in the case of AMD [26]. Pegaptanib confers its pharmacodynamics by binding the

VEGF receptors VEGF-A and VEGF-B with very high affinity (K_d = 50 pM) thereby inhibiting $VEGF_{165}$ from binding its cognate endothelial cell surface receptors [26, 145]. The aptamer is further modified with a 5'-polyethylene glycol (PEG) moiety and a 3'-dT (via a 3'-3' linkage) to both protect against exonuclease activity and prolong in-situ pharmacokinetic activity [145]. Phase I and II clinical trials of pegaptanib showed improved vision in a majority of patients after three months of intravitreal pegaptanib injections (Phase I: 12/15 patients; Phase II: 7/10), a follow-up randomized, controlled, multi-centre trial of 1,186 participants called VISION (VEGF Inhibition Study in Ocular Neovascularization) reported that the average patient still reported vision loss after intravitreal injections of pegaptanib [147-149].

Microneedles have less associated risks when compared with intravitreal injections that use macroscale stainless steel needles to delivery drug intraocularly as microneedles can penetrate the sclera as little as needed to effect a payload of drug within the tissues thus mitigate the chances of retinal detachment, cataract and endophthalmitis - risks associated with intravitreal injections [92, 150]. This concentration gradient can be maintained within the tissue for long periods of times. Microneedles also overcome the lack of localized delivery and low levels of bioavailability associated with topical eyedrops, periocular injections and systemic administration [27, 92, 151]. Microneedles also introduce much smaller sized defects into the eye when compared with the larger gauged hypodermic needles [92].

The methods developed in this thesis also offer an improvement over recent demonstrations of microneedle based ocular drug delivery where microneedles are made from conventional glass-drawn methods which have associated limitations. Jiang *et. al.* emphasized that though intrascleral delivery was shown with a pipette pulled needle, the method is a low throughput procedure stating that clinical applications would require multi-needle arrays and low-cost, high-throughput fabrication methods suitable for mass production [92, 97]. As microneedle-based devices would be single-use disposable instruments, any methods to minimize their manufacturing costs while maximizing product yields will be beneficial [114]. The microneedles fabricated using the improved method developed address each of these problems. The method also offers an improvement over existing non-integrated microneedle approaches where delivery cannot be easily targeted to specific tissues or released at specified rates.

The microneedles developed were able to fully penetrate and stay embedded within the ocular tissues due to frictional forces between the matrix and the glass surface. Demonstration of active control was achieved by developing leak-free, robust seals and interconnection methods to couple the devices to syringe pumps to deliver volumes at specified nanoscale rates.

Clearly, a device that can minimize the frequency of intravenous administrations, intravitreal injections and systemic dosing would be very useful for the mitigation of the associated risks involved in each of these delivery modes while concurrently reducing the frequency of inconvenient and painful procedures

for elderly patients. As such, as the current mode of delivery of these drugs is through bolus injection intravitreally, a longer term controlled dose administration approach has been the objective of many research groups in order to target delivery to the posterior segment in a frequent and ongoing regimen.

In addition to the primary goal of engineering a delivery device for the posterior eye, the secondary objective was to develop a better and highly repeatable method of hollow microneedle fabrication. This was achieved by adopting methods commonly used for optical microscopy probes. As fluid behavior on the microscale is dominated by viscous effects over inertial effects, exploiting surface tension effects at reduced dimensions - namely capillary forces defined as the rise or fall of a liquid in a narrow channel in accordance with the Young-Laplace relation - allows for a rapid and highly reproducible generation of microstructures. [152].

This was the first time a process used to make optical probes was modified and extended successfully for hollow microneedle fabrication for drug delivery applications. The protocols developed herein require minimal starting materials, facilities and equipment and yield target microneedle structures in a repeatable and reproducible manner. Single microneedles of any combination of inner and outer diameter could be fabricated within two hours. Furthermore, as silicon microneedle arrays can sometimes produce irregular needle shapes with high surface roughness values, the approach developed using surface tension forces yields highly reproducible, smooth surfaced (though not characterized) structures [61].

Facile fabrication of arrays of microneedles using smaller diameter capillary tubing was also demonstrated. Small diameter microneedles could also be batch fabricated to produce 15 microneedles/per hour in a repeatable manner. An original etching method using an electric field to manipulate microscale flows was also developed that allowed a single step “etch and deliver” solution further minimizing material consumption and associated costs.

A new method of microneedle device fabrication was developed in response to the high costs and complex instrumentation associated with conventional resource-intensive microfabrication methods. Conventional microfabrication methods employ expensive clean-room facilities and related equipment along with expertly trained personnel for operation. While this approach is useful and economical for high volume fabrication of integrated circuits and microdevices that require high-packing densities and precision, the same standard is not required for biomedical devices where high-packing densities of precision components, such as microneedles, is not necessarily required. Therefore, a solution was found which combines the precision associated with microfabrication with the low-costs of micromolding PDMS was designed and achieved.

The interfacial bond strength however will require some optimizations. Though the bond withstood an average force of 12 N before breaking (the forces to insert microneedles in skin are 10 N), insertion in to scleral tissue requires greater forces that have not been determined [87].

Further, all of the techniques developed can be performed in any standard wet lab to make a rigid microneedle with a flexible base capable of conforming to any underlying biological tissue.

This thesis presents an early embodiment of a hybrid approach to low-cost and accessible drug delivery using microneedles. The ultimate success of any pharmaceutical will depend ultimately on how good the delivery methods are to deploy them to diseased tissues. The methods developed so far not only have utility within the ocular tissues, but can be also used to target any tissue where controlled dosing and site-directed drug targeting is required. However, the feasibility of actual device insertion into a human or animal model will present challenges that merit further study. Future areas to explore that would extend the findings in this thesis include:

1. Characterization of pressure and flow rates required to deliver drugs for individual and multiple microneedles.

2. Demonstration of suprachoroidal delivery using better tissue sectioning methods to preserve the posterior spatial arrangement of tissues upon dissection.

3. Investigation into the effect of interneedle gap distances on microneedle geometry to produce tips of varying geometries that could be suited for a number of biological applications - from cell injection to drug delivery.

4. Identification of better adhesives to form stronger bonds between the PDMS and capillary tubings; set criteria for improved bonding to allow for device insertion/removal up to 50 times without failure through the modes identified.

5. Measurement of required insertion penetration forces.

6. Planarization of microneedle arrays to change the current configuration form in-plane to out-of-plane for more appropriate end use applications.

7. Integration with on-chip functionalities using pumps, reservoirs and valves in addition to integration with on-chip logic for wireless control.

8. Although, breakage of microneedles is a possibility due to the brittle nature of the glass microstructures, the fracture forces were not measured. A critical design constraint [114] for any microneedles is that the needle should not fracture during use. Forces required for fracture should be determined in conjunction with forces required to penetrate the scleral matrix.

9. Studies using animal models should be undertaken to assess risks during device insertion that could potentially require modification to the device specifications and design.

Chapter 12 References

1. Janoria, K.G., *et al*., *Novel approaches to retinal drug delivery.* Expert Opin Drug Deliv, 2007. **4**(4): p. 371-88.
2. Congdon, N., *et al*., *Causes and prevalence of visual impairment among adults in the United States.* Arch Ophthalmol, 2004. **122**(4): p. 477-85.
3. Friedman, D.S., *et al*., *Prevalence of age-related macular degeneration in the United States.* Arch Ophthalmol, 2004. **122**(4): p. 564-72.
4. Klein, R., *et al*., *The Wisconsin epidemiologic study of diabetic retinopathy. IV. Diabetic macular edema.* Ophthalmology, 1984. **91**(12): p. 1464-74.
5. Velez, G. and S.M. Whitcup, *New developments in sustained release drug delivery for the treatment of intraocular disease.* Br J Ophthalmol, 1999. **83**(11): p. 1225-9.
6. Langer, R., *Drug delivery and targeting.* Nature, 1998. **392**(6679 Suppl): p. 5-10.
7. Langer, R., *New methods of drug delivery.* Science, 1990. **249**(4976): p. 1527-33.
8. Zafar Razzacki, S., *et al*., *Integrated microsystems for controlled drug delivery.* Advanced Drug Delivery Reviews, 2004. **56**(2): p. 185-198.
9. Teo, A.L., *et al*., *Transdermal microneedles for drug delivery applications.* Materials Science and Engineering: B, 2006. **132**(1-2): p. 151-154.
10. Lang, J.C., *Ocular drug delivery conventional ocular formulations.* Advanced Drug Delivery Reviews, 1995. **16**(1): p. 39-43.
11. Hughes, P.M., *et al*., *Topical and systemic drug delivery to the posterior segments.* Advanced Drug Delivery Reviews, 2005. **57**(14): p. 2010-2032.
12. Fatt, I., and B. A. Weissman, *Physiology of the Eye, An Introduction to the Vegetative Functions*. 2nd ed. 1992, Boston: Butterworth-Heinemann.
13. Olsen, T.W., *et al*., *Human scleral permeability. Effects of age, cryotherapy, transscleral diode laser, and surgical thinning.* Invest Ophthalmol Vis Sci, 1995. **36**(9): p. 1893-903.
14. Ambati, J., *et al*., *Diffusion of high molecular weight compounds through sclera.* Invest Ophthalmol Vis Sci, 2000. **41**(5): p. 1181-5.
15. Ambati, J., *et al*., *Transscleral delivery of bioactive protein to the choroid and retina.* Invest Ophthalmol Vis Sci, 2000. **41**(5): p. 1186-91.
16. Foster, C.S., and M. Sainz de la Maza, *The Sclera*. 1994, New York: Springer-Verlag.
17. Geroski, D.H. and H.F. Edelhauser, *Transscleral drug delivery for posterior segment disease.* Adv Drug Deliv Rev, 2001. **52**(1): p. 37-48.
18. Geroski, D.H. and H.F. Edelhauser, *Drug delivery for posterior segment eye disease.* Invest Ophthalmol Vis Sci, 2000. **41**(5): p. 961-4.
19. Edwards, A.a.P., MR, *Fiber Matrix Model of Sclera and Corneal Stroma for Drug Delivery to the Eye.* Bioengineering, Food and Natural Products, 1998. **44**(1): p. 214-225.
20. Cheruvu, N.P. and U.B. Kompella, *Bovine and porcine transscleral solute transport: influence of lipophilicity and the Choroid-Bruch's layer.* Invest Ophthalmol Vis Sci, 2006. **47**(10): p. 4513-22.

21. Pitkanen, L., *et al*., *Permeability of retinal pigment epithelium: effects of permeant molecular weight and lipophilicity.* Invest Ophthalmol Vis Sci, 2005. **46**(2): p. 641-6.
22. Steuer, H., *et al*., *In vitro model of the outer blood-retina barrier.* Brain Res Brain Res Protoc, 2004. **13**(1): p. 26-36.
23. Hillenkamp, J., *et al*., *The influence of path length and matrix components on ageing characteristics of transport between the choroid and the outer retina.* Invest Ophthalmol Vis Sci, 2004. **45**(5): p. 1493-8.
24. Holekamp, N.M., *The vitreous gel: more than meets the eye.* Am J Ophthalmol. **149**(1): p. 32-6.
25. Tan, L.E., *et al*., *Effects of vitreous liquefaction on the intravitreal distribution of sodium fluorescein, fluorescein dextran, and fluorescent microparticles.* Invest Ophthalmol Vis Sci. **52**(2): p. 1111-8.
26. Fattal, E. and A. Bochot, *Ocular delivery of nucleic acids: antisense oligonucleotides, aptamers and siRNA.* Adv Drug Deliv Rev, 2006. **58**(11): p. 1203-23.
27. Urtti, E.M.d.A.a.A., *Current and future ophthalmic drug delivery systems: A shift to the posterior segment.* Drug Discovery Today, 2008. **13 Numbers 3/4**: p. 135 - 143.
28. Lee, S.S., *et al*., *Biodegradable implants for sustained drug release in the eye.* Pharm Res. **27**(10): p. 2043-53.
29. Bourges, J.L., *et al*., *Intraocular implants for extended drug delivery: therapeutic applications.* Adv Drug Deliv Rev, 2006. **58**(11): p. 1182-202.
30. Jaffe, G.J., *et al*., *Fluocinolone acetonide implant (Retisert) for noninfectious posterior uveitis: thirty-four-week results of a multicenter randomized clinical study.* Ophthalmology, 2006. **113**(6): p. 1020-7.
31. Yasukawa, T., *et al*., *Intraocular sustained drug delivery using implantable polymeric devices.* Adv Drug Deliv Rev, 2005. **57**(14): p. 2033-46.
32. Shive, M.S. and J.M. Anderson, *Biodegradation and biocompatibility of PLA and PLGA microspheres.* Adv Drug Deliv Rev, 1997. **28**(1): p. 5-24.
33. Ueda, H., *et al*., *Functional characterization of organic cation drug transport in the pigmented rabbit conjunctiva.* Invest Ophthalmol Vis Sci, 2000. **41**(3): p. 870-6.
34. Hughes, P.M., *et al*., *Topical and systemic drug delivery to the posterior segments.* Adv Drug Deliv Rev, 2005. **57**(14): p. 2010-32.
35. Imanidis, G., *et al*., *Estimation of skin target site acyclovir concentrations following controlled (trans)dermal drug delivery in topical and systemic treatment of cutaneous HSV-1 infections in hairless mice.* Pharm Res, 1994. **11**(7): p. 1035-41.
36. Ayalasomayajula, S.P. and U.B. Kompella, *Subconjunctivally administered celecoxib-PLGA microparticles sustain retinal drug levels and alleviate diabetes-induced oxidative stress in a rat model.* European Journal of Pharmacology, 2005. **511**(2-3): p. 191-198.

37. Barcia, E., *et al*., *Downregulation of endotoxin-induced uveitis by intravitreal injection of polylactic-glycolic acid (PLGA) microspheres loaded with dexamethasone.* Experimental Eye Research, 2009. **89**(2): p. 238-245.
38. Bourges, J.L., *et al*., *Ocular drug delivery targeting the retina and retinal pigment epithelium using polylactide nanoparticles.* Invest Ophthalmol Vis Sci, 2003. **44**(8): p. 3562-9.
39. Kompella, U.B., N. Bandi, and S.P. Ayalasomayajula, *Subconjunctival Nano- and Microparticles Sustain Retinal Delivery of Budesonide, a Corticosteroid Capable of Inhibiting VEGF Expression.* Investigative Ophthalmology & Visual Science, 2003. **44**(3): p. 1192-1201.
40. Hsu, J., *Drug delivery methods for posterior segment disease.* Curr Opin Ophthalmol, 2007. **18**(3): p. 235-9.
41. Carrasquillo, K.G., *et al*., *Controlled delivery of the anti-VEGF aptamer EYE001 with poly(lactic-co-glycolic)acid microspheres.* Invest Ophthalmol Vis Sci, 2003. **44**(1): p. 290-9.
42. Gomes dos Santos, A.L., *et al*., *Sustained release of nanosized complexes of polyethylenimine and anti-TGF-beta 2 oligonucleotide improves the outcome of glaucoma surgery.* J Control Release, 2006. **112**(3): p. 369-81.
43. Ebrahim, S., G.A. Peyman, and P.J. Lee, *Applications of liposomes in ophthalmology.* Surv Ophthalmol, 2005. **50**(2): p. 167-82.
44. Ruiz-Moreno, J.M., *et al*., *Photodynamic therapy and high-dose intravitreal triamcinolone to treat exudative age-related macular degeneration: 1-year outcome.* Retina, 2006. **26**(6): p. 602-12.
45. Carcaboso, A.M., *et al*., *Episcleral Implants for Topotecan Delivery to the Posterior Segment of the Eye.* Investigative Ophthalmology & Visual Science. **51**(4): p. 2126-2134.
46. Kato, A., *et al*., *Feasibility of Drug Delivery to the Posterior Pole of the Rabbit Eye with an Episcleral Implant.* Investigative Ophthalmology & Visual Science, 2004. **45**(1): p. 238-244.
47. J. Cruysberg, L.P., *et al*., *In Vitro Sustained Human Transscleral Drug Delivery of Fluorescein-Labeled Dexamethasone and Methotrexate with Fibrin Sealant.* Current Eye Research, 2005. **30**(8): p. 653-660.
48. Qian, Y., *et al*., *Preparation and evaluation of in situ gelling ophthalmic drug delivery system for methazolamide.* Drug Development and Industrial Pharmacy. **36**(11): p. 1340-1347.
49. Sia, S.K. and G.M. Whitesides, *Microfluidic devices fabricated in poly(dimethylsiloxane) for biological studies.* Electrophoresis, 2003. **24**(21): p. 3563-76.
50. Atencia, J. and D.J. Beebe, *Controlled microfluidic interfaces.* Nature, 2005. **437**(7059): p. 648-55.
51. Hsu, C.-H., C. Chen, and A. Folch, *"Microcanals" for micropipette access to single cells in microfluidic environments.* Lab on a Chip, 2004. **4**(5): p. 420-424.
52. Shawgo, R.S., *et al*., *BioMEMS for drug delivery.* Current Opinion in Solid State and Materials Science, 2002. **6**(4): p. 329-334.

53. Leoni, L. and T.A. Desai, *Nanoporous biocapsules for the encapsulation of insulinoma cells: biotransport and biocompatibility considerations.* Biomedical Engineering, IEEE Transactions on, 2001. **48**(11): p. 1335-1341.
54. Leoni, L., A. Boiarski, and T.A. Desai, *Characterization of Nanoporous Membranes for Immunoisolation: Diffusion Properties and Tissue Effects.* Biomedical Microdevices, 2002. **4**(2): p. 131-139.
55. Cao, L., S. Mantell, and D. Polla, *Design and simulation of an implantable medical drug delivery system using microelectromechanical systems technology*. Sensors and Actuators A: Physical, 2001. **94**(1-2): p. 117-125.
56. Maillefer, D., *et al*. *A high-performance silicon micropump for disposable drug delivery systems*. in *Micro Electro Mechanical Systems, 2001. MEMS 2001. The 14th IEEE International Conference on*. 2001.
57. Ahmed, A., C. Bonner, and T.A. Desai, *Bioadhesive Microdevices for Drug Delivery: A Feasibility Study.* Biomedical Microdevices, 2001. **3**(2): p. 89-96.
58. Santini, J.T., M.J. Cima, and R. Langer, *A controlled-release microchip.* Nature, 1999. **397**(6717): p. 335-338.
59. Tao, S.L. and T.A. Desai, *Microfabricated drug delivery systems: from particles to pores.* Adv Drug Deliv Rev, 2003. **55**(3): p. 315-28.
60. Ryan F. Donnelly, t.R.R.S.a.A.D.W., *Microneedle-based drug delivery systems: Microfabrication, drug delivery, and safety.* Drug Delivery, 2010. **17**(4): p. 187-207.
61. Henry, S., *et al*., *Microfabricated microneedles: a novel approach to transdermal drug delivery.* J Pharm Sci, 1998. **87**(8): p. 922-5.
62. Shifeng, L. and C. Shaochen, *Polydimethylsioxane fluidic interconnects for microfluidic systems.* Advanced Packaging, IEEE Transactions on, 2003. **26**(3): p. 242-247.
63. Teo, M.A., *et al*., *In vitro and in vivo characterization of MEMS microneedles.* Biomed Microdevices, 2005. **7**(1): p. 47-52.
64. Santini, J.T., Jr., M.J. Cima, and R. Langer, *A controlled-release microchip.* Nature, 1999. **397**(6717): p. 335-8.
65. McAllister, D.V., *et al*., *Microfabricated needles for transdermal delivery of macromolecules and nanoparticles: fabrication methods and transport studies.* Proc Natl Acad Sci U S A, 2003. **100**(24): p. 13755-60.
66. Smart, W.H. and K. Subramanian, *The use of silicon microfabrication technology in painless blood glucose monitoring.* Diabetes Technol Ther, 2000. **2**(4): p. 549-59.
67. Champion, R.H., Burton, J.L., Ebling, F.J.G., *Textbook of Dermatology*. 1992: Blackwell Scientific: London.
68. Gross, J.a.K., J.G. , *Intradermal drug delivery device and method for intradermal delivery of drugs*. 1996.
69. Jang, K.K., *Skin perforating device for transdermal medication*. 1997.
70. Place, M.S.G.a.V.A., *Drug Delivery Device*, U.S. Patent, Editor. June 22, 1976, Alza Corporation: U.S.

71. Prausnitz, M.R., *Microneedles for transdermal drug delivery.* Adv Drug Deliv Rev, 2004. **56**(5): p. 581-7.
72. Jingkuang, C., *et al*., *A multichannel neural probe for selective chemical delivery at the cellular level.* Biomedical Engineering, IEEE Transactions on, 1997. **44**(8): p. 760-769.
73. Liwei, L. and A.P. Pisano, *Silicon-processed microneedles.* Microelectromechanical Systems, Journal of, 1999. **8**(1): p. 78-84.
74. Gardeniers, H.J.G.E., *et al*., *Silicon micromachined hollow microneedles for transdermal liquid transport.* Microelectromechanical Systems, Journal of, 2003. **12**(6): p. 855-862.
75. Talbot NH, P.A. *Polymolding: two wafer polysiliconmicromolding of closed-flow passages for microneedles and microfluidic devices*. in *Tech. Dig. IEEE Solid-State Sens. Actuator Workshop*. 1998. Hilton Head Island.
76. McAllister, D.V., Kaushik S, Patel PN, Mayberry JL, Allen MG and Prausnitz MR. *Solid and hollow microneedles for transdermal drug delivery*. in *Proc. Int. Symp. Control. Release Bioact. Mater., 26th, Boston*. 1999.
77. Jing J, T.F., Miao J, *Microfabricated Hollow MIcroneedle Array Using ICP Etcher.* Journal of Physics: Conference Series, 2006. **34**: p. 1132-1136.
78. Roxhed, N., *et al*., *Penetration-Enhanced Ultrasharp Microneedles and Prediction on Skin Interaction for Efficient Transdermal Drug Delivery.* Microelectromechanical Systems, Journal of, 2007. **16**(6): p. 1429-1440.
79. Paik, S.-J., *et al*., *In-plane single-crystal-silicon microneedles for minimally invasive microfluid systems.* Sensors and Actuators A: Physical, 2004. **114**(2-3): p. 276-284.
80. Brazzle JD, P.I., Frazier AB. *Fluid-coupled hollow metallic micromachined needle arrays*. in *Proc. SPIE Conf. Microfluidic Dev. Syst.* 1998. Santa Clara, CA.
81. Chandrasekaran, S., J.D. Brazzle, and A.B. Frazier, *Surface micromachined metallic microneedles.* Journal of Microelectromechanical Systems, 2003. **12**(3): p. 281-288.
82. Kim K, P.D., Lu HM, Che W, Kim K, Lee J and Ahn C, *A tapered hollow metallicmicroneedle array using backside exposure of SU-8.* Journal of Micromechanics and Microengineering, 2004. **14**: p. 597-603.
83. J, K.K.a.L., *High aspect ratio tapered hollow metallic microneedle arrays with microfluidic interconnector.* Microsyst Technol, 2007. **13**: p. 231-235.
84. Davis, S.P., *et al*., *Hollow metal microneedles for insulin delivery to diabetic rats.* IEEE transactions on bio-medical engineering, 2005. **52**(5): p. 909-15.
85. Verbaan, F.J., *et al*., *Assembled microneedle arrays enhance the transport of compounds varying over a large range of molecular weight across human dermatomed skin.* Journal of Controlled Release, 2007. **117**(2): p. 238-245.
86. Gill, H.S. and M.R. Prausnitz, *Coated microneedles for transdermal delivery.* Journal of Controlled Release, 2007. **117**(2): p. 227-237.
87. Jiang, J., *et al*., *Coated microneedles for drug delivery to the eye.* Invest Ophthalmol Vis Sci, 2007. **48**(9): p. 4038-43.

88. Jung-Hwan, P., M.G. Allen, and M.R. Prausnitz. *Biodegradable polymer microneedles: fabrication, mechanics and transdermal drug delivery*. in *Engineering in Medicine and Biology Society, 2004. IEMBS '04. 26th Annual International Conference of the IEEE*. 2004.
89. Sullivan, S.P., N. Murthy, and M.R. Prausnitz, *Minimally Invasive Protein Delivery with Rapidly Dissolving Polymer Microneedles.* Advanced Materials, 2008. **20**(5): p. 933-938.
90. Hanada, T.M.Y.T.T.K.Y.M.H.T.M.W.K., *Sugar Micro Needles as Transdermic Drug Delivery System.* Biomed Microdevices, 2005. **7**: p. 185-188.
91. Po-Chun, W., *et al*. *Hypodermic-needle-like hollow polymer microneedle array using UV lithography into micromolds*. in *Micro Electro Mechanical Systems (MEMS), 2011 IEEE 24th International Conference on*. 2011.
92. Jiang, J., *et al*., *Intrascleral drug delivery to the eye using hollow microneedles.* Pharm Res, 2009. **26**(2): p. 395-403.
93. Patel, S.R., *et al*., *Suprachoroidal Drug Delivery to the Back of the Eye Using Hollow Microneedles.* Pharm Res.
94. Lee, S., W. Jeong, and D.J. Beebe, *Microfluidic valve with cored glass microneedle for microinjection.* Lab on a Chip, 2003. **3**(3): p. 164-167.
95. Wang, P.M., *et al*., *Precise Microinjection into Skin Using Hollow Microneedles.* J Invest Dermatol, 2006. **126**(5): p. 1080-1087.
96. Martanto, W., *et al*., *Mechanism of fluid infusion during microneedle insertion and retraction.* J Control Release, 2006. **112**(3): p. 357-61.
97. Martanto, W., *et al*., *Microinfusion Using Hollow Microneedles.* Pharm Res, 2006. **23**(1): p. 104-113.
98. Patel, S., *et al*., *Suprachoroidal Drug Delivery to the Back of the Eye Using Hollow Microneedles.* Pharm Res, 2011. **28**(1): p. 166-176.
99. Kelly, R.T., *et al*., *Chemically etched open tubular and monolithic emitters for nanoelectrospray ionization mass spectrometry.* Analytical Chemistry, 2006. **78**(22): p. 7796-7801.
100. Wahl, J.H., *et al*., *Attomole level capillary electrophoresis-mass spectrometric protein analysis using 5 .mu.m i.d. capillaries.* Analytical Chemistry, 1992. **64**(24): p. 3194-3196.
101. Emmett, M.R. and R.M. Caprioli, *Micro-electrospray mass spectrometry: ultra-high-sensitivity analysis of peptides and proteins.* Journal of the American Society for Mass Spectrometry, 1994. **5**(7): p. 605-613.
102. Reaume, S.E., *The use of hydrofluoric acid in making glass microneedles.* Science, 1952. **116**(3023): p. 641.
103. Stockle, R., *et al*., *High-quality near-field optical probes by tube etching.* Applied Physics Letters, 1999. **75**(2): p. 160-162.
104. Reddick, R.C., R.J. Warmack, and T.L. Ferrell, *New Form of Scanning Optical Microscopy.* Physical Review B, 1989. **39**(1): p. 767-770.
105. Puygranier, B.A.F. and P. Dawson, *Chemical etching of optical fibre tips - experiment and model.* Ultramicroscopy, 2000. **85**(4): p. 235-248.

106. Pak Kin Wong, T.-H.W., and Chih-Ming Ho, *Optical fiber tip fabricated by surface tension controlled etching.* Solid-State Sensor, Actuator and Microsystems Workshop, Hilton Head Island, South Carolina, June 2-6, 2002.
107. Wong, P.K., U. Ulmanella, and C.M. Ho, *Fabrication process of microsurgical tools for single-cell trapping and intracytoplasmic injection.* Journal of Microelectromechanical Systems, 2004. **13**(6): p. 940-946.
108. Xiao, M.F., *et al*., *Fabrication of probe tips for reflection scanning near-field optical microscopes: Chemical etching and heating-pulling methods.* Journal of Vacuum Science & Technology B, 1997. **15**(4): p. 1516-1520.
109. Cefali E, P.S., Spadaro S, Gardelli R, Albani M and Allegrini M *Applied Scanning Probe Methods VIII Scanning Probe Microscopy Techniques Nano Science and Technology* 2008: Springer Berlin Heidelberg.
110. Sayah, A., *et al*., *Fiber tips for scanning near-field optical microscopy fabricated by normal and reverse etching.* Ultramicroscopy, 1998. **71**(1-4): p. 59-63.
111. Hosain, S.I., Y. Lacroute, and J.P. Goudonnet, *A simple low-cost highly reproducible method of fabricating optical fiber tips for a photon scanning tunneling microscope.* Microwave and Optical Technology Letters, 1996. **13**(5): p. 243-248.
112. Hoffmann, P., B. Dutoit, and R.P. Salathe, *Comparison of mechanically drawn and protection layer chemically etched optical fiber tips.* Ultramicroscopy, 1995. **61**(1-4): p. 165-170.
113. Takahashi, K.M., J. Colloids Interf Sci. , 1969. **38**: p. 323-337.
114. Stoeber, B. and D. Liepmann. *Fluid injection through out-of-plane microneedles.* in *Microtechnologies in Medicine and Biology, 1st Annual International, Conference On. 2000*. 2000.
115. Sze, A., *et al*., *Zeta-potential measurement using the Smoluchowski equation and the slope of the current-time relationship in electroosmotic flow.* Journal of Colloid and Interface Science, 2003. **261**(2): p. 402-410.
116. Schwer, C. and E. Kenndler, *Electrophoresis in fused-silica capillaries: the influence of organic solvents on the electroosmotic velocity and the .zeta. potential.* Analytical Chemistry, 1991. **63**(17): p. 1801-1807.
117. Rodriguez, I., *et al*., *Rapid prototyping of glass microchannels.* Analytica Chimica Acta, 2003. **496**(1-2): p. 205-215.
118. Whitesides, G.M. and A.D. Stroock, *Flexible methods for microfluidics.* Physics Today, 2001. **54**(6): p. 42-48.
119. Weibel, D.B., W.R. DiLuzio, and G.M. Whitesides, *Microfabrication meets microbiology.* Nat Rev Micro, 2007. **5**(3): p. 209-218.
120. Chaudhury, M.K.a.W., G.M., *Direct measurement of interfacial interactions between*
semispherical lenses and flat sheets of poly(dimethylsiloxane) and their chemical derivatives Langmuir, 1991. **7**: p. 1013–1025.
121. M. Morra, E.O., R. Marola, F. Garbassi, P. Humphrey, D. Johnson, *On the aging of oxygen plasma-treated polydimethylsiloxane surfaces.* Journal of Colloid and Interface Science, June 1990. **137**(1): p. 11-24.

122. Whitesides, J.M.K.N.I.G.A.D.S.G.M., *Components for integrated poly(dimethylsiloxane) microfluidic systems.* Electrophoresis, 2002. **23**: p. 3461–3473.
123. Chuang, Y.H., *et al*., *A simple chemical etching technique for reproducible fabrication of robust scanning near-field fiber probes.* Review of Scientific Instruments, 1998. **69**(2): p. 437-439.
124. Huo, X., S. Pan, and S.F. Wu, *Fabrication of pure silica core multimode ultraviolet optical fibre probes by tube etching.* Chinese Physics Letters, 2007. **24**(10): p. 2876-2878.
125. Iles, A., *Chips & Tips: Overcoming interfacing issues by adding fumed silica.* Lab-on-a-Chip: Chips and Tips, November 21 2008.
126. Gavet, O. and J. Pines, *Progressive Activation of CyclinB1-Cdk1 Coordinates Entry to Mitosis.* Developmental cell, 2010. **18**(4): p. 533-543.
127. Abramoff, M.D., Magelhaes, P.J., Ram, S.J., *Image Processing with ImageJ.* Biophotonics International, 2004. **11**(7): p. 36-42.
128. Cruysberg, L.P., *et al*., *The influence of intraocular pressure on the transscleral diffusion of high-molecular-weight compounds.* Invest Ophthalmol Vis Sci, 2005. **46**(10): p. 3790-4.
129. Suh, Y.D. and R. Zenobi, *Improved probes for scanning near-field optical microscopy.* Advanced Materials, 2000. **12**(15): p. 1139-+.
130. Lazarev, A., *et al*., *Formation of fine near-field scanning optical microscopy tips. Part I. By static and dynamic chemical etching.* Review of Scientific Instruments, 2003. **74**(8): p. 3679-3683.
131. Wong, P.K., Wang T and Ho C. *Optical Fiber Tip Fabricated By Surface Tension Controlled Etching*. in *Solid-State sensor, Actuator and Microsystems Workshop*. 2002. Hilton Head Island, South Carolina.
132. Lambelet, P., *et al*., *Chemically etched fiber tips for near-field optical microscopy: a process for smoother tips.* Applied Optics, 1998. **37**(31): p. 7289-7292.
133. Wang, W., *et al*., *Lipophilicity influence on conjunctival drug penetration in the pigmented rabbit: a comparison with corneal penetration.* Current eye research, 1991. **10**(6): p. 571-9.
134. Olsen, T.W., *et al*., *Porcine Sclera: Thickness and Surface Area.* Investigative Ophthalmology & Visual Science, 2002. **43**(8): p. 2529-2532.
135. Karas, M., U. Bahr, and T. Dülcks, *Nano-electrospray ionization mass spectrometry: addressing analytical problems beyond routine.* Fresenius' Journal of Analytical Chemistry, 2000. **366**(6): p. 669-676.
136. Cech, N.B. and C.G. Enke, *Practical implications of some recent studies in electrospray ionization fundamentals.* Mass Spectrometry Reviews, 2001. **20**(6): p. 362-387.
137. Koerner, T., *et al*., *Porous Polymer Monolith Assisted Electrospray.* Analytical Chemistry, 2004. **76**(21): p. 6456-6460.
138. H.A. Stone, A.D.S., A. Ajdari, *Engineering Flows in Small Devices: Microfluidics Towards Lab-on-a-Chip.* Annu. Rev. Fluid Mech., 2004. **36**: p. 381-411.

139. Horibe, Y., *et al*., *Polar solute transport across the pigmented rabbit conjunctiva: size dependence and the influence of 8-bromo cyclic adenosine monophosphate.* Pharmaceutical research, 1997. **14**(9): p. 1246-51.
140. Pitkanen, L., *et al*., *Permeability of retinal pigment epithelium: effects of permeant molecular weight and lipophilicity.* Investigative Ophthalmology & Visual Science, 2005. **46**(2): p. 641-6.
141. Ahmed, I., *et al*., *Physicochemical determinants of drug diffusion across the conjunctiva, sclera, and cornea.* Journal of pharmaceutical sciences, 1987. **76**(8): p. 583-6.
142. Ranta, V.-P. and A. Urtti, *Transscleral drug delivery to the posterior eye: Prospects of pharmacokinetic modeling.* Advanced Drug Delivery Reviews, 2006. **58**(11): p. 1164-1181.
143. Ferrara, N., *Vascular endothelial growth factor: basic science and clinical progress.* Endocr Rev, 2004. **25**(4): p. 581-611.
144. Kvanta, A., *et al*., *Subfoveal fibrovascular membranes in age-related macular degeneration express vascular endothelial growth factor.* Invest Ophthalmol Vis Sci, 1996. **37**(9): p. 1929-34.
145. Ruckman, J., *et al*., *2'-Fluoropyrimidine RNA-based aptamers to the 165-amino acid form of vascular endothelial growth factor (VEGF165). Inhibition of receptor binding and VEGF-induced vascular permeability through interactions requiring the exon 7-encoded domain.* J Biol Chem, 1998. **273**(32): p. 20556-67.
146. Drolet, D.W., *et al*., *Pharmacokinetics and safety of an anti-vascular endothelial growth factor aptamer (NX1838) following injection into the vitreous humor of rhesus monkeys.* Pharm Res, 2000. **17**(12): p. 1503-10.
147. *Preclinical and phase 1A clinical evaluation of an anti-VEGF pegylated aptamer (EYE001) for the treatment of exudative age-related macular degeneration.* Retina, 2002. **22**(2): p. 143-52.
148. Group, T.E.S., *Anti-vascular endothelial growth factor therapy for subfoveal choroidal neovascularization secondary to age-related macular degeneration.* Ophthalmology, 2003. **110**: p. 979–986.
149. Gragoudas, E.S., *et al*., *Pegaptanib for neovascular age-related macular degeneration.* N Engl J Med, 2004. **351**(27): p. 2805-16.
150. Jager RD, A.L., Patel SC, *Risks of Intravitreal Injection: a comprehensive review.* Retina, 2004. **24**: p. 676-698.
151. Ghate, D. and H.F. Edelhauser, *Ocular drug delivery.* Expert Opin Drug Deliv, 2006. **3**(2): p. 275-87.
152. Adamson, A.W.G., A.P. , *Physical Chemistry of Surfaces*. 1997, New York: Wiley & Sons.

Chapter 13 Appendix

13.1. Polymicro Fused Silica Product Guide

Flexible Fused Silica Capillary Tubing

Capillary

- TSP: Standard Polyimide Coating
- TSG: High Temperature Polyimide Coating

TSP & TSG Standard Products

Product Descriptor	ID µm	OD µm	CT* µm
TSP002150	002 ± 01	150 ± 06	12
TSP005150	005 ± 02	150 ± 06	12
TSP005375	005 ± 02	363 ± 10	20
TSP010150	010 ± 02	150 ± 06	12
TSP010375	010 ± 02	363 ± 10	20
TSP015150	015 ± 02	150 ± 06	12
TSP015375	015 ± 02	363 ± 10	20
TSP020090	020 ± 02	090 ± 06	12
TSP020150	020 ± 02	150 ± 06	12
TSP020375	020 ± 02	363 ± 10	20
TSP025150	025 ± 02	150 ± 06	12
TSP025375	025 ± 02	363 ± 10	20
TSP030150	030 ± 02	150 ± 06	12
TSP030375	030 ± 02	363 ± 10	20
TSP040105	040 ± 03	105 ± 06	12
TSP040150	040 ± 03	150 ± 06	12
TSP040375	040 ± 03	363 ± 10	20
TSP050150	050 ± 03	150 ± 06	12
TSP050192	050 ± 03	186 ± 06	16
TSP050375	050 ± 03	363 ± 10	20
TSP075150	075 ± 03	150 ± 06	12
TSP075200	075 ± 03	193 ± 07	12
TSP075375	075 ± 03	363 ± 10	20
TSP100170	100 ± 04	164 ± 06	12
TSP100200	100 ± 04	193 ± 07	12
TSP100245	100 ± 04	238 ± 07	16
TSP100375	100 ± 04	363 ± 10	20
TSP150375	150 ± 04	363 ± 10	20
TSP180350	180 ± 06	360 ± 10	18
TSP200350	200 ± 06	360 ± 10	18
TSP250350	250 ± 06	360 ± 10	18
TSP320450	320 ± 06	435 ± 10	18
TSP450670	450 ± 06	673 ± 15	24
TSP530660	536 ± 06	665 ± 15	24
TSP530700	530 ± 10	700 ± 20	24
TSP700850	700 ± 10	850 ± 20	24
TSG250350	250 ± 06	350 ± 15	20
TSG320450	320 ± 06	435 ± 15	18
TSG530660	536 ± 06	680 ± 25	30

* CT is Coating Thickness per side; value is nominal.

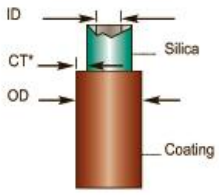

TSP Characteristics

- Standard polyimide coating
- Synthetic fused silica
- 100% proof tested for strength
- Operation up to 350°C

TSG Characteristics

- High temperature polyimide coating
- Synthetic fused silica
- 100% proof tested for strength
- Operation up to 400°C

Explore Our Other Unique Capillary Products and Capabilities

- Custom ID & OD sizes and tolerances
- Internal and external coatings
- Shaped cross-sectional geometries
- Precision cleaving
- Laser cutting
- Windowing
- Custom arrays and assemblies

Online Ordering

Products with ID of 320µm and smaller are available for immediate online ordering in quantities of 10m, 25m, or 50m. Go to www.polymicro.com to buy your capillary tubing today.

- Flexible Capillary
- Multimode Optical Fiber
- Specialty Assemblies
- Micro-Components

Polymicro TECHNOLOGIES
A Subsidiary of molex

18019 N. 25th Avenue
Phoenix, AZ 85023-1200
Ph: (602) 375.4100
Fax: (602) 375.4110
polymicrosales@molex.com
www.polymicro.com

PT-TSP/TSG: 01-08

13.2. PX273- Pressure Transducer

To measure process variables associated with etching microneedles, a PX273-300DI Pressure Transmitter (OMEGA Engineering, Stamford, CT) and separate 24 VDC converter were purchased.

The manufacturer-supplied transducer gave current as the output. In order to simplify data acquisition, the circuit was modified by placing a 499 Ω resistor to obtain voltage output.

To accomplish this, three 5/16" holes were drilled using a conical step drill bit at the 5/16" mark on the backside for both the electrical output and 24 VDC power supply as these ports were not provided in the manufacturer supplied housing as shown in Figure 91. The output was changed from 4-20 mA current to voltage (1.99 – 9.99 VDC) using a 499 Ω resistor. This conversion of the signal allowed for more convenient measurement using a standard multimeter. The output terminals/power supply was then soldered to the circuit board.

The sensor was calibrated using a pressure calibrator with a known pressure source as shown in Figure 92.

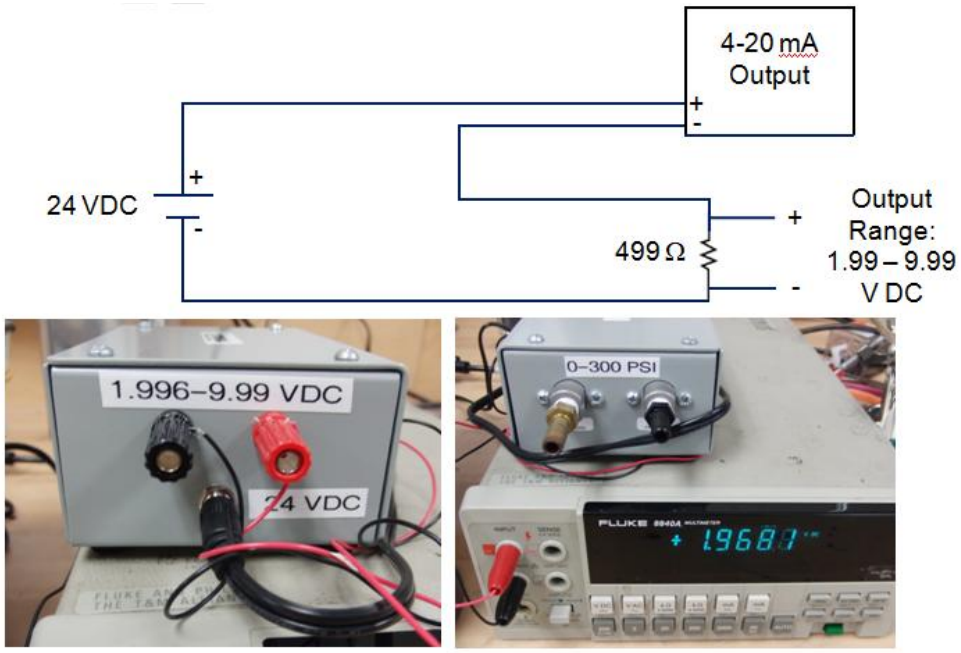

Figure 91. Pressure transducer DC output and fitted with a 24 VDC power supply

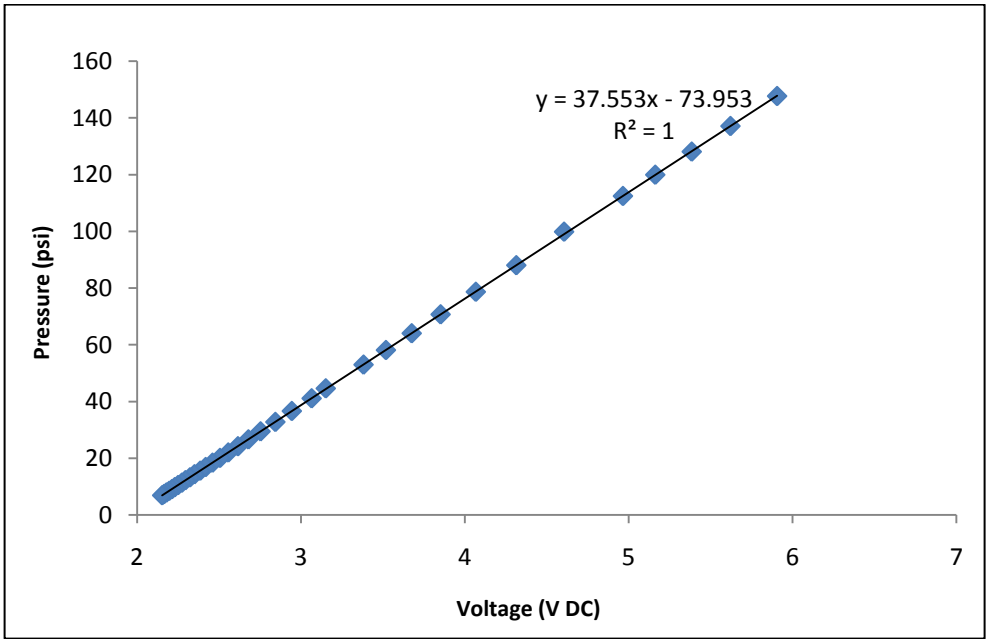

Figure 92. Pressure sensor calibration curve for the PX273 – 300 DI.

13.3. Standard Curves for Quantification of Model Compounds

6-aminoquinolone Standard Curve – Linear Region

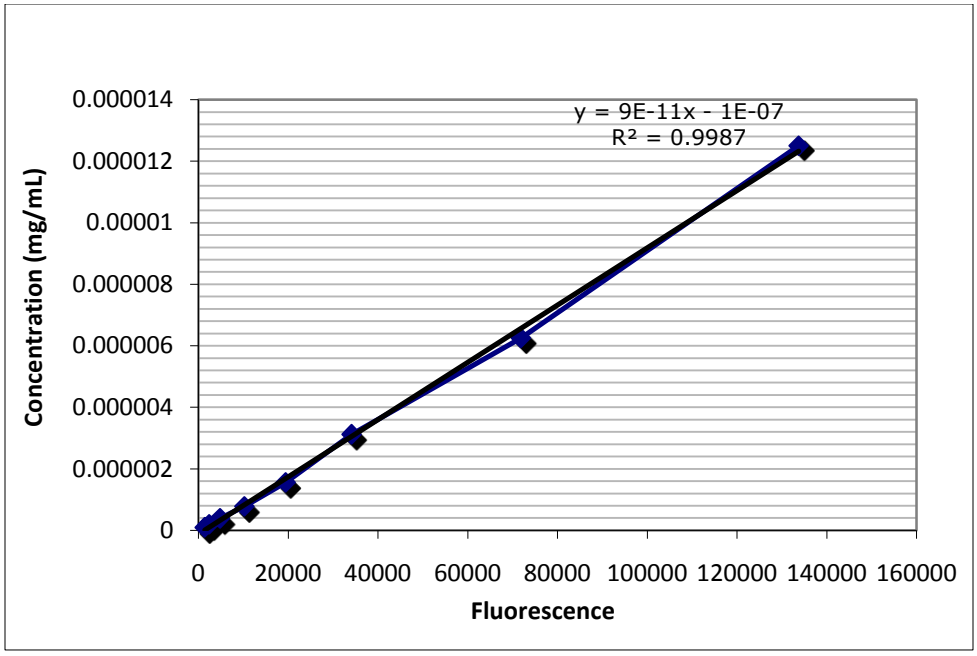

Rose Bengal Standard Curve – Linear Region

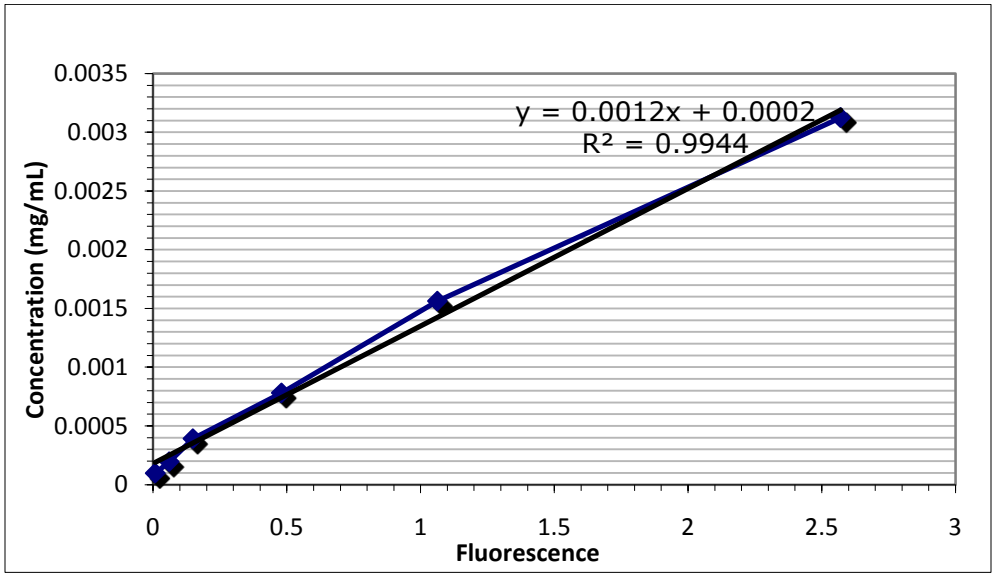

40 KDa-FITC Dextran Standard Curve - Linear Range